

Functional Nanomaterials for Energy Conversion and Storage

Guest Editors: Tianyi Kou, Gongming Wang, Xihong Lu, Yang Song,
and Teng Zhai





Functional Nanomaterials for Energy Conversion and Storage

Journal of Nanomaterials

Functional Nanomaterials for Energy Conversion and Storage

Guest Editors: Tianyi Kou, Gongming Wang, Xihong Lu,
Yang Song, and Teng Zhai



Copyright © 2016 Hindawi Publishing Corporation. All rights reserved.

This is a special issue published in "Journal of Nanomaterials." All articles are open access articles distributed under the Creative Commons Attribution License, which permits unrestricted use, distribution, and reproduction in any medium, provided the original work is properly cited.

Editorial Board

- Domenico Acierno, Italy
Katerina Aifantis, USA
Nageh K. Allam, USA
Margarida Amaral, Portugal
Martin Andersson, Sweden
Raul Arenal, Spain
Ilaria Armentano, Italy
Vincenzo Baglio, Italy
Lavinia Balan, France
Thierry Baron, France
Andrew R. Barron, USA
Hongbin Bei, USA
Daniel Bellet, France
Stefano Bellucci, Italy
Enrico Bergamaschi, Italy
Samuel Bernard, France
Debes Bhattacharyya, New Zealand
Sergio Bietti, Italy
Giovanni Bongiovanni, Italy
Theodorian Borca-Tasciuc, USA
Mohamed Bououdina, Bahrain
Torsten Brezesinski, Germany
C. Jeffrey Brinker, USA
Christian Brosseau, France
Philippe Caroff, Australia
Victor M. Castaño, Mexico
Albano Cavaleiro, Portugal
Bhanu P. S. Chauhan, USA
Shafiu Chowdhury, USA
Jin-Ho Choy, Republic of Korea
Kwang-Leong Choy, UK
Yu-Lun Chueh, Taiwan
Elisabetta Comini, Italy
Giuseppe Compagnini, Italy
David Cornu, France
M. A. Correa-Duarte, Spain
P. Davide Cozzoli, Italy
Shadi A. Dayeh, USA
Luca Deseri, USA
Yong Ding, USA
Philippe Dubois, Belgium
Zehra Durmus, Turkey
Joydeep Dutta, Oman
Ali Eftekhari, USA
Samy El-Shall, USA
- Ovidiu Ersen, France
Claude Estournès, France
Andrea Falqui, KSA
Matteo Ferroni, Italy
Ilaria Fratoddi, Italy
Alan Fuchs, USA
Miguel A. Garcia, Spain
Siddhartha Ghosh, Singapore
P. K. Giri, India
Russell E. Gorga, USA
Jihua Gou, USA
Jean M. Greneche, France
Smrati Gupta, Germany
Kimberly Hamad-Schifferli, USA
Simo-Pekka Hannula, Finland
Michael Harris, USA
Yasuhiko Hayashi, Japan
F. Hernandez-Ramirez, Spain
Michael Z. Hu, USA
Nay Ming Huang, Malaysia
Shaoming Huang, China
Zafar Iqbal, USA
B. Jeyadevan, Japan
Xin Jiang, Germany
Rakesh Joshi, Australia
Jeong-won Kang, Republic of Korea
Hassan Karimi-Maleh, Iran
Antonios Kelarakis, UK
Alireza Khataee, Iran
Ali Khorsand Zak, Iran
Philippe Knauth, France
Ralph Krupke, Germany
C. Kübel, Germany
Prashant Kumar, UK
Eric Le Bourhis, France
Jun Li, Singapore
Meiyong Liao, Japan
Shijun Liao, China
Silvia Licoccia, Italy
Wei Lin, USA
Nathan C. Lindquist, USA
Zainovia Lockman, Malaysia
Nico Lovergine, Italy
Jim Low, Australia
Jue Lu, USA
- Ed Ma, USA
Laura M. Maestro, Spain
Gaurav Mago, USA
Muhamamd A. Malik, UK
D. Mangalaraj, India
Sanjay R. Mathur, Germany
Tony McNally, UK
Yogendra Mishra, Germany
P. Cesar Morais, Brazil
Paul Munroe, Australia
Jae-Min Myoung, Republic of Korea
Rajesh R. Naik, USA
Albert Nasibulin, Russia
Toshiaki Natsuki, Japan
Koichi Niihara, Japan
Natalia Noginova, USA
Sherine Obare, USA
Won-Chun Oh, Republic of Korea
Atsuto Okamoto, Japan
Abdelwahab Omri, Canada
Ungyu Paik, Republic of Korea
P. Pallavicini, Italy
Edward A. Payzant, USA
A. Pegoretti, Italy
Ton Peijs, UK
O. Perales-Pérez, Puerto Rico
J. Pérez-Juste, Spain
Alexey P. Popov, Finland
Philip D. Rack, USA
Peter Reiss, France
Orlando Rojas, USA
Marco Rossi, Italy
Ilker S. Bayer, Italy
Cengiz S. Ozkan, USA
Sudipta Seal, USA
Shu Seki, Japan
V. Šepelák, Germany
Huaiyu Shao, Japan
Prashant Sharma, USA
Donglu Shi, USA
Bhanu P. Singh, India
Surinder Singh, USA
Vladimir Sivakov, Germany
Adolfo Speghini, Italy
Marinella Striccoli, Italy



Xuping Sun, KSA
A. K. Sundramoorthy, USA
Angelo Taglietti, Italy
Bo Tan, Canada
Leander Tapfer, Italy
Valeri P. Tolstoy, Russia
Muhammet S. Toprak, Sweden
R. Torrecillas, Spain
Achim Trampert, Germany
Takuya Tsuzuki, Australia

Tamer Uyar, Turkey
Bala Vaidhyanathan, UK
Luca Valentini, Italy
Rajender S. Varma, USA
Ester Vazquez, Spain
Ajayan Vinu, Australia
Ruibing Wang, Macau
Shiren Wang, USA
Yong Wang, USA
Magnus Willander, Sweden

Ping Xiao, UK
Zhi Li Xiao, USA
Yangchuan Xing, USA
Doron Yadlovker, Israel
Yoke K. Yap, USA
Kui Yu, Canada
William Yu, USA
Michele Zappalorto, Italy
Renyun Zhang, Sweden

Contents

Functional Nanomaterials for Energy Conversion and Storage

Tianyi Kou, Gongming Wang, Xihong Lu, Yang Song, and Teng Zhai
Volume 2016, Article ID 8521320, 1 page

Continued Multicolumns Bioleaching for Low Grade Uranium Ore at a Certain Uranium Deposit

Gongxin Chen, Zhanxue Sun, and Yajie Liu
Volume 2016, Article ID 1683416, 7 pages

The Comparative Study of Electrochemical Capacitance Performance between Sulphur-Doped Co_3O_4 and CoS Anodes

Wei Xu, M. A. Khan, Jiahui Chen, Yongbing Long, Gui Xu, Yu Bai, Xiaodong Zhang, Zhenmin Qiu, Sennian Lin, and Donghua Fan
Volume 2016, Article ID 5676380, 5 pages

Twist-Shaped CuO Nanowires as Anode Materials for Lithium Ion Batteries

Hongdong Liu, Ye Lin, Zhongli Hu, Rong Hu, Haibo Ruan, and Lei Zhang
Volume 2016, Article ID 2864962, 5 pages

Manganese Oxide on Carbon Fabric for Flexible Supercapacitors

Jianfeng Zhang, Mujun Chen, Yunwang Ge, and Qi Liu
Volume 2016, Article ID 2870761, 7 pages

ZnO Nanocrystals as Anode Electrodes for Lithium-Ion Batteries

Wenhui Zhang, Lijuan Du, Zongren Chen, Juan Hong, and Lu Yue
Volume 2016, Article ID 8056302, 7 pages

Effect of Na Doping on the Nanostructures and Electrical Properties of ZnO Nanorod Arrays

Lu Yue, Zhiqiang Zhang, Yanyan Ma, and Wenhui Zhang
Volume 2016, Article ID 3040536, 5 pages

Multishelled NiO Hollow Spheres Decorated by Graphene Nanosheets as Anodes for Lithium-Ion Batteries with Improved Reversible Capacity and Cycling Stability

Lihua Chu, Meicheng Li, Yu Wang, Xiaodan Li, Zipei Wan, Shangyi Dou, and Yue Chu
Volume 2016, Article ID 4901847, 6 pages

Lanthanide Coordination Polymer Nanosheet Aggregates: Solvothermal Synthesis and Downconversion Luminescence

Rui-Rui Su, Peng Tao, Yi Han, Cheng-Hui Zeng, and Sheng-Liang Zhong
Volume 2016, Article ID 3714041, 5 pages

Editorial

Functional Nanomaterials for Energy Conversion and Storage

Tianyi Kou,¹ Gongming Wang,² Xihong Lu,³ Yang Song,⁴ and Teng Zhai⁵

¹University of California, Santa Cruz, CA 95064, USA

²University of California, Los Angeles, CA 90095, USA

³Sun Yat-sen University, Guangzhou 510275, China

⁴Oak Ridge National Laboratory, Oak Ridge, TN 37831, USA

⁵Nanjing University of Science and Technology, Nanjing 210094, China

Correspondence should be addressed to Teng Zhai; tengzhai@njust.edu.cn

Received 26 July 2016; Accepted 26 July 2016

Copyright © 2016 Tianyi Kou et al. This is an open access article distributed under the Creative Commons Attribution License, which permits unrestricted use, distribution, and reproduction in any medium, provided the original work is properly cited.

Fossil fuels have been the primary energy source in the past thousands of years. However, the nonrenewable feature and air pollutants produced by fossil fuel combustion make fossil fuels unfavorable for long-term usage, under the background of global population booming. In order to relieve this issue, it is urgent to develop renewable energy storage/conversion devices with both high energy and power delivering performances. A variety of energy storage/conversion devices have been developed such as lithium ion batteries and supercapacitors. Lithium ion batteries usually deliver higher energy density around 200 Wh/kg because of the bulk intercalation of a large amount of lithium ions. However, resulting from the sluggish bulk faradaic reactions, a high degree of bulk intercalation of lithium ions should be guaranteed by the lower charging and discharging rate. This fact leads to the inferior power delivering ability of lithium ion batteries with typical power density on the level below 1kW/kg. To supplement the drawbacks of power delivering in lithium ion batteries, supercapacitors have been therefore put forward to aim at high rate charging and discharging. Due to the fast interface charge storage mechanism, supercapacitors can provide power density on the level of tens of kW/kg, much higher than that in lithium ion batteries. Unfortunately, the fast interfacial charge storage mechanism in supercapacitors is contradictory to sluggish bulk charging mechanism which results in lower energy density for supercapacitors and several Wh/kg are usually seen.

In the scenario of both intrinsic problems existent in lithium ion batteries and supercapacitors, a balance between energy and power should be required so that energy density

is boosted and at the same time decent power density is also kept. A key method to resolve this long-standing problem should reside in developing novel nanostructured electrodes for these electrochemical energy storage devices. High conductivity, fast ions intercalation channel, highly electrolyte ions accessible surface, rich faradaic reactions sites, and stable long duration charging/discharging performance are indispensable to high efficient lithium ion batteries or supercapacitors. And these are also the common goals for materials scientists when developing state-of-the-art electrodes. Based on these goals, this special issue includes reports selected by the guest editors team which are focused on the advanced nanomaterials synthesis or/and the application of nanostructured electrodes in energy storage/conversion devices such as lithium ion batteries and supercapacitors. We hope the work summarized in the issue can provide some new ideas for our science community and inspire our colleagues studying functional materials for energy storage/conversion.

Acknowledgments

The guest editors team sincerely appreciates the contribution and efforts from all of the authors and referees to make this special issue a success.

Tianyi Kou
Gongming Wang
Xihong Lu
Yang Song
Teng Zhai

Research Article

Continued Multicolumns Bioleaching for Low Grade Uranium Ore at a Certain Uranium Deposit

Gongxin Chen, Zhanxue Sun, and Yajie Liu

State Key Laboratory Breeding Base of Nuclear Resources and Environment, East China University of Technology, Nanchang, Jiangxi 330013, China

Correspondence should be addressed to Gongxin Chen; cgx95121@163.com

Received 26 April 2016; Revised 19 June 2016; Accepted 22 June 2016

Academic Editor: Tianyi Kou

Copyright © 2016 Gongxin Chen et al. This is an open access article distributed under the Creative Commons Attribution License, which permits unrestricted use, distribution, and reproduction in any medium, provided the original work is properly cited.

Bioleaching has lots of advantages compared with traditional heap leaching. In industry, bioleaching of uranium is still facing many problems such as site space, high cost of production, and limited industrial facilities. In this paper, a continued column bioleaching system has been established for leaching a certain uranium ore which contains high fluoride. The analysis of chemical composition of ore shows that the grade of uranium is 0.208%, which is lower than that of other deposits. However, the fluoride content (1.8% of weight) is greater than that of other deposits. This can be toxic for bacteria growth in bioleaching progress. In our continued multicolumns bioleaching experiment, the uranium recovery (89.5%) of 4th column is greater than those of other columns in 120 days, as well as the acid consumption (33.6 g/kg). These results indicate that continued multicolumns bioleaching technology is suitable for leaching this type of ore. The uranium concentration of PLS can be effectively improved, where uranium recovery can be enhanced by the iron exchange system. Furthermore, this continued multicolumns bioleaching system can effectively utilize the remaining acid of PLS, which can reduce the sulfuric acid consumption. The cost of production of uranium can be reduced and this benefits the environment too.

1. Introduction

Biological metallurgy technology does not have a long history in leaching minerals. Bioleaching is one of the most active technologies [1]. For introduction of bacterial leaching process at uranium leaching can enhance the kinetics of leaching and strengthen its process, bioleaching has been paid great attention in uranium industry in recent years. By this technology, the leaching time can be shortened and the recovery of minerals can be improved and the production costs can be reduced. This technology has been used in the production [2, 3] or is still in the laboratory research stage [4]. Leaching in columns simulates percolation leaching because the conditions are very similar to those in the heap [5].

In China, bioleaching has been greatly improved in uranium industry. However, we still face some keys which greatly impact this technology's application, such as the bacteria adapting to the leaching environment, the tolerance of toxic elements in leaching solution, not well understanding the mechanism and the biochemical kinetics, and the leaching process needing to be optimized [6]. In China,

hard-rock-type uranium (such as granite-type) deposits are using heap leaching widely in industry. In this paper, one of the biggest granite uranium deposits located in south China with high fluoride mineral is selected for study. In this deposit's industrial producing practice, acid is often used as irrigating solution. However, the uranium concentration of pregnant leaching solution (PLS) is low. This affects the adsorption efficiency. Another problem is that the acid consumption (about 55 g/kg) is still too high and the recovery is low which lead to the high product cost. The company who owns this deposit needs a new technology to solve this problem. So we try to use continued multicolumns bioleaching in uranium to model multiheaps bioleaching as to improve the production efficiency and reduce the production cost.

2. Materials and Methods

2.1. Materials. A solid sample of uranium ore from the normal production of ore in this deposit plant was used. This type of uranium ore is mainly distributed in Taoshan

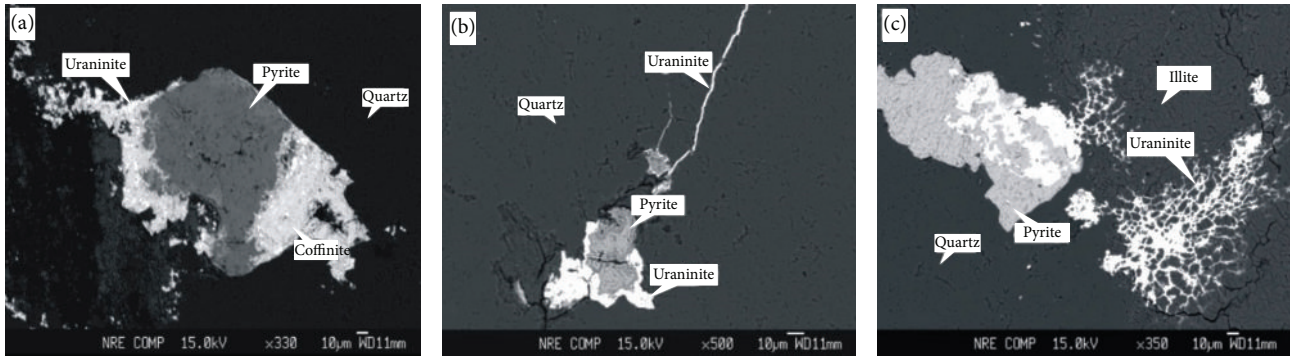


FIGURE 1: Back-scattered electron image by EPMA before leaching. ((a), (b), and (c)) Uranium minerals accompanied by pyrite. (b) Uranium minerals are located in the tiny fractures of quartz. (c) Uranium minerals are located in the tiny fractures of illite. ((a) and (b)) Images from Zhihua Wang and Baoqin Hu (2013) and (c) Xinbo Zhao (2014).

TABLE 1: Chemical and mineralogical composition of the ore sample used in column bioleaching.

Composition	Weight%	Mineralogical composition
SiO ₂	78.46	
Al ₂ O ₃	7.14	
Fe ₂ O ₃	1.34	
K ₂ O	2.71	
Na ₂ O	0.25	
FeO	0.7	
MgO	0.5	Quartz
P ₂ O ₅	0.021	Potash feldspar
TiO ₂	0.03	Fluorite
CaO	4.2	Calcite
U	0.208	
BaO	0.01	
S	0.16	
F	1.8	
CO ₂	1.2	
S ⁻¹⁻²	0.1	

Zhuguangshan mineralization belt. It has a relationship with the granite of Yanshan period in space and genesis. Uranium mineralizations are product in low level structure of tectonic fault, which mainly contain pitchblende, coffinite, fluorite silicate uranium, lead, and zinc.

Table 1 shows the chemical and mineralogical composition of the sample. Elemental analysis of the sample by a wet chemical method involving hydrofluoric acid digestion and measurement by atomic absorption spectrophotometry (AAS; Perkin Elmer, Model 3100) indicated that the major constituent of the sample was SiO₂, weight of more than 78%, and the second is Al₂O₃, weight of 7%, and a small amount of FeO, S, Na₂O, P₂O₅, MgO, TiO₂, BaO, and so forth. Fluoride element analysis of the sample by potassium hydroxide digestion and measurement by fluoride electrode indicated that fluoride weight is high (1.8%). This indicates these ores contain lots of fluoride mineral. It can have certain influence on the growth of microorganisms. The sulfur weight is 0.16% and the uranium weight is 0.208%. This uranium ore

belongs to a low grade type. The sample was also analyzed by X-ray diffraction (XRD) using a Panalytical X'Pert PRO MPD with CuK α radiation (40 kV, 50 mA), equipped with automatic divergence slit, sample spinner, and a graphite secondary monochromatic and proportional detector [7]. XRD analysis indicated that silica (SiO₂), potash feldspar (K(AlSi₃O₈)), fluorite (CaF₂), and calcite (CaCO₃) were the dominant phases present.

Back-scattered electron image shows that the uranium minerals are located in the tiny fractures of the ore and they are accompanied by pyrite as shown in Figure 1. This indicates that once pyrite is leached; the surface area of those uraninite and coffinite minerals will be greatly increased. Those tiny fractures around uranium minerals will be enlarged as well. Furthermore, when the pyrite is dissolved or, more precisely, is oxidized, ferric iron is produced which can offer good oxidizing for those reduced-type uranium minerals. Iron oxidizing bacteria are a good worker who can do this job.

In our study, a strain of mesospheric iron oxidizing bacteria (*Acidithiobacillus ferrooxidans* mixed with *Leptospirillum ferriphilum*, named B3mYPIQ) provided by our university was used throughout the investigations. It was domesticated by PLS with high fluorine concentration (3 to 4 g/L of total F). *Acidithiobacillus ferrooxidans* is Gram-negative bacteria [8], characterized by nonsporulating rods, 0.5–0.6 μm wide and 1.0–2.0 μm long with rounded ends, and occurring singly or in pairs or rarely in short chains. The bacteria are also known to be motile by means of a single polar flagellum. All of these characteristics were observed during the isolation of the strain used. The compositions of the nutrient growth medium are from PLS at this deposit.

2.2. Experimental Bioleaching. Leaching system consists of serial organic glass columns with a diameter of 150 mm and a height of 2 m. In the bottom of each column gravel and pebbles were cushioned at 10 cm height. The ratio of the internal diameter of the column to the height of ore is important for the leaching solution percolates more efficiently. It has been established that this ratio must be greater than 4 and not in excess of 20 in order to avoid any effects of the wall [9, 10]. As a consequence, a ratio of 10 was adopted in

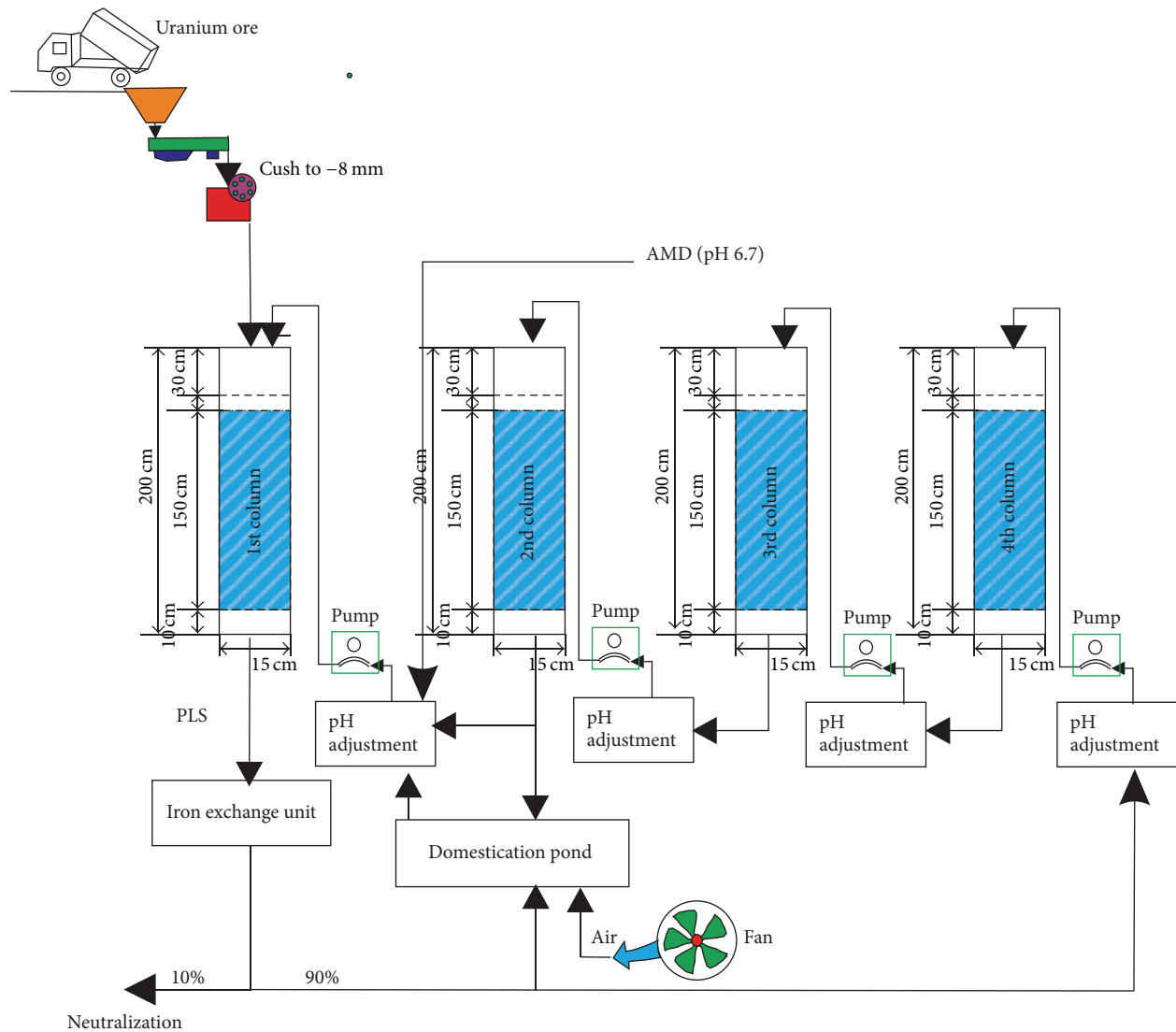


FIGURE 2: Schematic of continued multicolumn bioleaching system.

these experiments. In each column, the ore is built up 150 cm high and on top there are loading cobble and gravel 10 cm high. Plastic film was covered on the top of both leaching column and liquid collecting tank to reduce evaporation. The irrigation is powered by a peristaltic pump. The speed of pump is changed in the test to control the time and intensity. Test process is 120 d for the uranium leaching cycle, consisting of four columns as shown in Figure 2. The test process and the specific implementation process are as follows: 4 columns are, respectively, set, first column (acid leaching stage and domestication stage), second column (bioleaching stage), third column (bioleaching stage), and the last column (final leaching stage). Each column acidification stage is 30 d, and domestication stage is 30 d, and bioleaching stage is 30 days and final leaching stage is 30 days. After 120 d of leaching, the last column was unloaded out of this system and a new column was added in. Before irrigation of the former column, the pH of PLS should be adjusted to 1.8. For comparison, a single column test is conducted at the same time. Sample

volumes of liquid were extracted periodically and the pH and redox potential (Eh) were measured. The U_3O_8 , Fe^{Total} , and Fe^{2+} content were also analyzed.

3. Results and Discussion

3.1. Acid Consumption during Bioleaching. There exist consumptive acid minerals such as calcite (chemical analysis of the weight of CO_2 1.2%, of calcite about 2.7%) in this ore. Thus, during bioleaching, the pH of irrigating solution in the column will be increased. When the pH value of irrigating solution reaches over 2.5, the ferric iron will be precipitated as goethite. As shown in Figure 3, the pH values of PLS in the first 5 leaching days decrease very fast but are still greater than 4. In the next five days, pH values decrease slowly compared with the former 5 days and reach around 2.0 at the 10th day. This indicates that during this stage most easily consumptive acid minerals such as calcite of this ore are almost reacted by acid in the large fractures. However,

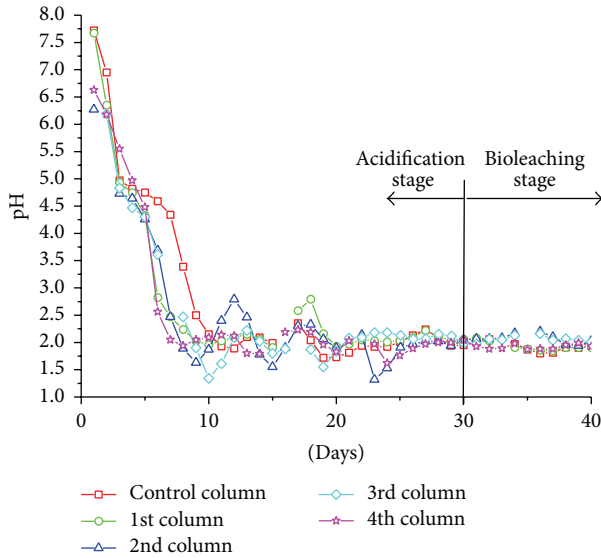


FIGURE 3: pH value of the PLS in the first 40 days.

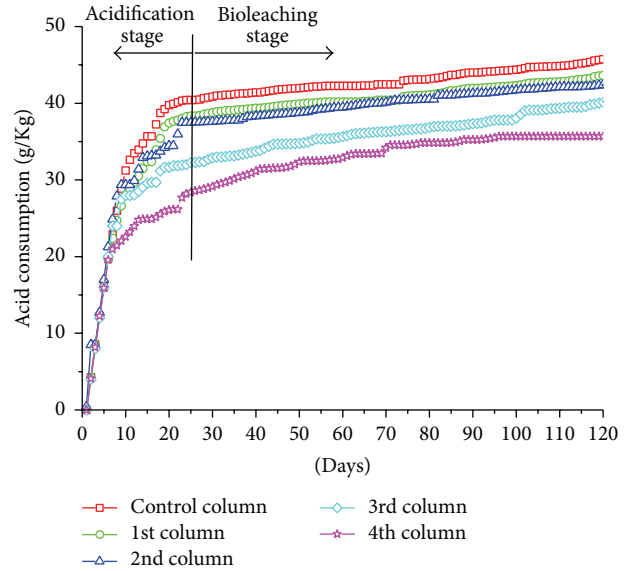


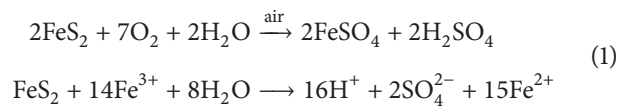
FIGURE 4: The acid consumption with the column's order.

some consumptive acid minerals in small fractures will be reacted more slowly. On the other hand, the mesospheric iron oxidizing bacteria of *Acidithiobacillus ferrooxidans* and *Leptospirillum ferriphilum* which are used in this experiment are more active in pH of 1.5 to 2 than in other pH values. Therefore, the pH of irrigating solution cannot be lower than 1.5 or higher than 2. When pH is lower than 1.5, the precipitation of some jarosite-type basic compounds will be found in the column [11]. These type of precipitations are difficult to be dissolved by strong acid and that will decrease the permeability of the column [12]. The uranium minerals will be wrapped up by them. As a consequence, they hinder the irrigating solution to react with the uranium minerals and the uranium recovery is decreased. In acidification stage, therefore, the acid concentration should be decreased as well. In our experiment, the concentration of acid of irrigating solution is reduced from 40 g/L to 5 g/L in 10 days for those easier reactant consumptive acid minerals in small fractures and from 5 g/L to 3 g/L in the next around 20 days for those slow reactants in small fractures. Under these circumstances, the precipitation of both goethite and jarosite-type basic compounds will not occur in the next bioleaching stage and the bacterium will grow in the column as bacteria are adapted to this pH and the culture from the irrigating solution (PLS of pH adjustment).

After 120 days' leaching, the total acid consumption for each column is 45.73, 43.74, 42.38, 40.23, and 33.6 g/kg, respectively, in this type of system as shown in Figure 4. In the first 10 days of acidification stage, acid consumption curve increases fast linearly and is up to around 30 g/kg. In the next 20 days, acid consumption increases still fast but it is lower than that in the first 10 days. And then in the next bioleaching stage, acid consumption still increase slowly because some acid needs to be added in the bacteria domestication pond for pH adjustment and there are still some consumptive acid minerals in tiny fracture which are not reacted by acid in

the former stage. The total acid consumption of 1st column is highest and that of the last column is lowest. This result shows that the acid consumption is in good accordance with the column's order and this system can help to save acid consumption. Moreover, the acid consumption of the 1st column and that of the 2nd column are very similar. Because the first column is the initial column in this type of system and the acid amount of PLS from the 1st column is small, the irrigating solution of 2nd column needs to add more acid for pH adjustment using PLS from the 1st column. The acid of the 3rd and 4th column, however, can accumulate acid from the former columns. It is found that the acid consumption of the later columns will be lower than that of the former ones.

3.2. Redox Potentials (*Eh*) of Irrigating Solution and PLS. During this experiment, both redox potentials of irrigating solution and PLS are measured in each day. Redox potentials of from 1st column to 4th column are presented in Figures 5(a), 5(b), 5(c), and 5(d). During the acidification process of leaching of uranium, the redox potentials of leaching solution are low and varied between 350 mV and 400 mV (versus SCE). In this type of ore, many minerals such as pyrite and urinate belong to reduced substances. In the leaching progress, they can be oxidized by ferric iron or O_2 of the solution [13]. In the process of acidification, reducing substances in ore are leached into the PLS and decrease *Eh* of PLS:



As shown in Figure 5, in each column in the bioleaching process, redox potentials increased obviously compared with the former acid leaching period, and they reach 500 mv (SCE) rapidly. After bioleaching period, redox potentials of PLS are significantly higher than the correspondence leaching solutions. This indicates that the bacteria grow well in these

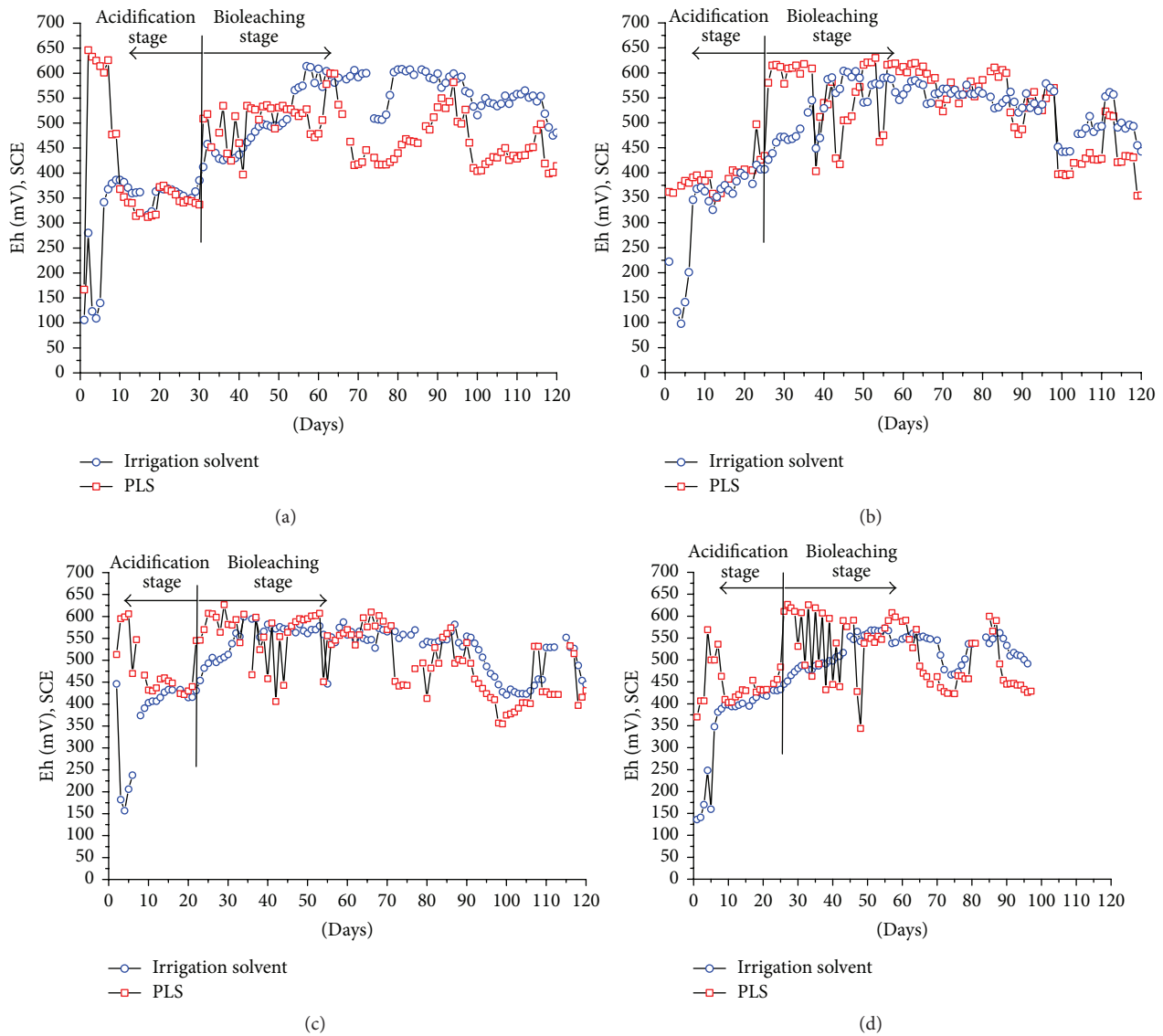
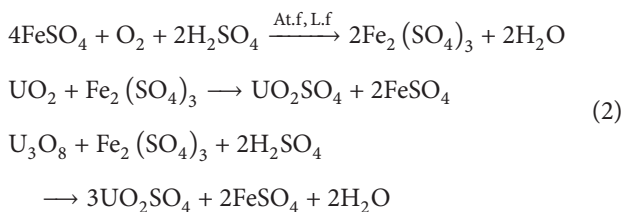


FIGURE 5: Relationship between each column of Eh value. (a) 1st column; (b) 2nd column; (c) 3rd column; (d) 4th column.

columns. They enhance the ferrous oxidizing and produce ferric iron to oxidize pyrite and uraninite as shown in the following equations [14]:



During bioleaching period, redox potentials increase and uranium concentrations are also increased as shown in Figures 5 and 6. With the variation of Eh of irrigating solution, the uranium concentration is varied too. Therefore, high Eh value is good benefit for oxidizing fourth valence uranium [15]. Normally, the bacteria need 24 hr of cultivation.

In this type of system, one purpose is the increasing redox potentials of this system; the other purpose is that the iron oxidizing bacteria can grow in the column. The irrigation frequency is 12 hr/day. Irrigation method is that one day we use bacteria as irrigation solution after domestication by air in 24 hours for increasing the activity of bacteria and also increasing the redox potential, and the next day we use PLS from the former column which contains ferrous iron as the nutrition for those iron oxidizing bacteria in order to help the bacteria grow in the ore. The redox potential of PLS is much lower than that of bacteria culture. For the bacteria culture and the PLS as irrigation solution changed in turns, the red curves of irrigation solution are more fluctuant than blue curve of PLS.

3.3. Uranium Leaching. In the acidification period, there occurs a uranium concentration peak. Most of sixth valence

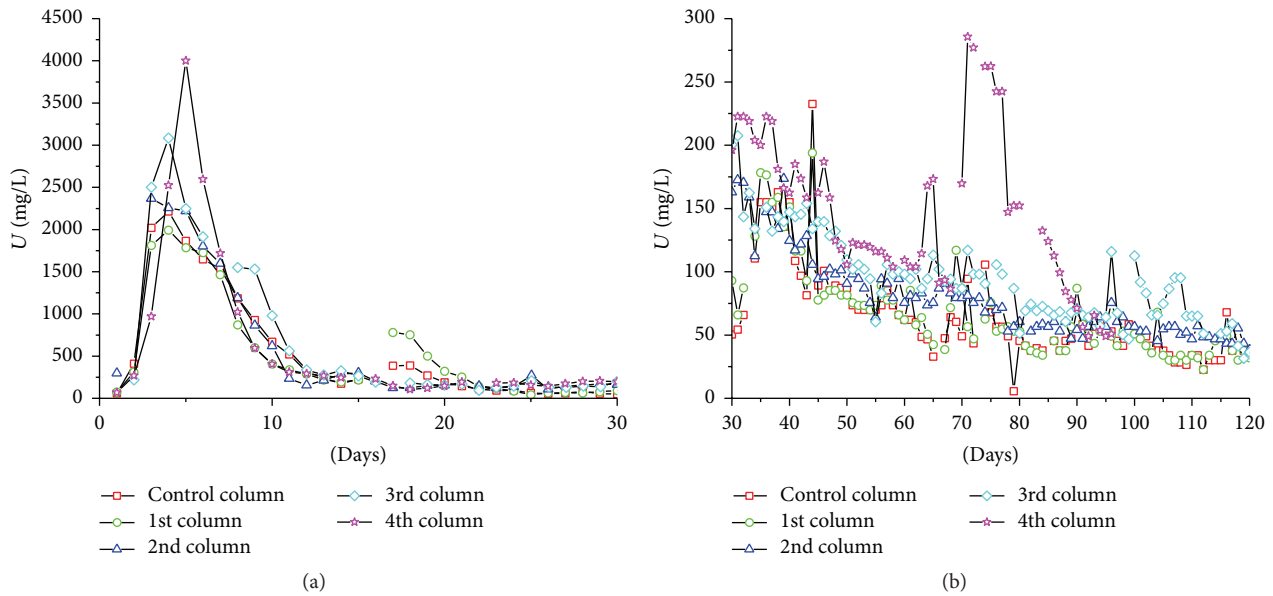


FIGURE 6: Uranium concentration of PLS for each column during the leaching. (a) From 1 to 30 days and (b) from 31 to 120 days.

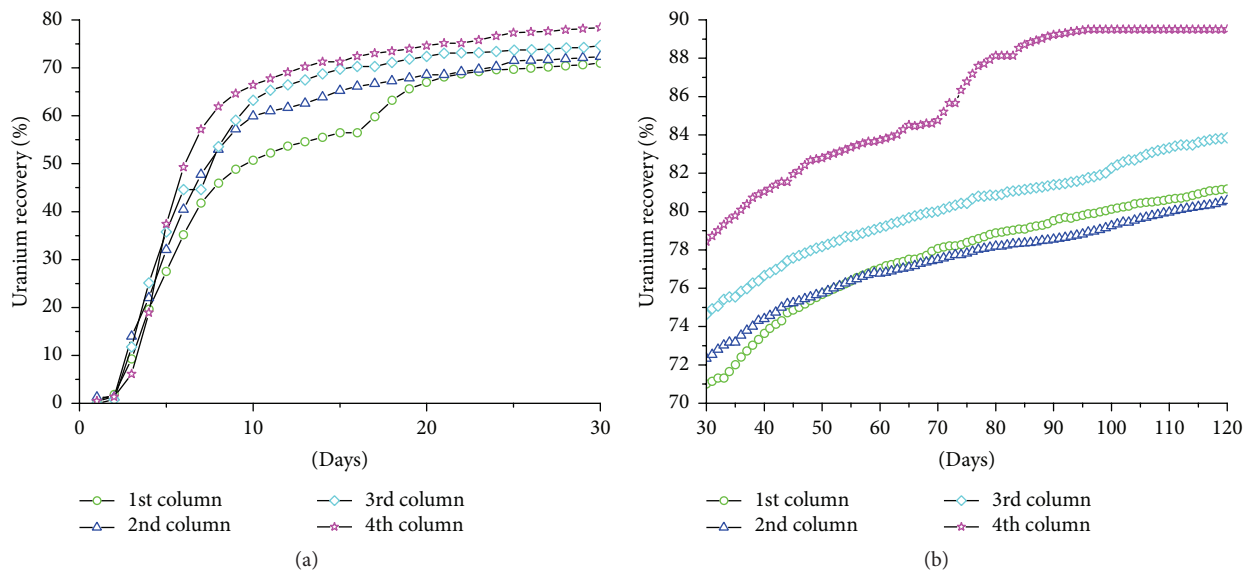


FIGURE 7: Uranium recovery for each column during the leaching. (a) In the first 30 days; (b) in the next 90 days.

uranium minerals are leaching because they can dissolve in acid normally. In this period, the redox potential and the concentration of uranium have no correlation relationship which are presented in Figure 6(a). There is a big peak for uranium concentration for each column in the fifth day. However, the peak of 4th column is the highest one and that of the 3rd column is the second. The peaks for the control column and the 1st column are much lower than the later columns. This is because the later column utilized the PLS of the former column which contains ferric iron as stronger oxidizing agent. The other reason is that the bacteria can adapt more easily to the leaching environment which contains more fluorine and other toxic ions after adopting extreme

toxic iron environment in former column. That is, bacteria activity was enhanced after they underwent the former column.

Figure 6(a) shows the uranium concentration of PLS with different column in bioleaching stage. The U concentration of PLS from 4th column is higher than those of others. The average uranium concentration of PLS is 67 mg/L of 1st column, 80 mg/L of 2nd column, 95 mg/L of 3rd column, and 147 mg/L of 4th column. Obviously, the average uranium concentration of PLS of later column is higher than that of the former one. This system can increase the uranium concentration of PLS. This is good for the iron exchange system to recover the uranium.

In acid leaching stage (in the first 30 days), about 65% to 70% totally were leached in the first 30 days as shown in Figure 7(a). The major uranium mineral is pitchblende which can be easily leached by acid with O_2 . Because the PLS contains bacteria and ferric iron from the former column as irrigation solution, in this stage, uranium can be leached more efficiently which has more ferric iron or bacteria. Thus, the recovery of 4th is greater than that of 3rd column, and that of 3rd is greater than 2nd column and so on.

After 120 days of bioleaching, the uranium recovery was 81.0% for the 1st column, 81.8% for the 2nd column, 87.5% for the 3rd column, and 89.5% for the 4th column, respectively, as shown in Figure 7(b). The uranium recovery of the 4th column is over 8.5% more than that of the 1st column. The result demonstrates that the highest leaching of base metals is achieved at low pH values under high redox conditions where ferric iron remains in solutions [16].

4. Summary

The continued multicolumns bioleaching is seen to be very effective for leaching uranium. After 120 d of continued multicolumns bioleaching, the acid consumption of the last column was 33.6 g/kg, which is much less than that of acid leaching. The uranium recovery is highly leached (89.5%). The highest uranium concentration (4000 mg/L) is that from the 4th column. This technology can effectively enhance both bacteria activity and uranium concentration of PLS. It improved the iron exchange system to recover uranium. Furthermore, this continued multicolumns bioleaching system can reuse the acid of PLS and reduce the acid consumption. The cost can be reduced by this technology.

Competing Interests

The authors declare that they have no conflict of interests.

Acknowledgments

This work was financially supported by National 973 Plans (Grant no. 2015CB453000), Joint Fund Project of National Natural Science Foundation of China (U1501231), the Science and Technology Project of Jiangxi Province Education Department (no. GJJ12752), Science and Technology Project of Jiangxi Province (no. 20133BFB29004), the International Science and Technology Cooperation Project of China (no. 2011DFR60830), China Postdoctoral Science Foundation of Jiangxi Province (JX2014KY48), and Project of Key Laboratory of Radioactive Geology and Exploration Technology Fundamental Science for National Defense (Z1508).

References

- [1] A. Potysz, P. N. L. Lens, J. van de Vossenberg et al., "Comparison of Cu, Zn and Fe bioleaching from Cu-metallurgical slags in the presence of *Pseudomonas fluorescens* and *Acidithiobacillus thiooxidans*," *Applied Geochemistry*, vol. 68, pp. 39–52, 2016.
- [2] S. Ilyas, J.-C. Lee, and R.-A. Chi, "Bioleaching of metals from electronic scrap and its potential for commercial exploitation," *Hydrometallurgy*, vol. 131-132, pp. 138–143, 2013.
- [3] G. Zou, S. Papirio, X. Lai et al., "Column leaching of low-grade sulfide ore from Zijinshan copper mine," *International Journal of Mineral Processing*, vol. 139, article 2730, pp. 11–16, 2015.
- [4] M. L. Rodrigues, K. C. Lopes, H. C. Leônico, L. A. Silva, and V. A. Leão, "Bioleaching of fluoride-bearing secondary copper sulphides: column experiments with *Acidithiobacillus ferrooxidans*," *Chemical Engineering Journal*, vol. 284, pp. 1279–1286, 2016.
- [5] J. A. Muñoz, M. L. Blázquez, A. Ballester, and F. González, "A study of the bioleaching of a Spanish uranium ore. Part III: column experiments," *Hydrometallurgy*, vol. 38, no. 1, pp. 79–97, 1995.
- [6] Z.-J. Peng, R.-L. Yu, G.-Z. Qiu et al., "Really active form of fluorine toxicity affecting *Acidithiobacillus ferrooxidans* activity in bioleaching uranium," *Transactions of Nonferrous Metals Society of China*, vol. 23, no. 3, pp. 812–817, 2013.
- [7] Y. Yang, W. Liu, S. K. Bhargava, W. Zeng, and M. Chen, "A XANES and XRD study of chalcopyrite bioleaching with pyrite," *Minerals Engineering*, vol. 89, pp. 157–162, 2016.
- [8] J. Park, Y. Han, E. Lee et al., "Bioleaching of highly concentrated arsenic mine tailings by *Acidithiobacillus ferrooxidans*," *Separation and Purification Technology*, vol. 133, pp. 291–296, 2014.
- [9] Abhilash, B. D. Pandey, and A. K. Singh, "Comparative performance of uranium bioleaching from low grade indian apatite rock in column and bioreactor," *Energy Procedia*, vol. 39, pp. 20–32, 2013.
- [10] M. Shahrabi-Farahani, S. Yaghmaei, S. M. Mousavi, and F. Amiri, "Bioleaching of heavy metals from a petroleum spent catalyst using *Acidithiobacillus thiooxidans* in a slurry bubble column bioreactor," *Separation and Purification Technology*, vol. 132, pp. 41–49, 2014.
- [11] L. Castro, M. L. Blázquez, F. González, J. A. Muñoz, and A. Ballester, "Reductive leaching of jarosites by *Aeromonas hydrophila*," *Minerals Engineering*, vol. 95, pp. 21–28, 2016.
- [12] L. Gunneriusson, Å. Sandström, A. Holmgren, E. Kuzmann, K. Kovacs, and A. Vértes, "Jarosite inclusion of fluoride and its potential significance to bioleaching of sulphide minerals," *Hydrometallurgy*, vol. 96, no. 1-2, pp. 108–116, 2009.
- [13] V. Fonti, A. Dell'Anno, and F. Beolchini, "Does bioleaching represent a biotechnological strategy for remediation of contaminated sediments?" *Science of the Total Environment*, vol. 563-564, pp. 302–319, 2016.
- [14] J. A. Muñoz, F. González, M. L. Blázquez, and A. Ballester, "A study of the bioleaching of a Spanish uranium ore. Part I: a review of the bacterial leaching in the treatment of uranium ores," *Hydrometallurgy*, vol. 38, no. 1, pp. 39–57, 1995.
- [15] J.-U. Lee, S.-M. Kim, K.-W. Kim, and I. S. Kim, "Microbial removal of uranium in uranium-bearing black shale," *Chemosphere*, vol. 59, no. 1, pp. 147–154, 2005.
- [16] A. Cecal, K. Popa, M. Craus, S. Patachia, and R. T. Moraru, "Bioleaching of UO_2^{2+} ions from a Romanian poor uranium ore," *Journal of Radioanalytical and Nuclear Chemistry*, vol. 254, no. 1, pp. 81–84, 2002.

Research Article

The Comparative Study of Electrochemical Capacitance Performance between Sulphur-Doped Co_3O_4 and CoS Anodes

Wei Xu,¹ M. A. Khan,² Jiahui Chen,¹ Yongbing Long,³ Gui Xu,⁴ Yu Bai,¹ Xiaodong Zhang,¹ Zhenmin Qiu,¹ Sennian Lin,¹ and Donghua Fan¹

¹School of Applied Physics and Materials, Wuyi University, Jiangmen, Guangdong 529020, China

²Department of Physics, Hi-Tech. Laboratory, University of AJK, Muzaffarabad 999010, Pakistan

³School of Electronic Engineering, South China Agricultural University, Guangzhou 510642, China

⁴Baotou Power Supply Bureau, Jianshe Road, Baotou, Inner Mongolia 014030, China

Correspondence should be addressed to Wei Xu; weixugreat@126.com and Yongbing Long; yongbinglong@126.com

Received 5 May 2016; Accepted 12 June 2016

Academic Editor: Gongming Wang

Copyright © 2016 Wei Xu et al. This is an open access article distributed under the Creative Commons Attribution License, which permits unrestricted use, distribution, and reproduction in any medium, provided the original work is properly cited.

Anode materials with high capacitance performance are highly desirable for supercapacitors (SCs). In this work, nanomaterials cobalt sulfide (CoS), sulphur-doped Co_3O_4 (S- Co_3O_4), and Co_3O_4 were fabricated on a carbon cloth substrate by hydrothermal method. The composition and morphology of the material were characterized by X-ray diffraction (XRD) patterns and Scanning Electron Microscope (SEM). The electrochemical measurements were performed in a three-electrode system. The result shows that CoS nanomaterial as anode is of the best electrochemical performance, achieving areal capacitance of 1.98 F/cm^2 at 2 mA/cm^2 in a 5 M LiCl solution. Moreover, the CoS anode has long-term cycling stability with more than 85.7% capacitance retention after 10000 cycles, confirming its larger capacitance, good redox activity, and electrochemical stability.

1. Introduction

With the ever increasing energy depletion and aggravating environmental issue, considerable attention was paid to energy storage and conversion and intense research has been concentrated on this field [1, 2]. Of them, supercapacitors, with their advantages of high-power density, excellent reversibility, fast recharge ability, and long cycle life and their potential application in the field of high-power electronic devices, emergency power supplies, and hybrid electric vehicles, have attracted significant research attention [1–6]. However, the relatively low energy density of SCs impeded their further development and application. Therefore, based on not sacrificing the power density and cycle life, it is highly desirable to increase the energy density of SCs. According to the equation of energy density, $E = 0.5 \text{ CV}^2$, the energy density of a SC can be improved if the output voltage and/or the capacitance is increased [7]. An

effective approach to increase the voltage is to use organic and ionic liquid electrolytes [8–10], such as tetraethylammonium tetrafluoroborate in acetonitrile [9] or lithium perchlorate in propylene carbonate [10]. Although the voltage window of up to 3 V can be reached, the disadvantages such as high cost, poor ionic conductivity, and high toxicity prevent SCs from further applications. A hopeful alternative is to develop asymmetric supercapacitors (ASCs) based on the environmentally friendly aqueous electrolyte. As compared with symmetric supercapacitors (SSCs), ASCs combined two electrodes with different voltage to increase the operating voltage in aqueous electrolyte which is up to 2 V [11, 12]. Great efforts have been made to research various materials, such as graphene- MnO_2 //activated carbon nanofiber, Ni(OH)_2 -graphene and graphene, V_2O_5 //active carbon, and MnO_2 // FeOOH [11, 13, 14], for their application on ASCs. However, previous studies have been mainly focused on the development of high-performance cathode materials [15]. By

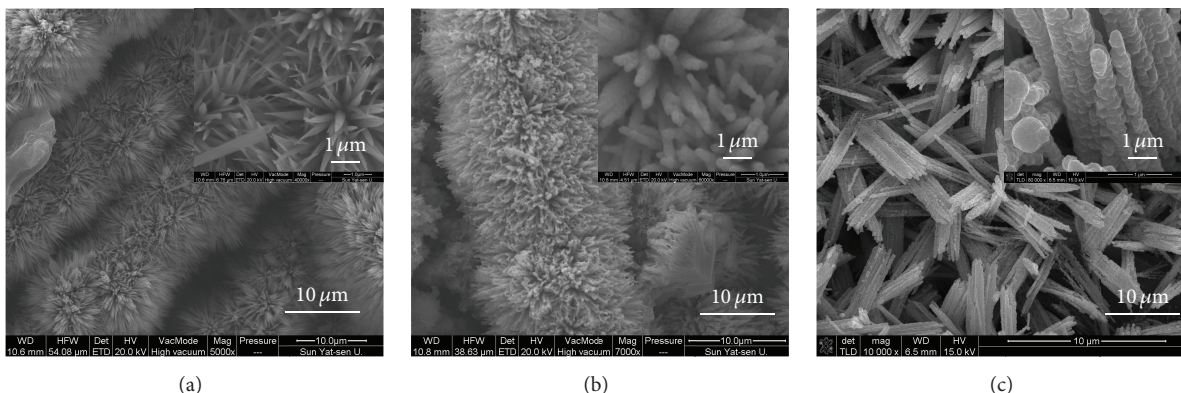


FIGURE 1: SEM images of (a) Co_3O_4 nanomaterials, (b) $\text{S-Co}_3\text{O}_4$ nanomaterials, and (c) CoS nanomaterials on a carbon cloth.

comparison, explorations for anode materials have been very few as yet. The most common anode materials are carbon-based nanomaterials, yet they suffer from the relatively low capacitance which prevents ASCs from further enhancement in energy density. Therefore, it is necessary to explore novel anode materials to advance the performance of ASCs.

As promising, environmentally friendly, and low-cost candidates, cobalt sulfides can also be grown on a flexible conductive substrate, but they have not been systematically studied as anode materials yet [16]. In this paper, we reported the fabrication of Co_3O_4 , sulphur-doped Co_3O_4 , and CoS and compared their electrochemical performance as anodes of ASCs. The result shows that CoS nanomaterial is of the best electrochemical performance when used as anode, achieving areal capacitance of 1.98 F/cm^2 at 2 mA/cm^2 and excellent long-term cycling stability in a 5 M LiCl solution.

2. Experimental

All reagents used in the experiment are up to the standard of analytical grade that were used without any further purification. Co_3O_4 were fabricated on a carbon cloth substrate by using hydrothermal method. First, 5 mmol of $\text{Co}(\text{NO}_3)_2 \cdot 6\text{H}_2\text{O}$, 10 mmol of NH_4F , and 25 mmol of $\text{CO}(\text{NH}_2)_2$ were dissolved in 50 mL of DI water under stirring, respectively. After 10 minutes of slight stirring, a Teflon-lined stainless-steel autoclave of 25 mL capacity was filled with 20 mL of homogeneous solution prepared above. Then, carbon cloth ($2 \text{ cm} \times 3 \text{ cm}$) was cleaned by ethanol, deionized water, and using ultrasonic treatment in turn and then immersed into the reaction solution. Subsequently, the autoclave was sealed and heated at 120°C for 5 h and allowed to cool down to room temperature. After the reaction, a layer of Co_3O_4 film was grown on the carbon cloth substrate and then washed with DI water and dried at 60°C . The $\text{S-Co}_3\text{O}_4$ was prepared by immersing a piece of Co_3O_4 ($2 \text{ cm} \times 3 \text{ cm}$) into a 25 mL autoclave containing 0.1 M of $\text{C}_2\text{H}_5\text{NS}$, which was then sealed and heated at 80°C for 3 h . After cooling down to room temperature, the sample was washed and then dried at 60°C . The CoS was prepared by immersing a piece of Co_3O_4 ($2 \text{ cm} \times 3 \text{ cm}$) into a 25 mL autoclave containing

0.3 M of NaS , which was then sealed and heated at 120°C for 36 h . After cooling down to room temperature, the sample was washed and then dried at 60°C .

3. Material Characterization and Electrochemical Measurement

The composition morphology and structure of the electrode materials were characterized by X-ray diffraction patterns, field-emission SEM (FE-SEM, JSM-6330F), and CV, and galvanostatic charge/discharge measurements were conducted using an electrochemical workstation (CHI 760D). The electrochemical measurements were performed in a three-electrode cell, with the individual sample used as working electrode, a Pt mesh as counter-electrode, and a SCE as reference electrode.

4. Results and Discussion

The SEM images of Co_3O_4 , $\text{S-Co}_3\text{O}_4$, and CoS on carbon cloth are shown in Figures 1(a), 1(b), and 1(c), respectively. It can be seen that the individual carbon fiber was uniformly wrapped by many nanowires with a diameter between 300 and 500 nm and length up to $4 \mu\text{m}$. The obvious difference in morphology between the SEM images of Co_3O_4 , $\text{S-Co}_3\text{O}_4$, and CoS can be observed. The SEM images of the $\text{S-Co}_3\text{O}_4$ and CoS are much rougher compared with that of Co_3O_4 ; furthermore, the SEM image of CoS is rougher than that of $\text{S-Co}_3\text{O}_4$ (Figures 1(b) and 1(c)).

Figure 2 shows the X-ray diffraction (XRD) patterns of the Co_3O_4 , $\text{S-Co}_3\text{O}_4$, and CoS samples. The peaks of Co_3O_4 and $\text{S-Co}_3\text{O}_4$ samples can be indexed to the standard card (JCPDS Card no. 42-1467), which are in good accordance with cubic spinel Co_3O_4 phase. In addition, the peak shift can be observed in $\text{S-Co}_3\text{O}_4$ as compared to the peak of Co_3O_4 , especially for (311) crystal face, confirming the S doping in the material. Energy dispersive spectrometry (EDS) elemental spectrum was performed to provide the doping amount of S ($26.08 \text{ wt}\%$). The peaks of CoS sample can be indexed to the standard card (JCPDS Card no. 65-3418), which are in good agreement with spinel CoS structure.

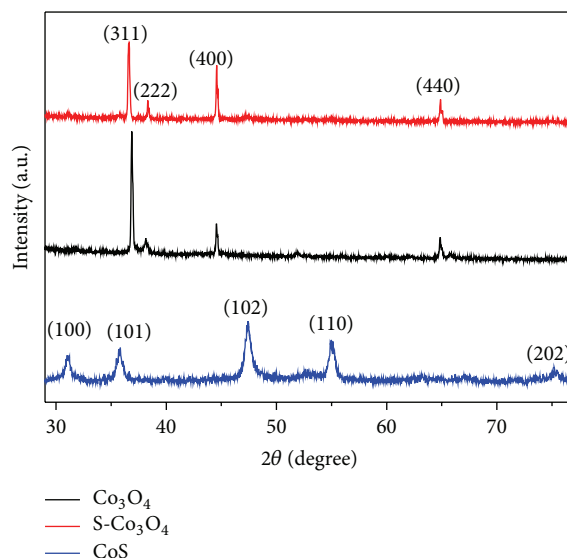


FIGURE 2: XRD spectra collected for Co_3O_4 , $\text{S-Co}_3\text{O}_4$, and CoS anodes.

The electrochemical properties of the Co_3O_4 , $\text{S-Co}_3\text{O}_4$, and CoS electrodes were investigated in a three-electrode cell in 5 M LiCl aqueous electrolyte, with a Pt counter-electrode and a SCE reference electrode. Cyclic voltammogram (CV) curves of Co_3O_4 , $\text{S-Co}_3\text{O}_4$, and CoS electrodes at a scan rate of 100 mV/s were compared in Figure 3(a). It is obvious that the current densities of $\text{S-Co}_3\text{O}_4$ and CoS electrodes are substantially higher than that of Co_3O_4 electrode, indicating that substantial enhancement of electrochemical capacitance of $\text{S-Co}_3\text{O}_4$ is originated from the sulphur doping into the Co_3O_4 , and the most significant enhancement of electrochemical capacitance appeared in CoS sample, which is due to the specific surface structure of CoS that can be proven by the rough surface in Figure 1(c). Moreover, the CV profiles of the CoS electrode at various scan rates are rectangularly shaped and remain similar as the scan rate increases from 10 to 200 mV/s (Figure 3(b)), demonstrating the excellent capacitive properties and high-rate capability of the CoS electrode.

Figure 3(c) shows the areal capacitances of the CoS anode at the scan rates from 10 mV/s to 400 mV/s calculated according to its CV curves. The highest areal capacitance of 0.46 F/cm^2 obtained at the scan rate of 10 mV/s is much better than the value (0.27 F/cm^2) obtained for $\text{N-Fe}_2\text{O}_3$ negative electrode and comparable to the excellent value for other negative electrodes, such as $\text{Co}_3\text{O}_4@\text{RuO}_2$ (0.6 F/cm^2) and VOS (0.56 F/cm^2), demonstrating the excellent capacitive performance and a good electrical conductivity of CoS anode [3, 15, 16].

The galvanostatic charge-discharge curves of the $\text{S-Co}_3\text{O}_4$ and CoS electrodes at a current density of 2 mA/cm^2 are shown in Figure 3(d). Compared with the $\text{S-Co}_3\text{O}_4$ electrode, the CoS exhibits slower and more symmetrical charge and discharge curves and a more linear variation of potential versus time, which is also supported by the galvanostatic charge-discharge curves collected for CoS electrode at different

current densities from 2 to 3, 4, 5, 6, 8, and 10 mA/cm^2 (Figure 3(e)), confirming the enhanced capacitance, superior Coulombic efficiency, and excellent reversibility of the CoS electrode at a high current density. The areal capacitance of 0.68 F/cm^2 at current density of 10 mA/cm^2 (shown in Figure 3(e)) is also comparable to $\text{Co}_3\text{O}_4@\text{RuO}_2$ electrode (0.67 F/cm^2), the best value for cobalt sulfides, proving that CoS can be a suitable candidate for anode [16].

Figure 4 demonstrates the long-term cycling performance of the $\text{S-Co}_3\text{O}_4$ and CoS as anodes, respectively. Although the capacitance retention CoS is a little lower than that of $\text{S-Co}_3\text{O}_4$, more than 85.7% of the capacitance retention after 10000 cycles at a scan rate of 200 mV/s still indicates that CoS is of excellent long cycle life.

To further find the electrochemical reason for the phenomenon that the fully converted CoS can significantly improve capacitance (Figure 3(a)), the electrochemical impedance spectroscopy (EIS) measurements on the Co_3O_4 , $\text{S-Co}_3\text{O}_4$, and CoS electrodes were performed (as shown in Figure 5). It is qualitatively demonstrated that the Nyquist plots of the EIS spectra show a similar semicircle in a high frequency range and a spike in a low frequency range. In a high frequency area, the intercept to the x -axis represents the bulk resistance (R_b), while the semicircle corresponds to the double-layer capacitance and charge-transfer resistance (R_{ct}). The R_b resistances of CoS and $\text{S-Co}_3\text{O}_4$ electrodes are smaller than that of pristine Co_3O_4 electrodes, especially for CoS electrode, indicating the enhanced electrical conductivity and the significantly improved capacitance of CoS electrodes.

5. Conclusion

In summary, high-performance CoS anode was demonstrated on woven carbon fabrics. The electrochemical performances of CoS were enhanced dramatically compared with that of Co_3O_4 and were better than that of $\text{S-Co}_3\text{O}_4$.

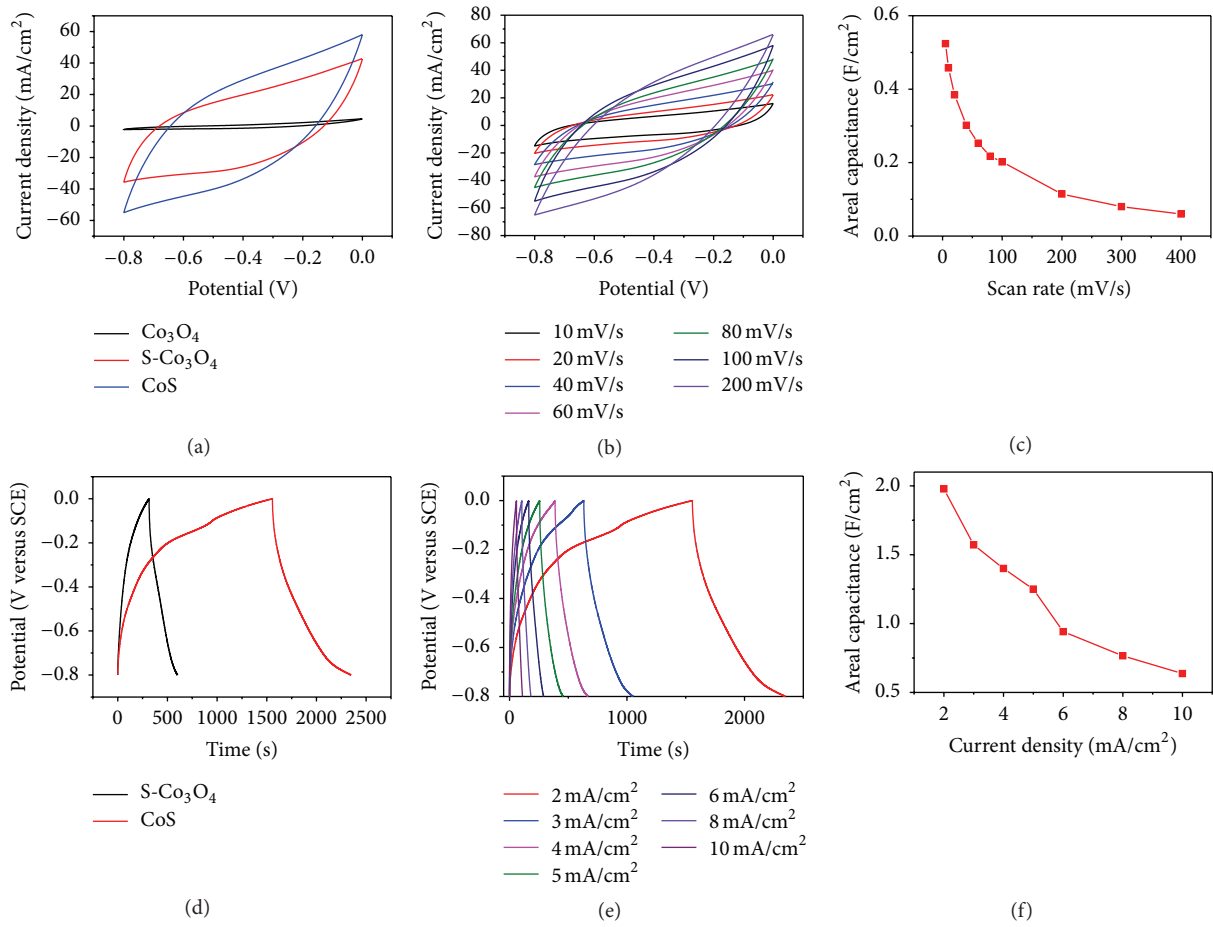


FIGURE 3: (a) CV curves collected for CoS and S-Co₃O₄ anodes at a scan rate of 100 mV/s. (b) CV curves collected for CoS anode at various scan rates. (c) Areal capacitance of the CoS anode as a function of the scan rate. (d) Galvanostatic charge-discharge curves of the S-Co₃O₄ and CoS anodes at a current density of 2 mA/cm². (e) Galvanostatic charge-discharge curves of the CoS anodes collected at different current densities. (f) Areal capacitance of the CoS anode collected from galvanostatic charge-discharge curves as a function of current density.

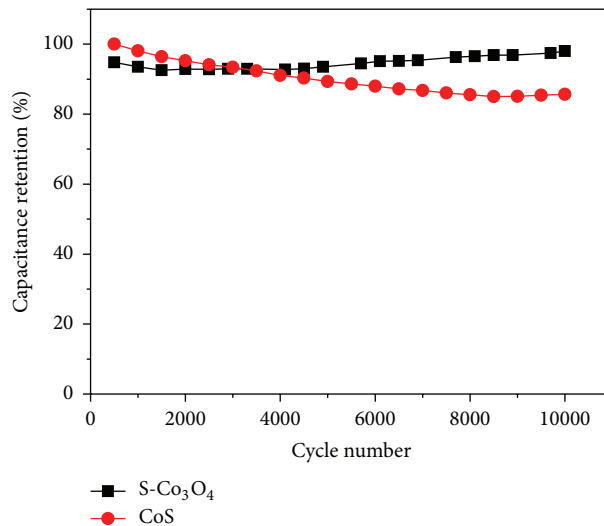


FIGURE 4: Cycling performance of S-Co₃O₄ and CoS anodes collected at a scan rate of 200 mV/s for 10000 cycles.

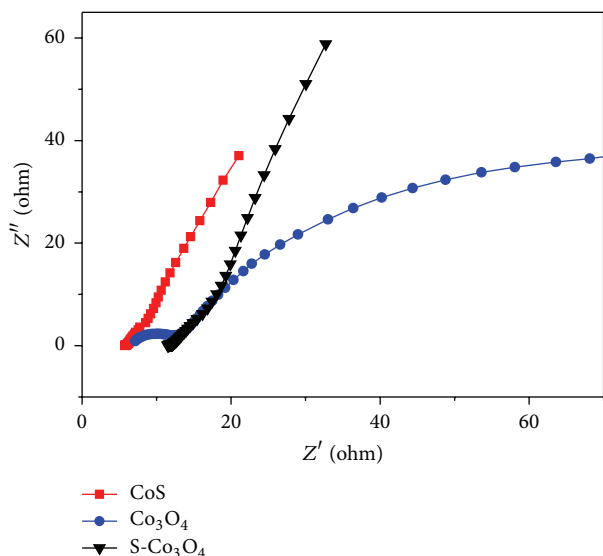


FIGURE 5: Nyquist plots of the Co_3O_4 , $\text{S-Co}_3\text{O}_4$, and CoS anodes.

Moreover, stable rate capability and cycle capability were also achieved. These encouraging performances have access to its applications in high-performance asymmetric supercapacitors, opening up a novel approach to advancing the performance of energy storage devices.

Competing Interests

The authors declare that they have no competing interests.

Acknowledgments

The authors acknowledge the financial support from Guangdong Natural Science Funds for Distinguished Young Scholar (no. 2014A030306005), Natural Science Foundation of Guangdong Province, China (Grant no. S2013010012854), Foundation for High-Level Talents in Higher Education of Guangdong Province, China (Yue Cai-Jiao [2013] 246, Jiang Cai-Jiao [2014] 10), Development Program for Outstanding Young Teachers in Guangdong University (Yue Jiaoshi [2014] 108), Innovative Research Team in University of Guangdong (no. 2015KCXTD027), China's Postdoctoral Science Foundation (no. 2013M540744), Natural Science Foundation of Shanxi Province, China (2014JM7265), Degree and Postgraduate Education Reform Project of Wuyi University (no. 30641015), The Innovation Project of Department of Education of Guangdong Province (no. 2014KTSCX131), and The Mobilization Project of Scientific and Technological Equipment (Yue Cai-Jiao [2015] 356).

References

[1] M. F. El-Kady, V. Strong, S. Dubin, and R. B. Kaner, "Laser scribing of high-performance and flexible graphene-based electrochemical capacitors," *Science*, vol. 335, no. 6074, pp. 1326–1330, 2012.

[2] S. He and W. Chen, "3D graphene nanomaterials for binder-free supercapacitors: scientific design for enhanced performance," *Nanoscale*, vol. 7, no. 16, pp. 6957–6990, 2015.

[3] X. Lu, Y. Zeng, M. Yu et al., "Oxygen-deficient hematite nanorods as high-performance and novel negative electrodes for flexible asymmetric supercapacitors," *Advanced Materials*, vol. 26, no. 19, pp. 3148–3155, 2014.

[4] X. Xia, C. Zhu, J. Luo et al., "Synthesis of free-standing metal sulfide nanoarrays via anion exchange reaction and their electrochemical energy storage application," *Small*, vol. 10, no. 4, pp. 766–773, 2014.

[5] C. Guan, Z. Zeng, X. Li et al., "Atomic-layer-deposition-assisted formation of carbon nanoflakes on metal oxides and energy storage application," *Small*, vol. 10, no. 2, pp. 300–307, 2014.

[6] Z. Yu and J. Thomas, "Energy storing electrical cables: integrating energy storage and electrical conduction," *Advanced Materials*, vol. 26, no. 25, pp. 4279–4285, 2014.

[7] P.-C. Chen, G. Shen, Y. Shi, H. Chen, and C. Zhou, "Preparation and characterization of flexible asymmetric supercapacitors based on transition-metal-oxide nanowire/single-walled carbon nanotube hybrid thin-film electrodes," *ACS Nano*, vol. 4, no. 8, pp. 4403–4411, 2010.

[8] A. Lewandowski, A. Olejniczak, M. Galinski, and I. Stepniak, "Performance of carbon-carbon supercapacitors based on organic, aqueous and ionic liquid electrolytes," *Journal of Power Sources*, vol. 195, no. 17, pp. 5814–5819, 2010.

[9] E. Frackowiak, "Carbon materials for supercapacitor application," *Physical Chemistry Chemical Physics*, vol. 9, no. 15, pp. 1774–1780, 2007.

[10] K.-W. Nam, C.-W. Lee, X.-Q. Yang, B. W. Cho, W.-S. Yoon, and K.-B. Kim, "Electrodeposited manganese oxides on three-dimensional carbon nanotube substrate: supercapacitive behaviour in aqueous and organic electrolytes," *Journal of Power Sources*, vol. 188, no. 1, pp. 323–331, 2009.

[11] J. Yan, Z. Fan, W. Sun et al., "Advanced asymmetric supercapacitors based on $\text{Ni}(\text{OH})_2$ /graphene and porous graphene electrodes with high energy density," *Advanced Functional Materials*, vol. 22, no. 12, pp. 2632–2641, 2012.

[12] X. Lu, M. Yu, G. Wang et al., "H-TiO₂@MnO₂//H-TiO₂@C core-shell nanowires for high performance and flexible asymmetric supercapacitors," *Advanced Materials*, vol. 25, no. 2, pp. 267–272, 2012.

[13] Z. Fan, J. Yan, T. Wei et al., "Asymmetric supercapacitors based on graphene/MnO₂ and activated carbon nanofiber electrodes with high power and energy density," *Advanced Functional Materials*, vol. 21, no. 12, pp. 2366–2375, 2011.

[14] W.-H. Jin, G.-T. Cao, and J.-Y. Sun, "Hybrid supercapacitor based on MnO₂ and columned FeOOH using Li₂SO₄ electrolyte solution," *Journal of Power Sources*, vol. 175, no. 1, pp. 686–691, 2008.

[15] T. Zhai, X. Lu, Y. Ling et al., "A new benchmark capacitance for supercapacitor anodes by mixed-valence sulfur-doped V₆O_{13-x}," *Advanced Materials*, vol. 26, no. 33, pp. 5869–5875, 2014.

[16] J. Xu, Q. Wang, X. Wang et al., "Flexible asymmetric supercapacitors based upon Co₉S₈ nanorod//Co₃O₄@RuO₂ nanosheet arrays on carbon cloth," *ACS Nano*, vol. 7, no. 6, pp. 5453–5462, 2013.

Research Article

Twist-Shaped CuO Nanowires as Anode Materials for Lithium Ion Batteries

Hongdong Liu,¹ Ye Lin,¹ Zhongli Hu,¹ Rong Hu,¹ Haibo Ruan,¹ and Lei Zhang²

¹Research Institute for New Materials Technology, Chongqing University of Arts and Sciences, Chongqing 402160, China

²College of Life Science, Chongqing Normal University, Chongqing 401331, China

Correspondence should be addressed to Lei Zhang; leizhang0215@126.com

Received 21 April 2016; Accepted 8 May 2016

Academic Editor: Gongming Wang

Copyright © 2016 Hongdong Liu et al. This is an open access article distributed under the Creative Commons Attribution License, which permits unrestricted use, distribution, and reproduction in any medium, provided the original work is properly cited.

Twist-shaped CuO nanowires were synthesized by two-step method consisting of solution reaction and then heat treatment. The as-synthesized samples were characterized by X-ray diffraction (XRD) and transmission electron microscopy (TEM). When evaluated as anode materials for lithium ion batteries, twist-shaped CuO nanowires showed a high initial discharge capacity of 983 mAh g^{-1} and maintained a reversible capacity of 320 mAh g^{-1} over 50 cycles at the current density of 100 mA g^{-1} . Thus, 1D twist-shaped CuO nanowires provide a new insight into the development of anode materials for next-generation high performance lithium ion batteries.

1. Introduction

Rechargeable lithium ion batteries have been considered as the most promising energy storage device for portable electronic devices and electrical vehicles due to their high electromotive force and high energy density [1–4]. Graphite is commonly used as the anode material for commercial lithium ion batteries owing to its natural abundance and low cost [5, 6]. However, graphite with low capacity of 372 mAh g^{-1} can not meet the increasing demand for high energy density [7, 8]. Therefore, it is urgent to explore a novel anode material with high theoretical capacity, such as silicon based materials [9], lithium alloy materials, and transition metal oxides [10].

As one of the transition metal oxides, CuO has attracted extensive attention because of its natural abundance, low cost, and ecofriendliness [11, 12], and it has a high theoretical capacity of 674 mAh g^{-1} , which is almost two times that of graphite. Same as the other transition metal oxides, it suffers from the large volume expansion and agglomeration during the discharge-charge process, which results in poor conductivity, rapid capacity fading, and poor cycle performance [13]. Some strategies have been made to resolve these issues significantly [14, 15]. It is reported that the CuO with various nanostructures can effectively alleviate these drawbacks, such as 0D nanoparticles [16], 1D nanowires [17],

2D nanoplates [18], and 3D nanoflowers [19]. Recently, 1D nanowires have shown great potential application in lithium ion batteries due to their large specific surface area and the porous nanostructures. It can provide short diffusion path lengths for lithium ion transport to improve the electrical conductivity and relieve the volume expansion [20, 21].

Herein, twist-shaped CuO nanowires were synthesized by two-step method consisting of solution reaction and then heat treatment for the $\text{Cu}(\text{OH})_2$ precursor at different temperatures (300°C , 400°C , and 500°C) in air. The as-prepared CuO nanowires exhibited enhanced lithium storage capacity and good cyclic performance as anode materials for lithium ion batteries.

2. Experimental

2.1. Preparation of Materials. All reagents were of analytical grade and directly used without further purification. In the typical synthesis process, 0.302 g of $\text{Cu}(\text{NO}_3)_2 \cdot 3\text{H}_2\text{O}$ and 5 mL of H_2O_2 were dissolved in 50 mL of deionized water under stirring constantly at room temperature for 15 min . Then, 50 mL of NaOH (0.15 M) aqueous solution was added to the above solution under mild mechanical stirring and kept for another 30 min . Next, the resulting samples were collected and washed and centrifuged with deionized water

and ethanol for several times and then dried at 60°C for a night in air. Finally, the CuO nanowires were obtained by annealing at 300°C, 400°C, and 500°C in air for 20 min and named as CuO-300°C, CuO-400°C, and CuO-500°C, respectively.

2.2. Structure and Morphology Characterization. X-ray powder diffraction patterns were collected with a TD-3500 X-ray diffractometer equipped with Cu/K α radiation ($\lambda = 0.154056$ nm); the collection angles were set to 10° to 80° with a scanning rate of 0.07° s⁻¹. The morphology and microstructure of the samples were investigated by scanning transmission electron microscopy (TEM-2100).

2.3. Electrochemical Measurements. Electrochemical experiments were carried out in 2032 coin-type cells. The working electrodes were prepared by mixing the active material (CuO nanowires), acetylene black, and polyvinylidene fluoride (PVDF) with a weight ratio of 80:10:10 in 1-methyl-2-pyrrolidinone (NMP) to form homogeneous slurry and the slurries were uniformly coated on the copper foil and finally dried at 100°C under vacuum for 12 hours; the total mass loading of the electrode is about 3 mg. The pure lithium sheet was as the counter and reference electrode. The electrolyte was 1 M LiPF₆ in ethylene carbonate (EC) and dimethyl carbonate (DMC) (1:1 by volume). All the cells were assembled in an argon-filled glovebox with the content of moisture and oxygen below 0.1 ppm.

Cyclic voltammetry (CV) and electrochemical impedance spectra (EIS) measurements were performed using CHI 760E electrochemistry workstation. The CV curves were obtained at a scan rate of 0.2 mV/s and the EIS plots were conducted in the frequency range from 100 kHz to 0.01 Hz. The galvanostatic charge-discharge tests were recorded on a Battery Testing System (Neware BTS-610) at the current density of 100 mA g⁻¹ in the voltage range of 0.01 to 3.0 V.

3. Results and Discussion

The schematic growth progress for the formation of twist-shaped CuO nanowires via a typical solution reaction and then heat treatment method is shown in Figure 1. When Cu(NO₃)₂·3H₂O and H₂O₂ solution were mixed under stirring constantly at room temperature, a blue solution was obtained. After 15 min, NaOH was added to the above solution, immediately resulting in a black turbid solution and forming numerous black Cu(OH)₂ precipitates. With increasing reaction time, the Cu(OH)₂ further aged and finally formed individual nanowire structures. Lastly, the twist-shaped CuO nanowires were obtained by annealing at temperature of 300–500°C.

The morphology and structure of twist-shaped CuO nanowires (500°C) were characterized by TEM. Figure 2(a) confirmed that the samples were a uniform nanowires' structure with a length of 0.75–2.7 μm. From the enlarged TEM image of samples in Figure 2(b), we could further see that the porous structure-like Chinese hemp flowers rope consisted of several twist-shaped nanowires with a width of

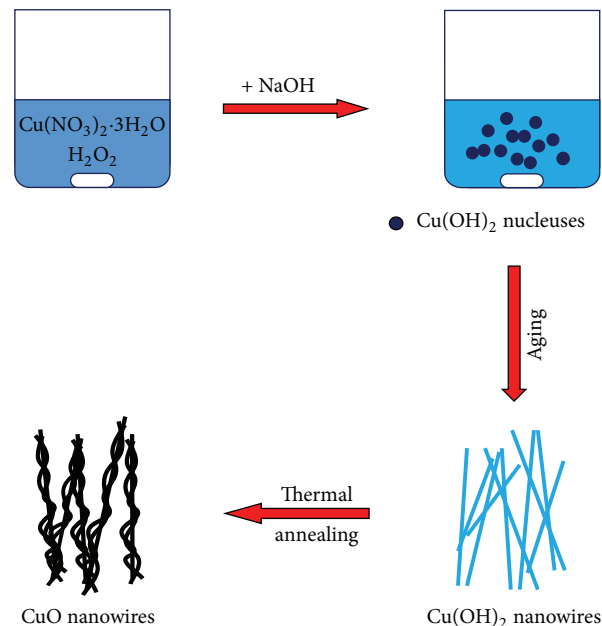


FIGURE 1: Schematic illustration of twist-shaped CuO nanowires.

about 20–75 nm and pores ranging from a few to a few tens of nanometers in diameter, which was beneficial to the intercalation of extra lithium and shortened the path of lithium ion transport during the charge-discharge process. The electron diffraction pattern of twist-shaped CuO nanowires (500°C) was shown in inset of Figure 2(b).

The crystal structures of the samples were further studied by powder X-ray diffraction in Figure 3. Apparently, the diffraction peaks of Cu(OH)₂ nanowires at different angles were like high pure crystal without other peaks compared with the standard card of Cu(OH)₂ (JCPDS 13-0420). Meanwhile, CuO-300°C, CuO-400°C, and CuO-500°C nanowires were also consistent with the standard card of CuO (JCPDS 48-1548), indicating that Cu(OH)₂ nanowires had transformed to monoclinic crystal CuO nanowires. Besides, the order of the full-width-at-half-maximum (FWHM) of XRD peaks for three CuO samples was 0.484° (CuO-500°C) < 0.593° (CuO-400°C) < 0.851° (CuO-300°C), which confirmed that the CuO-500°C nanowires had better pure crystallinity than others.

In order to investigate the performance of twist-shaped CuO nanowires, electrochemical characterization was conducted based on 2032 coin-type cells with pure lithium sheet as the counter electrode. The cyclic voltammetry curves of the CuO-500°C nanowires anode for the 1st, 2nd, and 3rd cycles in the potential range from 0 V to 3 V (versus Li⁺/Li) at a scan rate of 0.2 mV s⁻¹ were shown in Figure 4(a). In the first cathodic process, there were two peaks located at around 0.69 V and 0.93 V, which might be ascribed to the formation of a solid electrolyte interface (SEI) layer and the reduction of CuO to Cu, respectively [22]. In the first anodic process, two oxidation peaks at 0.81 V and 2.48 V were attributed to the oxidation of metallic Cu to Cu₂O and the oxidation of Cu₂O to CuO, respectively [23]. In subsequent cycles, the cathodic peaks shifted to 1.09 V and 0.61 V due

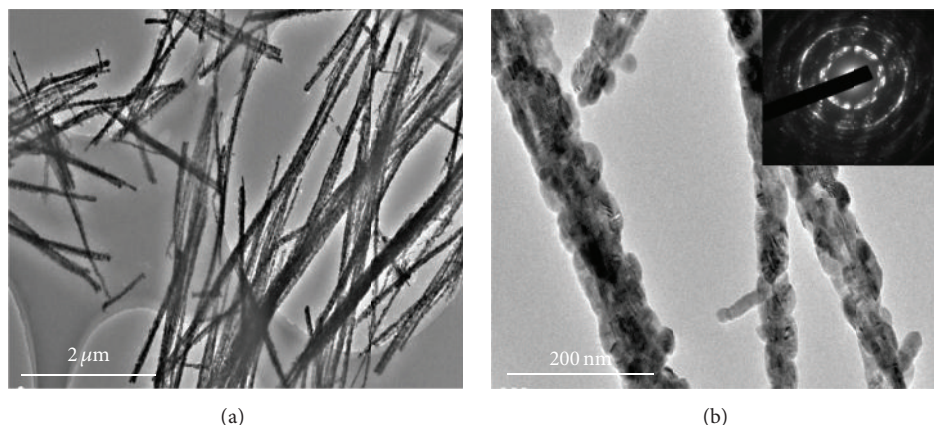


FIGURE 2: (a) Low-resolution TEM of twist-shaped CuO nanowires (500°C) and (b) high-resolution TEM of twist-shaped CuO nanowires (500°C). The inset presents SAED pattern of CuO nanowires (500°C).

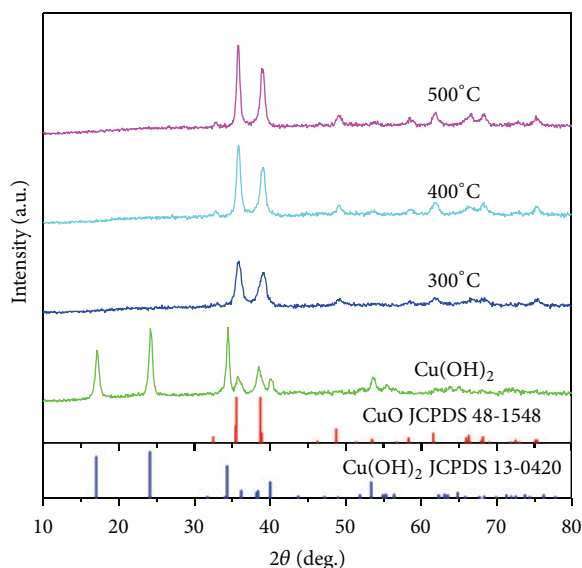


FIGURE 3: XRD patterns of the as-prepared Cu(OH)₂ nanowires and CuO-300°C, CuO-400°C, and CuO-500°C nanowires.

to the structure modification after the first cycle [18], and the anodic peaks overlapped very well, suggesting that the electrochemical reversibility of CuO tended to be more stable.

Figure 4(b) presented the galvanostatic discharge-charge profiles of CuO-500°C nanowires at the current density of 100 mA g⁻¹ in the voltage of 0~3.0 V. In the first discharge profile, two obvious sloping potential plateaus located at 1.6–1.15 V and 1.0–1.25 V were observed. The first long voltage plateau (1.6–1.15 V) implied that the lithium insertion to CuO was to form Cu and the second voltage plateau at 1.0–1.25 V was ascribed to the formation of a solid electrolyte interface (SEI) layer [16, 24]. In the following charge profile, an unobvious voltage plateau at around 2.41 V represented the oxidation of metallic Cu to CuO [23], which was in good agreement with the CV results. In the first cycle, the discharge capacity of CuO-500°C nanowires was about 983 mAh g⁻¹; however, the first charge capacity dramatically decreased to 496 mAh g⁻¹ corresponding to low coulombic efficiency

of 50%. The high capacity loss was believed to originate from the decomposition of electrolyte and the formation of solid electrolyte interface (SEI) layer on the electrode surface [25, 26]. At the second cycle, the discharge capacity was 495 mAh g⁻¹, with coulombic efficiency of 95.2%, and 482 mAh g⁻¹ and 96.5% at the third cycle, which indicated that the reversible performance increased.

The cycling performances of twist-shaped CuO nanowires of different temperature and their corresponding coulombic efficiencies at the current density of 100 mA g⁻¹ were shown in Figure 4(c). It can be seen that the CuO-500°C nanowires showed the highest capacity of 983 mAh g⁻¹ for the first cycle, the CuO-400°C presented lower capacity of 956 mAh g⁻¹, and the CuO-300°C presented the lowest capacity of 948 mAh g⁻¹. Although all samples had a higher capacity than the theoretical capacity of CuO (670 mAh g⁻¹) for the first cycle, they have a low coulombic efficiency, which is attributed to the formation of SEI layer on the electrode surface, large volume expansion, and electrode decomposition during the charge-discharge process [12, 27]. Even after 50 cycles, the discharge capacity of 320 mAh g⁻¹ of CuO-500°C was much higher than 203 mAh g⁻¹ of CuO-400°C and 133 mAh g⁻¹ of CuO-300°C. It is also better than that of spherical CuO nanoparticles reported by Zhang et al., 300 mAh g⁻¹ after 30 charge/discharge cycles [28]. Therefore, CuO-500°C nanowires exhibited the most excellent performance, which indicated that high temperature calcination was beneficial to the lithium storage. In addition, all samples possessed a high coulombic efficiency of 98% except the first several cycles.

In order to verify the remarkable cycle performance of CuO nanowires electrodes, electrochemical impedance spectrum (EIS) was performed on the cell. Electrochemical impedance spectrum (EIS), in Figure 4(d), consisted of a small semicircle at the high-medium frequency region and a long line at the low-medium frequency region. In the high-medium frequency, semicircle represented the electric contact and charge-transfer resistance and, in the low-medium frequency, the slope of line associated with lithium ion diffusion activity. Obviously, we could observe that the diameter

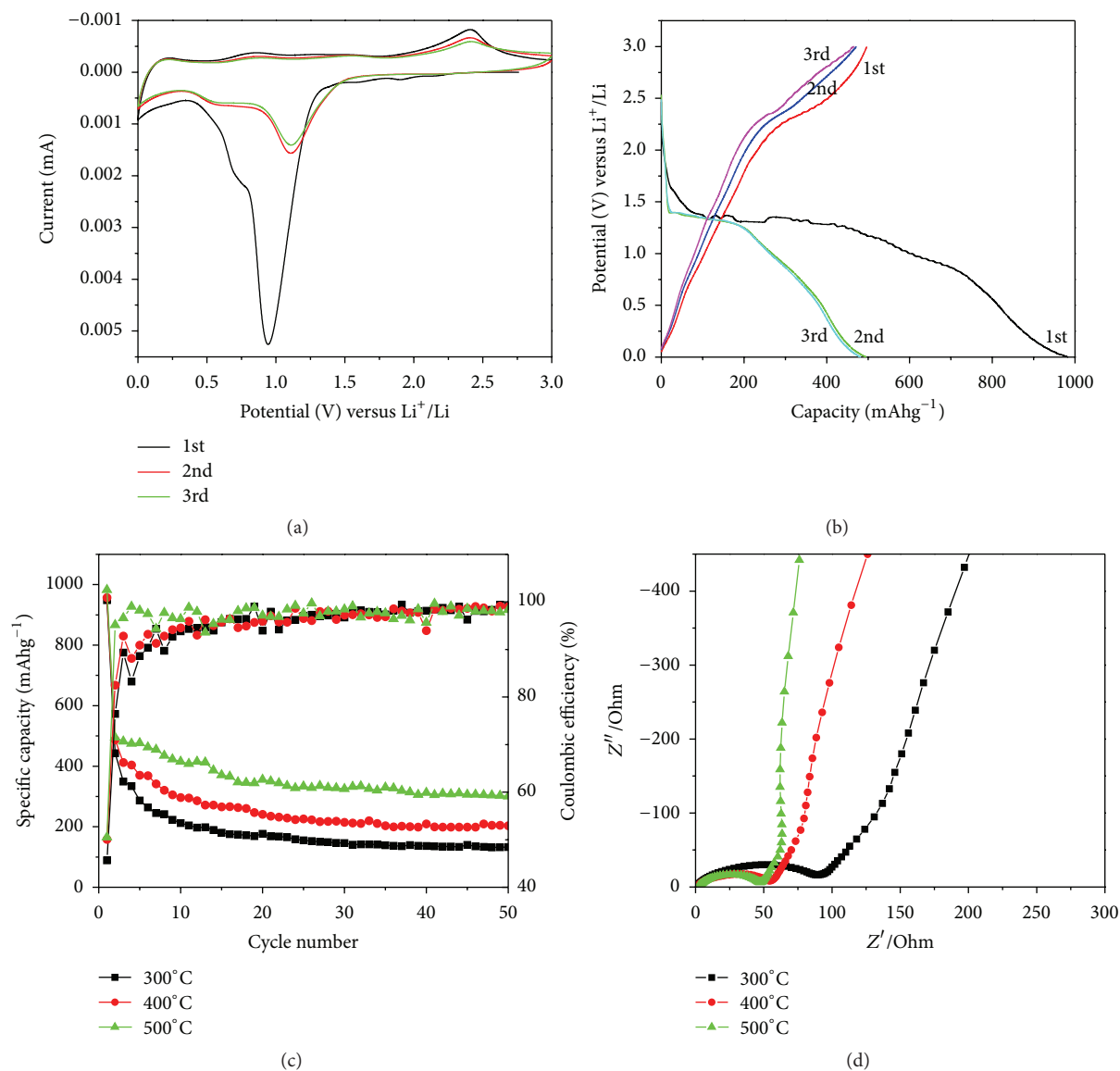


FIGURE 4: (a) Cyclic voltammograms of CuO-500°C nanowires in the 1st, 2nd, and 3rd cycles. (b) Galvanostatic discharge-charge profiles in the 1st, 2nd, and 3rd cycles of CuO-500°C nanowires at the current density of 100 mA g^{-1} . (c) Cycling performances of CuO-300°C, CuO-400°C, and CuO-500°C at the current density of 100 mA g^{-1} . (d) Electrochemical impedance spectra plots of CuO nanowires electrodes over the frequency range of 100 kHz and 0.01 Hz.

of the semicircle of CuO-500°C was smaller than that of CuO-400°C and CuO-300°C, suggesting that CuO-500°C had the lowest electric contact and charge-transfer resistance. What was more, the slope of line of CuO-500°C was bigger compared to others, which also verified the front result. Because of better crystallinity at 500°C, CuO at 500°C showed more superior electrochemical performance to the other temperatures.

4. Conclusion

In this work, twist-shaped CuO nanowires were successfully synthesized by two-step method consisting of solution reaction and then heat treatment for the $\text{Cu}(\text{OH})_2$ precursor at different temperature in air. This method is simple, rapid,

green, and of low cost. When evaluated as anode materials for lithium ion batteries, CuO-500°C nanowires showed a great electrochemical performance, including high discharge capacity and high capacity retention, delivered a high initial discharge capacity of 983 mAh g^{-1} in the first cycle, and maintained a reversible capacity of 320 mAh g^{-1} over 50 cycles at a current density of 100 mA g^{-1} . Thus, 1D twist-shaped CuO nanowires provided a new insight into the development of anode materials for next-generation high performance lithium ion batteries.

Competing Interests

The authors declare that they have no competing interests.

Acknowledgments

This work was financially supported by Basic and Frontier Research Program of Chongqing Municipality (cstc2015jcyjA90020 and cstc2014jcyjA10063), Scientific and Technological Research Program of Chongqing Municipal Education Commission (KJ1501101, KJ1500323, and KJ1501116), Introduction of Talent Project of Chongqing University of Arts and Sciences (R2013CJ06), China Postdoctoral Science Foundation (2015M582499), Postdoctoral Special Foundation of Chongqing (Xm2015064), Project of Chongqing Normal University (14XYY025 and 14XLB004), and National Natural Science Foundation of China (51502030).

References

- [1] W. Wei, S. Yang, H. Zhou, I. Lieberwirth, X. Feng, and K. Müllen, "3D graphene foams cross-linked with pre-encapsulated Fe_3O_4 nanospheres for enhanced lithium storage," *Advanced Materials*, vol. 25, no. 21, pp. 2909–2914, 2013.
- [2] C. Marino, A. Debenedetti, B. Fraisse, F. Favier, and L. Monconduit, "Activated-phosphorus as new electrode material for Li-ion batteries," *Electrochemistry Communications*, vol. 13, no. 4, pp. 346–349, 2011.
- [3] Z. Cao, Y. Ding, J. Zhang et al., "Submicron peanut-like MnCO_3 as an anode material for lithium ion batteries," *RSC Advances*, vol. 5, no. 69, pp. 56299–56303, 2015.
- [4] J.-Y. Liao, D. Higgins, G. Lui, V. Chabot, X. Xiao, and Z. Chen, "Multifunctional TiO_2 -C/ MnO_2 core-double-shell nanowire arrays as high-performance 3D electrodes for lithium ion batteries," *Nano Letters*, vol. 13, no. 11, pp. 5467–5473, 2013.
- [5] A. Bhaskar, M. Deepa, T. N. Rao, and U. V. Varadaraju, "Enhanced nanoscale conduction capability of a MoO_2 /Graphene composite for high performance anodes in lithium ion batteries," *Journal of Power Sources*, vol. 216, pp. 169–178, 2012.
- [6] X. Dong, L. Li, C. Zhao, H.-K. Liu, and Z. Guo, "Controllable synthesis of RGO/ Fe_xO_y nanocomposites as high-performance anode materials for lithium ion batteries," *Journal of Materials Chemistry A*, vol. 2, no. 25, pp. 9844–9850, 2014.
- [7] Z. Bai, N. Fan, C. Sun et al., "Facile synthesis of loaf-like ZnMn_2O_4 nanorods and their excellent performance in Li-ion batteries," *Nanoscale*, vol. 5, no. 6, pp. 2442–2447, 2013.
- [8] W. Kang, Y. Tang, W. Li et al., "Porous CuCo_2O_4 nanocubes wrapped by reduced graphene oxide as high-performance lithium-ion battery anodes," *Nanoscale*, vol. 6, no. 12, pp. 6551–6556, 2014.
- [9] S. Jing, H. Jiang, Y. Hu, and C. Li, "Directly grown Si nanowire arrays on Cu foam with a coral-like surface for lithium-ion batteries," *Nanoscale*, vol. 6, no. 23, pp. 14441–14445, 2014.
- [10] P. Lv, H. Zhao, Z. Zeng, J. Wang, T. Zhang, and X. Li, "Facile preparation and electrochemical properties of carbon coated Fe_3O_4 as anode material for lithium-ion batteries," *Journal of Power Sources*, vol. 259, pp. 92–97, 2014.
- [11] J. Pal, C. Mondal, A. K. Sasmal, M. Ganguly, Y. Negishi, and T. Pal, "Account of nitroarene reduction with size- and facet-controlled CuO - MnO_2 nanocomposites," *ACS Applied Materials & Interfaces*, vol. 6, no. 12, pp. 9173–9184, 2014.
- [12] Q. Wang, J. Zhao, W. Shan, X. Xia, L. Xing, and X. Xue, "CuO nanorods/graphene nanocomposites for high-performance lithium-ion battery anodes," *Journal of Alloys and Compounds*, vol. 590, pp. 424–427, 2014.
- [13] S. Yuan, X.-L. Huang, D.-L. Ma, H.-G. Wang, F.-Z. Meng, and X.-B. Zhang, "Engraving copper foil to give large-scale binder-free porous CuO arrays for a high-performance sodium-ion battery anode," *Advanced Materials*, vol. 26, no. 14, pp. 2273–2279, 2014.
- [14] Y. Xu, R. Yi, B. Yuan et al., "High capacity MoO_2 /graphite oxide composite anode for lithium-ion batteries," *Journal of Physical Chemistry Letters*, vol. 3, no. 3, pp. 309–314, 2012.
- [15] K. Zhang, W. Zhao, J.-T. Lee, G. Jang, X. Shi, and J. H. Park, "A magnetic field assisted self-assembly strategy towards strongly coupled Fe_3O_4 nanocrystal/rGO paper for high-performance lithium ion batteries," *Journal of Materials Chemistry A*, vol. 2, no. 25, pp. 9636–9644, 2014.
- [16] S. He, J. Li, J. Wang, G. Yang, and Z. Qiao, "Facile synthesis and lithium storage performance of hollow CuO microspheres," *Materials Letters*, vol. 129, pp. 5–7, 2014.
- [17] L. Wang, K. Zhang, Z. Hu, W. Duan, F. Cheng, and J. Chen, "Porous CuO nanowires as the anode of rechargeable Na-ion batteries," *Nano Research*, vol. 7, no. 2, pp. 199–208, 2014.
- [18] Y. Liu, Y. Qiao, W. Zhang et al., "Facile fabrication of CuO nanosheets on Cu substrate as anode materials for electrochemical energy storage," *Journal of Alloys and Compounds*, vol. 586, pp. 208–215, 2014.
- [19] Z. Hu and H. Liu, "Three-dimensional CuO microflowers as anode materials for Li-ion batteries," *Ceramics International*, vol. 41, no. 6, pp. 8257–8260, 2015.
- [20] C. Wu, X. Li, W. Li et al., " Fe_2O_3 nanorods/carbon nanofibers composite: preparation and performance as anode of high rate lithium ion battery," *Journal of Power Sources*, vol. 251, pp. 85–91, 2014.
- [21] Q. Zhou, Z. Zhao, Z. Wang et al., "Low temperature plasma synthesis of mesoporous Fe_3O_4 nanorods grafted on reduced graphene oxide for high performance lithium storage," *Nanoscale*, vol. 6, no. 4, pp. 2286–2291, 2014.
- [22] J. Wang, Q. Zhang, X. Li et al., "Three-dimensional hierarchical Co_3O_4 / CuO nanowire heterostructure arrays on nickel foam for high-performance lithium ion batteries," *Nano Energy*, vol. 6, pp. 19–26, 2014.
- [23] C. Wang, Q. Li, F. Wang et al., "Morphology-dependent performance of CuO anodes via facile and controllable synthesis for lithium-ion batteries," *ACS Applied Materials and Interfaces*, vol. 6, no. 2, pp. 1243–1250, 2014.
- [24] A. Li, H. Song, W. Wan, J. Zhou, and X. Chen, "Copper oxide nanowire arrays synthesized by in-situ thermal oxidation as an anode material for lithium-ion batteries," *Electrochimica Acta*, vol. 132, pp. 42–48, 2014.
- [25] J. Guo, L. Ma, X. Zhang, Y. Zhang, and L. Tang, "Mesoporous CuO xerogels constructed by nanorods for high-performance lithium storage," *Materials Letters*, vol. 118, pp. 142–145, 2014.
- [26] L. Feng, Z. Xuan, Y. Bai et al., "Preparation of octahedral CuO micro/nanocrystals and electrochemical performance as anode for lithium-ion battery," *Journal of Alloys and Compounds*, vol. 600, pp. 162–167, 2014.
- [27] C. Wang, J. Xu, R. Ma, and M.-F. Yuen, "Facile synthesis of CuO nanoneedle electrodes for high-performance lithium-ion batteries," *Materials Chemistry and Physics*, vol. 148, no. 1–2, pp. 411–415, 2014.
- [28] X. Zhang, G. Wang, X. Liu, and H. Wu, "Synthesis and electrochemical properties of CuO nanobelts," *Materials Chemistry and Physics*, vol. 112, no. 3, pp. 726–729, 2008.

Research Article

Manganese Oxide on Carbon Fabric for Flexible Supercapacitors

Jianfeng Zhang,¹ Mujun Chen,¹ Yunwang Ge,² and Qi Liu²

¹College of Information Engineering, Henan Vocational College of Agriculture, Zhengzhou 451450, China

²College of Electrical Engineering and Automation, Luoyang Institute of Science and Technology, Luoyang 471023, China

Correspondence should be addressed to Qi Liu; liuqi8349@163.com

Received 5 May 2016; Accepted 26 May 2016

Academic Editor: Yang Song

Copyright © 2016 Jianfeng Zhang et al. This is an open access article distributed under the Creative Commons Attribution License, which permits unrestricted use, distribution, and reproduction in any medium, provided the original work is properly cited.

We report the fabrication of uniform large-area manganese oxide (MnO_2) nanosheets on carbon fabric which oxidized using O_2 plasma treatment (MnO_2/O_2 -carbon fabric) via electrodeposition process and their implementation as supercapacitor electrodes. Electrochemical measurements demonstrated that MnO_2/O_2 -carbon fabric exhibited capacitance as high as 275 F/g at a scan rate of 5 mV/s; in addition, it showed an excellent cycling performance (less than 20% capacitance loss after 10,000 cycles). All the results suggest that MnO_2/O_2 -carbon fabric is a promising electrode material which has great potential for application on flexible supercapacitors.

1. Introduction

With the rapid development of economy, the global energy consumption has been increasing for decades. As a result, the traditional fossil energy faces serious shortages. Green renewable energy such as solar cells and wind power generation set is desired. However, most of the new energy sources are intermittent and unsustainable, which hinder their application greatly [1, 2]. The energy supply gap deriving from the discontinuous characteristics of the renewable sources can be filled by coupling them with energy storage devices, such as supercapacitors (SCs) and batteries, which are able to store energy and deliver it to power the electronics [3–5].

SCs have drawn great attention in addressing the emerging energy demands due to the advantages of high power density, fast charge/discharge rates, and long cycle life [6–8]. Generally, SCs could be categorized into two types according to the charge storage mechanisms: electrochemical double layer capacitors (EDLCs) [9, 10] and pseudocapacitors (PSCs) [11–13]. EDLCs attract charges on the electrode-electrolyte interface of electrode materials electrostatically; meanwhile PSCs store energy via fast redox reaction on/near electrode surface [5, 14, 15]. Each of the two types of SCs has advantages and disadvantages, respectively. EDLCs use carbon materials such as carbon nanotubes (CNTs), graphene, carbon

nanofibers (CFs), and carbon onion as electrode materials, while PSCs employ transition metal oxides or conducting polymers such as manganese oxide (MnO_2), molybdenum trioxide (MoO_3), and polyaniline as electrode materials. Carbon materials usually hold higher physical and chemical stability, better electrical conductivity, and higher specific surface than those materials for PSCs, resulting in higher rate capability and longer durability than the latter. However, the theoretical capacitance of carbon materials is much lower than that for transition metal oxides, leading to the fact that most specific capacitance of carbon-based EDLCs are less than 150 F/g [3, 16–18]. On the contrary, PSCs exhibit higher capacitance and energy density through Faradic reaction, but suffered by the poor electrical conductivity [12, 19]. In this regard, if we can combine both the advantages of the two types of SCs and solve the shortcomings, then the SCs with enhanced electrochemical properties could be expected.

MnO_2 is one of the most attractive pseudocapacitive materials for the superior theoretical capacitance (1370 F/g), low cost, and abundance. Nevertheless, it suffered from the poor electric conductivity (10^{-5} – 10^{-6} S/cm), leading to the fact that the practice capacitance is much lower than the theoretical value [20, 21]. Growth of pseudocapacitive materials on well conductive carbon substrates not only can facilitate the diffusion of electrolyte ions but also can improve the transport of electrons, thus enhancing the electrochemical

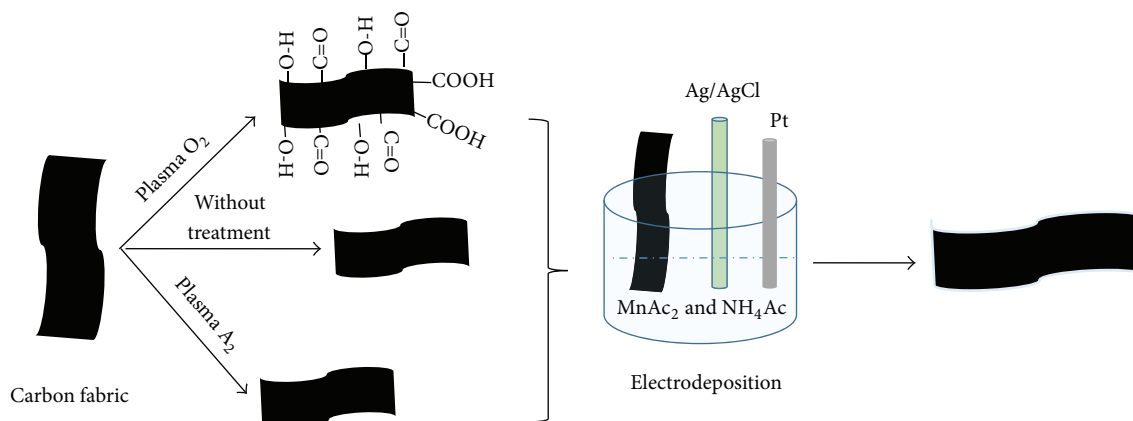


FIGURE 1: Schematic of the fabrication procedure for MnO_2 -carbon composites.

properties [22, 23]. Furthermore, the hybrid structures may broaden their applications in energy storage device [24].

Herein, different surface treatments were employed to carbon fabric for assessing the influence of different treatments on the surface chemical states. We choose carbon fabric as substrates here for its low cost, good electrical conductivity, excellent chemical stability, and the flexible nature. Characterizations showed that the oxidic carbon fabric substrate is more suitable for electrodeposition of MnO_2 , for the reason of more oxygen containing functional groups which can act as nucleation points of MnO_2 . As a result, it exhibits a high specific capacitance (275 F/g) at a current density of 5 mV/s. In addition, the oxidic carbon fabric- MnO_2 showed excellent long-term cycle stability.

2. Experimental

2.1. Synthesis of MnO_2 /Carbon Fabric. The carbon fabric was oxidized or reduced using plasma technology. Firstly, carbon fabric was cut into the same size ($0.9 \times 1.8 \text{ cm}^2$). Then it was cleaned ultrasonically for 15 min by acetone, ethanol, and deionized water, respectively. After drying at 70°C , the carbon fabric was placed in plasma sample chamber for oxidation or reduction treatments. The treated carbon fabric was ready for next experiments.

A template-free electrodeposition method was introduced to fabricate MnO_2 /carbon fabric in a three-electrode cell. Carbon fabric, a graphite rod, and a saturated Ag/AgCl electrode were used as working electrode, counter electrode, and reference electrode, respectively. The solution containing 0.01 M manganese acetate (MnAc_2) and 0.02 M ammonium acetate (NH_4Ac) was used as electrolyte. The constant current and deposition time are 0.1 mA/cm^2 and 30 min, respectively.

2.2. Fabrication of SCs Electrodes. One piece of MnO_2 /carbon fabric was used as working electrode. The saturated Ag/AgCl electrode, a piece of pure Pt foil, and 1 M sodium sulfate (Na_2SO_4) aqueous solution were employed as reference electrode, counter electrode, and electrolyte, respectively.

2.3. Characterization. The morphology of MnO_2 /carbon fabric was analyzed using scanning electron microscopy (SEM, JSM-7100F). The transmission electron microscopy (TEM) and high-resolution transmission electron microscopy (HR-TEM) were performed on a JEOL-2010 HR transmission electron microscope to further investigate the internal structures and lattice fringes. The crystal structure of MnO_2 /carbon fabric was characterized by X-ray diffraction using the Cu K_α radiation ($\lambda = 1.5418 \text{ \AA}$) (XRD, D8-Advanced Bruker-AXS).

The electrochemical workstation (Chenhua, CHI 660D) was used to perform cyclic voltammetry (CV) and chronopotentiometry measurements. Autolab (PGSTAT302N) was used to measure the electrochemical impedance spectroscopy (EIS) with potential amplitude of 10 mV under the frequency ranging from 10 kHz to 100 mHz.

3. Results and Discussion

The fabrication procedure for the MnO_2 -carbon fabric composites is illustrated in Figure 1. Firstly, the carbon fabric cut in $0.9 \times 1.8 \text{ cm}^2$ is washed by deionized water, acetone, and ethanol, respectively. After drying, the carbon fabric was reduced or oxidized by plasma to add redox active functional groups on carbon fabric. Finally, the efficient electrodeposition method was adopted to prepare MnO_2 -carbon fabric composites.

The morphology of the original carbon fabric and as-prepared MnO_2 /carbon fabric samples was characterized by SEM, as shown in Figure 2. Figure 2(a) clearly shows that there is no other substance on the carbon fiber surface except very small amount of impurities. After electrodeposition, all the carbon fibers were covered by a multitude of MnO_2 on their surface (Figures 2(b)–2(d)). However, from Figures 2(b) and 2(c), it can be observed clearly that both the electrodeposition samples based on the pristine carbon fabric (MnO_2 /carbon fabric) and the carbon fabric reduced under Ar atmosphere (MnO_2 /Ar-carbon fabric) covered by many flower-like MnO_2 on the surface which exhibit uneven surface characteristics, suggesting lower pseudocapacitive electrochemical performance. Meanwhile, there is lots of sheet

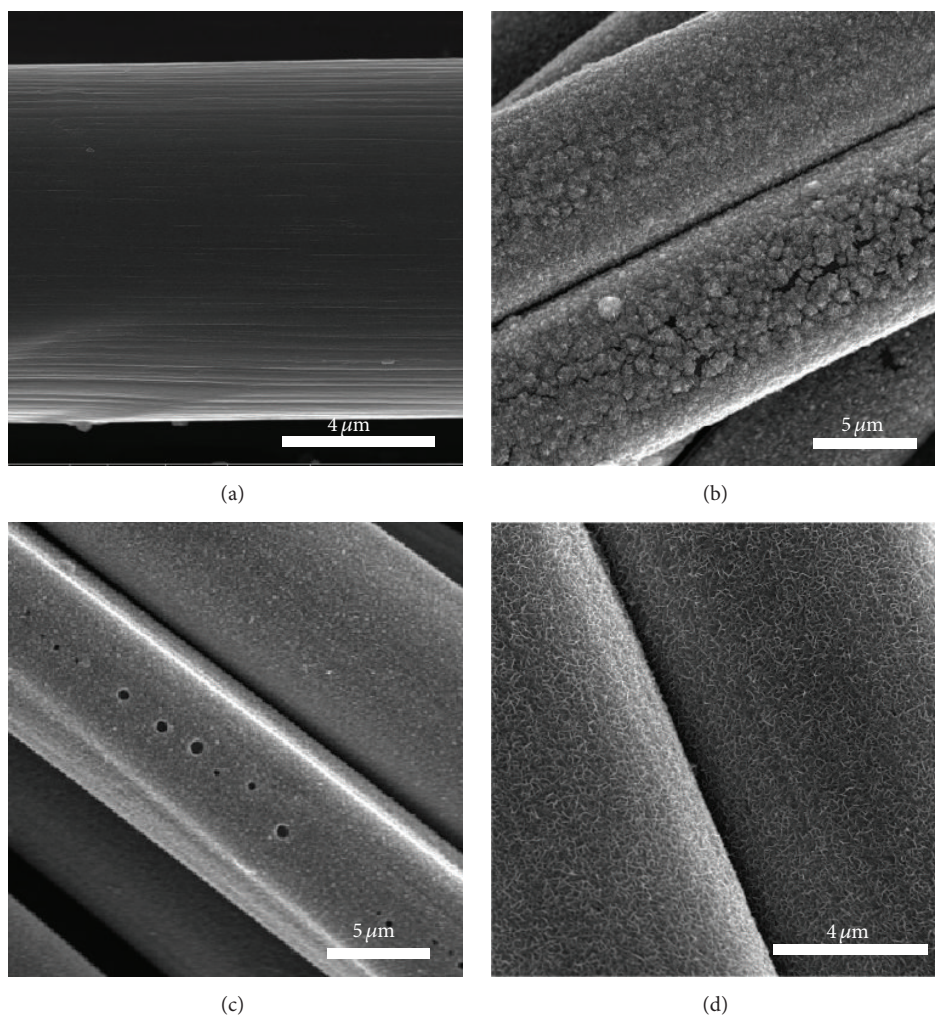


FIGURE 2: The SEM images of (a) the rare carbon fabric, (b) $\text{MnO}_2/\text{carbon}$ fabric, (c) $\text{MnO}_2/\text{Ar}_2\text{-carbon}$ fabric, and (d) $\text{MnO}_2/\text{O}_2\text{-carbon}$ fabric.

MnO_2 covering densely the carbon fabric fiber surface which oxidized under O_2 atmosphere ($\text{MnO}_2/\text{O}_2\text{-carbon}$ fabric). The uniform surface morphology implies that it may have good electrochemical performance. Hence, we will further investigate the internal structure and electrochemical properties of $\text{MnO}_2/\text{O}_2\text{-carbon}$ fabric.

TEM was introduced to further investigate the morphology of $\text{MnO}_2/\text{O}_2\text{-carbon}$ fabric, as shown in Figure 3. According to the low resolution TEM image (Figure 3(a)), the electrodeposited MnO_2 is a sheet shape with a nanoscale thickness. HRTEM image (Figure 3(b)) shows the interplanar spacings for the two perpendicular directions to be ~ 0.48 nm. This value corresponds to d_{101} of the tetragonal MnO_2 phase (JCPDS reference card number 18-0802).

XRD pattern was collected from the electrodeposited products for investigating the crystal phase, as shown in Figure 4. From the spectrum, there are six peaks located at $2\theta = 11.4^\circ, 21.4^\circ, 36.5^\circ, 37.7^\circ, 41.3^\circ, 54.9^\circ,$ and 65.7° . Among them, the broad peak located at 21.4° not only corresponds to the amorphous carbon but also can be assigned to the reflection

of (101) of tetragonal MnO_2 . Meanwhile, the other five peaks can be well assigned to the tetragonal MnO_2 (JCPDS reference card number 18-0802), which is consistent well with the TEM observations. Hence, the products synthesized by electrodeposition procedure are tetragonal MnO_2 .

To study the electrochemical performances of $\text{MnO}_2/\text{O}_2\text{-carbon}$ fabric, cyclic voltammetry (CV) and galvanostatic charge-discharge (GCD) were conducted using a three-electrode configuration with Ag/AgCl as reference electrode and 1 M Na_2SO_4 as electrolyte. The typical CV curves of $\text{MnO}_2/\text{O}_2\text{-carbon}$ fabric are displayed in Figure 5(a) with scan rates from 5 mV/s to 100 mV/s. From the curves, even the scan rate has been increased to 100 mV/s; the CV curves retain a symmetrical rectangular shape, which demonstrate that the $\text{MnO}_2/\text{O}_2\text{-carbon}$ fabric not only holds rapid capacitive response but also has good electronic conductivity. In addition, the GCD curves of $\text{MnO}_2/\text{O}_2\text{-carbon}$ fabric collected at various current densities (Figure 5(b)) remain of semisymmetric shape revealing reversible ion adsorption/reaction on the surface and good Coulombic efficiency. Moreover, the

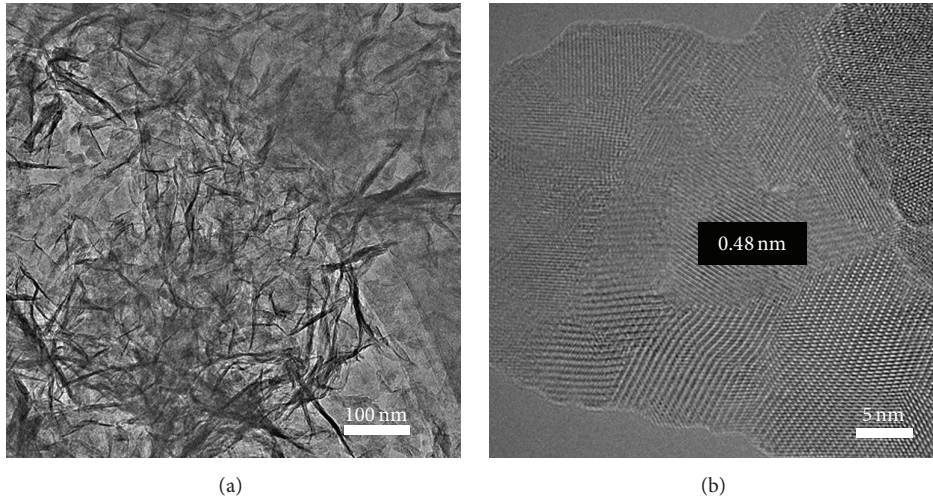


FIGURE 3: (a) TEM image and (b) HRTEM image of MnO₂/O₂-carbon fabric.

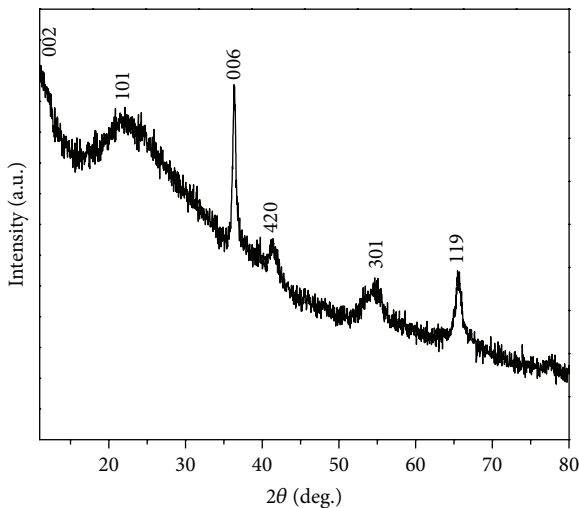


FIGURE 4: The XRD pattern of the electrodeposited products.

IR drop derived from the GCD curves of MnO₂/O₂-carbon fabric is as low as 0.05 V at 2 A/g, suggesting the MnO₂/O₂-carbon fabric has good electrical conductivity. Combined with the excellent electrical conductivity of the carbon fabric and high theory capacitance value of manganese MnO₂, enhanced properties are expected.

The specific capacitance derived from the discharge curves measured at different current densities could be calculated according to the following equation [1]:

$$C_s = \frac{Q}{\Delta U \times m}, \quad (1)$$

where C_s is the mass specific capacitance of the MnO₂/O₂-carbon fabric, Q is the average electric quantity, ΔU is the working voltage window of the active material, and m is the mass of the active material.

The specific capacitance of the MnO₂/O₂-carbon fabric calculated from their CV curves with different scan rates was

summarized in Figure 5(c). From the specific capacitance change curve, the specific capacitance value decreases along with the increase of the scan rate. The highest specific capacitance for MnO₂/O₂-carbon fabric can achieve 275 F/g at the scan rate of 5 mV/s. This value is higher than those recently reported for other MnO₂ electrodes [25–27]. The specific capacitance of MnO₂/O₂-carbon fabric still remains more than 45% (120 F/g) comparable with that obtained at 5 mV/s when the scan rate increases to 200 mV/s. It is important to note that the specific capacitance contribution of the carbon fabric is rather small [28, 29]. Thus, the MnO₂/O₂-carbon fabric has high rate capability which provides a benefit for the potential applications. The high rate capability could be attributed to the unique free-standing composite structure including good-electrical-conductivity carbon fibers and disordered nanosheets which not only makes electron transportation and ion diffusion convenient, but also facilitates the reaction of active species, so that a good rate capability was obtained.

Beside high specific capacitance, good cycling performance is also one of the most important characteristics for high-performance supercapacitors [24]. In present work, GCD cycling at a current density of 5 A/g was employed to evaluate the long-term stability of the MnO₂/O₂-carbon fabric electrode. From Figure 5(d), it is observed clearly that the specific capacitance for MnO₂/O₂-carbon fabric remains more than 70% of the initial capacitance over the first 5000 cycles. Meanwhile, the capacitance even slightly increases to about 80% of the initial capacitance after 10,000 cycles. The specific capacitance increase of the MnO₂/O₂-carbon fabric could be assigned to the following reasons: after the beginning circulations, the intercalation and deintercalation of the active species had been reacted completely, leading to the increase of active points; hence the specific capacitance was enhanced. This outstanding long-term stability performance could be attributed to the good contact between MnO₂ nanosheets and carbon fibers. Furthermore, this cycling performance is higher than those recently reported results

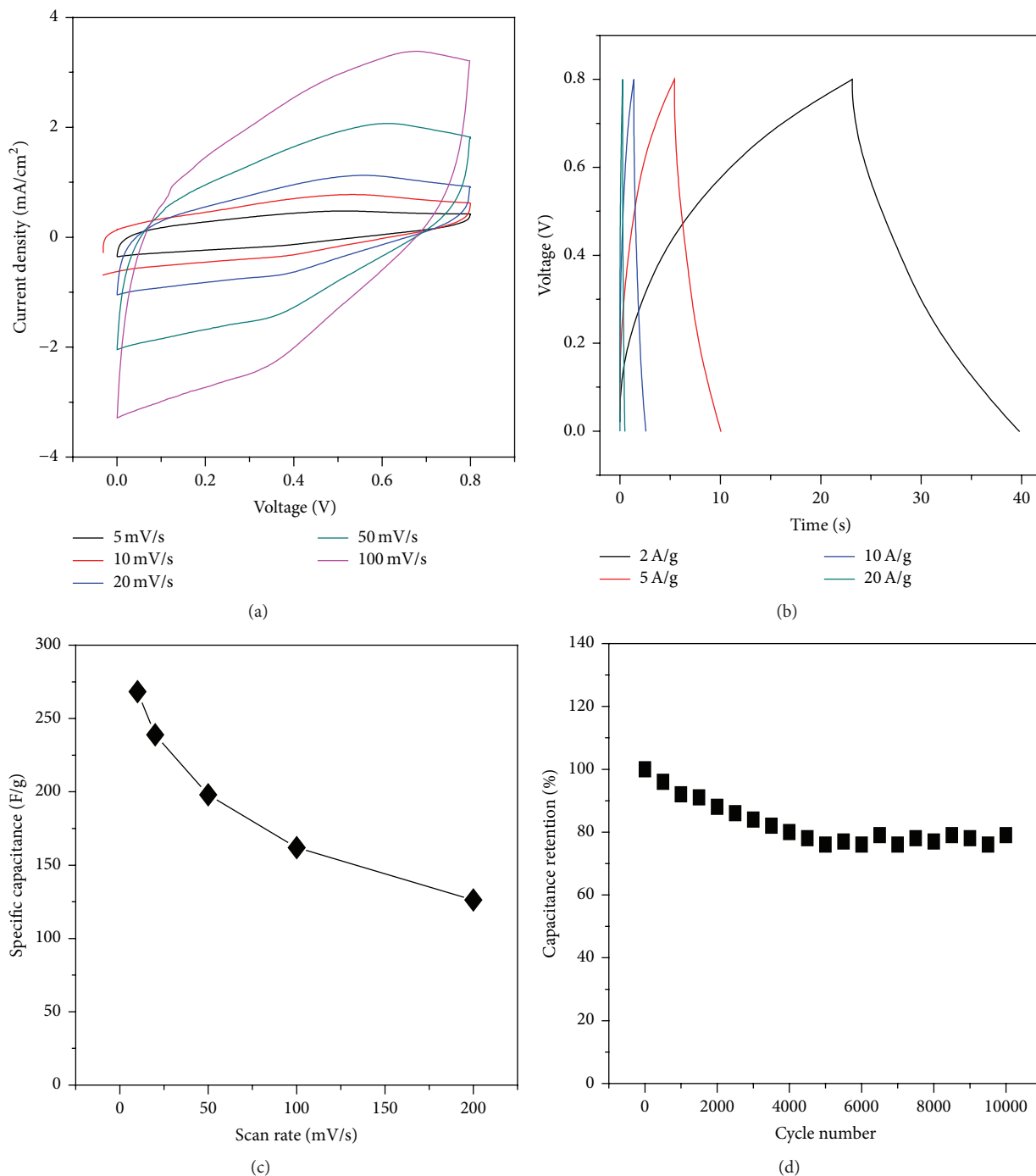


FIGURE 5: (a) Cyclic voltammogram curves, (b) galvanostatic charge-discharge curves, (c) specific capacitance, and (d) cyclic performance of MnO₂/O₂-carbon fabric, respectively.

for MnO₂ nanotube arrays [30], MnO₂ nanowires [31], and hierarchical tubular MnO₂ structures [32].

4. Conclusions

In summary, uniform large-area MnO₂ nanosheets were successfully fabricated on flexible carbon fabric through a simple

electrodeposition method. The as-electrodeposited MnO₂/O₂-carbon fabric was implemented as supercapacitor electrodes and shows outstanding electrochemical performance such as high specific capacitance and good cyclic stability. These results suggest that MnO₂/O₂-carbon fabric is a promising electrode material which has great potential for application in flexible supercapacitors.

Competing Interests

The authors declare that they have no competing interests.

Acknowledgments

This work is supported by the Key Scientific Research Project of Higher Education of Henan Province (15B510012) and the Starting Fund for High-Scientific Study of Genius of Luoyang Institute of Science and Technology (2014BZ09).

References

- [1] J. R. Miller and P. Simon, "Electrochemical capacitors for energy management," *Science*, vol. 321, no. 5889, pp. 651–652, 2008.
- [2] M. F. El-Kady and R. B. Kaner, "Scalable fabrication of high-power graphene micro-supercapacitors for flexible and on-chip energy storage," *Nature Communications*, vol. 4, article 1475, 2013.
- [3] P. Simon and Y. Gogotsi, "Materials for electrochemical capacitors," *Nature Materials*, vol. 7, no. 11, pp. 845–854, 2008.
- [4] C. D. Lokhande, D. P. Dubal, and O.-S. Joo, "Metal oxide thin film based supercapacitors," *Current Applied Physics*, vol. 11, no. 3, pp. 255–270, 2011.
- [5] W. F. Wei, X. W. Cui, W. X. Chen, and D. G. Ivey, "Manganese oxide-based materials as electrochemical supercapacitor electrodes," *Chemical Society Reviews*, vol. 40, no. 3, pp. 1697–1721, 2011.
- [6] L. Hu and Y. Cui, "Energy and environmental nanotechnology in conductive paper and textiles," *Energy and Environmental Science*, vol. 5, no. 4, pp. 6423–6435, 2012.
- [7] C. Yuan, H. B. Wu, Y. Xie, and X. W. Lou, "Mixed transition-metal oxides: design, synthesis, and energy-related applications," *Angewandte Chemie—International Edition*, vol. 53, no. 6, pp. 1488–1504, 2014.
- [8] X. Li and B. Wei, "Facile synthesis and super capacitive behavior of SWNT/MnO₂ hybrid films," *Nano Energy*, vol. 1, no. 3, pp. 479–487, 2012.
- [9] Y. Qiu, X. Zhang, and S. Yang, "High performance supercapacitors based on highly conductive nitrogen-doped graphene sheets," *Physical Chemistry Chemical Physics*, vol. 13, no. 27, pp. 12554–12558, 2011.
- [10] D. Sun, X. Yan, J. Lang, and Q. Xue, "High performance supercapacitor electrode based on graphene paper via flame-induced reduction of graphene oxide paper," *Journal of Power Sources*, vol. 222, pp. 52–58, 2013.
- [11] L. Chen, L.-J. Sun, F. Luan, Y. Liang, Y. Li, and X.-X. Liu, "Synthesis and pseudocapacitive studies of composite films of polyaniline and manganese oxide nanoparticles," *Journal of Power Sources*, vol. 195, no. 11, pp. 3742–3747, 2010.
- [12] S. L. Candelaria, B. B. Garcia, D. Liu, and G. Cao, "Nitrogen modification of highly porous carbon for improved supercapacitor performance," *Journal of Materials Chemistry*, vol. 22, no. 19, pp. 9884–9889, 2012.
- [13] D. Yuan, J. Chen, J. Zeng, and S. Tan, "Preparation of monodisperse carbon nanospheres for electrochemical capacitors," *Electrochemistry Communications*, vol. 10, no. 7, pp. 1067–1070, 2008.
- [14] P. Simon and Y. Gogotsi, "Capacitive energy storage in nanostructured carbon-electrolyte systems," *Accounts of Chemical Research*, vol. 46, no. 5, pp. 1094–1103, 2013.
- [15] G. Zhao, N. Zhang, and K. Sun, "Porous MoO₃ films with ultra-short relaxation time used for supercapacitors," *Materials Research Bulletin*, vol. 48, no. 3, pp. 1328–1332, 2013.
- [16] N. Xiao, D. Lau, W. Shi et al., "A simple process to prepare nitrogen-modified few-layer graphene for a supercapacitor electrode," *Carbon*, vol. 57, pp. 184–190, 2013.
- [17] Y. Gao, Y. S. Zhou, M. Qian et al., "Chemical activation of carbon nano-onions for high-rate supercapacitor electrodes," *Carbon*, vol. 51, no. 1, pp. 52–58, 2013.
- [18] Y. P. Zhai, Y. Q. Dou, D. Y. Zhao, P. F. Fulvio, R. T. Mayes, and S. Dai, "Carbon materials for chemical capacitive energy storage," *Advanced Materials*, vol. 23, no. 42, pp. 4828–4850, 2011.
- [19] R. B. Rakhi, W. Chen, D. Cha, and H. N. Alshareef, "Substrate dependent self-organization of mesoporous cobalt oxide nanowires with remarkable pseudocapacitance," *Nano Letters*, vol. 12, no. 5, pp. 2559–2567, 2012.
- [20] Y. B. He, G. R. Li, Z. L. Wang, C. Y. Su, and Y. X. Tong, "Single-crystal ZnO nanorod/amorphous and nanoporous metal oxide shell composites: controllable electrochemical synthesis and enhanced supercapacitor performances," *Energy & Environmental Science*, vol. 4, no. 4, pp. 1288–1292, 2011.
- [21] M. Ghaemi, F. Ataherian, A. Zolfaghari, and S. M. Jafari, "Charge storage mechanism of sonochemically prepared MnO₂ as supercapacitor electrode: Effects of physisorbed water and proton conduction," *Electrochimica Acta*, vol. 53, no. 14, pp. 4607–4614, 2008.
- [22] S. Dong, X. Chen, L. Gu et al., "One dimensional MnO₂/titanium nitride nanotube coaxial arrays for high performance electrochemical capacitive energy storage," *Energy & Environmental Science*, vol. 4, no. 9, pp. 3502–3508, 2011.
- [23] L. Bao, J. Zang, and X. Li, "Flexible Zn₂SnO₄/MnO₂ core/shell nanocable-carbon microfiber hybrid composites for high-performance supercapacitor electrodes," *Nano Letters*, vol. 11, no. 3, pp. 1215–1220, 2011.
- [24] M. Yu, T. Zhai, X. Lu et al., "Manganese dioxide nanorod arrays on carbon fabric for flexible solid-state supercapacitors," *Journal of Power Sources*, vol. 239, pp. 64–71, 2013.
- [25] P. Yu, X. Zhang, D. Wang, L. Wang, and Y. Ma, "Shape-controlled synthesis of 3D hierarchical MnO₂ nanostructures for electrochemical supercapacitors," *Crystal Growth and Design*, vol. 9, no. 1, pp. 528–533, 2009.
- [26] S. Devaraj and N. Munichandraiah, "Effect of crystallographic structure of MnO₂ on its electrochemical capacitance properties," *The Journal of Physical Chemistry C*, vol. 112, no. 11, pp. 4406–4417, 2008.
- [27] N. Nagarajan, M. Cheong, and I. Zhitomirsky, "Electrochemical capacitance of MnO_x films," *Materials Chemistry and Physics*, vol. 103, no. 1, pp. 47–53, 2007.
- [28] T. Zhai, X. Lu, Y. Ling et al., "A new benchmark capacitance for supercapacitor anodes by mixed-valence sulfur-doped V₆O_{13-x}," *Advanced Materials*, vol. 26, no. 33, pp. 5869–5875, 2014.
- [29] X. Lu, M. Yu, G. Wang et al., "H-TiO₂@MnO₂//H-TiO₂@C core-shell nanowires for high performance and flexible asymmetric supercapacitors," *Advanced Materials*, vol. 25, no. 2, pp. 267–272, 2013.
- [30] H. Xia, J. Feng, H. Wang, M. O. Lai, and L. Lu, "MnO₂ nanotube and nanowire arrays by electrochemical deposition for supercapacitors," *Journal of Power Sources*, vol. 195, no. 13, pp. 4410–4413, 2010.

- [31] S.-L. Chou, J.-Z. Wang, S.-Y. Chew, H.-K. Liu, and S.-X. Dou, "Electrodeposition of MnO₂ nanowires on carbon nanotube paper as free-standing, flexible electrode for supercapacitors," *Electrochemistry Communications*, vol. 10, no. 11, pp. 1724–1727, 2008.
- [32] H. Zhu, X. Wang, X. Liu, and X. Yang, "Integrated synthesis of poly(O-phenylenediamine)-derived carbon materials for high performance supercapacitors," *Advanced Materials*, vol. 24, no. 48, pp. 6524–6529, 2012.

Research Article

ZnO Nanocrystals as Anode Electrodes for Lithium-Ion Batteries

Wenhui Zhang,¹ Lijuan Du,¹ Zongren Chen,¹ Juan Hong,² and Lu Yue¹

¹Jiangsu Collaborative Innovation Center for Ecological Building Materials and Environmental Protection Equipments, Key Laboratory for Advanced Technology in Environmental Protection of Jiangsu Province, Yancheng Institute of Technology, Yancheng 224051, China

²College of Mechanical Engineering, Yancheng Institute of Technology, Yancheng 224051, China

Correspondence should be addressed to Juan Hong; jameshong@ycit.cn and Lu Yue; yuelu66@126.com

Received 8 March 2016; Accepted 24 April 2016

Academic Editor: Gongming Wang

Copyright © 2016 Wenhui Zhang et al. This is an open access article distributed under the Creative Commons Attribution License, which permits unrestricted use, distribution, and reproduction in any medium, provided the original work is properly cited.

ZnO nanocrystals were synthesized via a thermal decomposition method. X-ray diffraction, transmission electron microscopy, and photoluminescence were used to investigate the composition and nanostructure of the material. Compared with commercial ZnO nanoparticles, ZnO nanocrystals showed higher lithium storage capacity and better cycling characteristics and exhibited a reversible discharge capacity of 500 mAh g⁻¹ after 100 cycles at 200 mA g⁻¹.

1. Introduction

Transition metal oxides have gained more and more interest as electrode materials in lithium-ion batteries in the last decades because of their higher theoretical capacity and safety compared with the conventional carbon materials [1–4]. Among them, ZnO, a wide-bandgap semiconductor of 3.37 eV at room temperature with large exciton binding energy of 60 meV, is a multifunctional material for a variety of practical applications such as piezoelectric devices [5], field emission [6], gas sensors [7], dye-sensitized solar cells [8], and photocatalysts [9] due to its excellent physical and chemical properties. ZnO has superior advantages such as low cost, facile preparation, morphologic diversity, and high chemical stability. ZnO nanocrystals with different morphologies have some special properties of physics, so intense interests have been devoted to the synthesis of ZnO with various morphologies such as nanowires [10], nanobelts [11], nanorods [12], and nanosheets [13].

As an anode material of lithium-ion batteries, ZnO has a theoretical capacity of 978 mAh g⁻¹ [14]. However, the poor electronic conductivity, large volume change during lithium/delithium process, and the resulting severe capacity fading hinder its practical application [15]. Hitherto, some efforts have been made to improve its cycling performance including synthesis of nanostructures [15–17], doping and

forming composite with metal [18, 19], metal oxide [20–22], carbon [23, 24], and graphene [25, 26]. For example, dandelion-like ZnO nanorod arrays showed higher lithium storage capacity and better cycling characteristics compared to powder-form ZnO [27]. Mesoporous ZnO nanosheets exhibit a 50th charge capacity of 420 mAh g⁻¹, and the capacity and cycling performance are enhanced compared with those of common solid ZnO particles [17]. More significant research efforts are needed to further improve the lithium-ion battery performances of ZnO.

In the present work, ZnO nanocrystals have been prepared by a thermal decomposition method and their electrochemical performances as lithium anode materials are investigated.

2. Experimental Section

2.1. Preparation of ZnO Nanocrystals. 0.316 g zinc stearate (Zn(St)₂, 10–12% Zn basis, Sigma-Aldrich) and 10 g 1-octadecene (ODE, technical grade, 90%, Sigma-Aldrich) were loaded in a 50 mL three-necked flask, degassed, and heated to 270°C under an argon flow. A separate solution of 2.5 g ODE containing 0.676 g 1-octadecanol (ODA, 95%, Sigma-Aldrich) at 200°C was rapidly injected into the reaction flask to generate nanocrystals. The reaction was allowed

to proceed for 30 min. When the reaction was finished, the reaction mixture was cooled to room temperature. The resulting nanocrystals were precipitated out by adding ethyl acetate, carefully purified with hexane/ethanol mixtures, and dried at 70°C. Ethyl acetate (AR), hexane (AR), and ethanol (AR) were purchased from Sinopharm Chemical Reagent Co. Commercial ZnO nanoparticles (30 ± 10 nm) were purchased from Aladdin Industrial Corporation for comparison.

2.2. Characterization of ZnO Nanocrystals. Powder X-ray diffraction (XRD) analyses were performed on a Philips PW-1830 X-ray diffractometer with Cu K α irradiation ($\lambda = 1.5406 \text{ \AA}$) at a scanning speed of 0.014°/sec over the 2θ range of 30–60°. The electronic morphology of the samples was examined by a transmission electron microscope (TEM; FEI Tecnai G2 Spirit, USA). Photoluminescence (PL) spectra of the sample on Si substrate were recorded using Jobin-Yvon LabRAM high-resolution spectrometer with He-Cd laser ($\lambda = 325 \text{ nm}$). Cyclic voltammetry (CV) and electrochemical impedance spectroscopy (EIS) results were obtained with Zennium/IM6 electrochemical workstation (Zahner, Germany).

2.3. Electrochemical Performance. The coin cells (CR2025) were assembled to test the electrochemical performance of the as-prepared electrodes. The as-prepared samples were mixed with acetylene black and carboxymethyl cellulose, in a weight ratio of 60:20:20 in an aqueous solution to form homogeneous slurry. The slurry was spread onto 10 μm thick copper foil and dried at 60°C for 12 h in a vacuum oven and then pressed to obtain the electrode sheet with a 9–10 μm coating thickness and a loading level of about 1.4 mg cm^{-2} . The electrolyte of 1 M LiPF₆ and 5% fluoroethylene carbonate (FEC) in ethylene carbonate (EC, >99.9%)/diethylene carbonate (DEC, >99.9%)/dimethyl carbonate (DMC, >99.9%) (v:v:v = 1:1:1, water content <20 ppm) was purchased from Zhangjiagang Guotai-Huarong New Chemical Materials Company (China). The cells were assembled in an Ar filled glove-box. The cells were charged and discharged galvanostatically in the fixed voltage window from 0.01 V to 3 V on a Shenzhen Neware battery cycler (China) at 25°C.

EIS was measured by applying an alternating voltage of 5 mV over the frequency ranging from 10⁻² to 10⁵ Hz. In this work, unless otherwise specified, all impedance measurements were carried out after one cycle of the prepared electrode.

3. Results and Discussion

The crystal structure of the sample was characterized by XRD, as shown in Figure 1. All diffraction peaks can be indexed as the hexagonal phase of ZnO, which is in good agreement with JCPDS number 36-1451.

The typical morphology of ZnO nanocrystals and commercial ZnO nanoparticles, as observed by TEM, is presented in Figure 2. It can be seen that the reaction generated trigonal ZnO nanocrystals with the size of 10–15 nm (side-edge length). The diameter of commercial ZnO nanoparticles was 30 ± 10 nm.

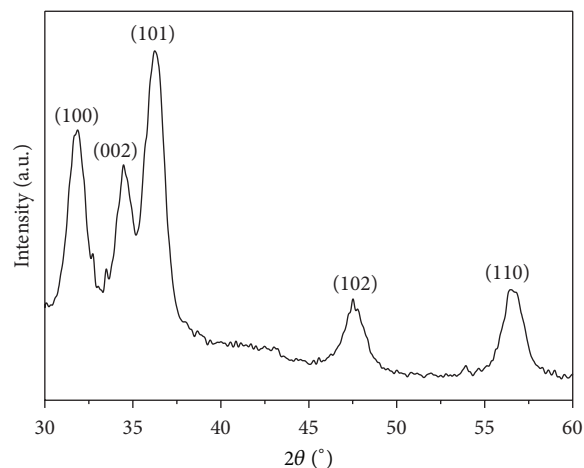


FIGURE 1: XRD pattern of ZnO nanocrystals.

PL spectrum of the sample is shown in Figure 3. Strong excitonic emission at 375 nm and a broad but weak spectral band ranging from 450 to 600 nm were observed. The near-UV peak is due to the recombination of electron and hole in an exciton, while the visible emission is due to the presence of various point defects, such as interstitial oxygen and oxygen vacancies.

The electrochemical properties of ZnO nanocrystal and commercial ZnO nanoparticle electrode for lithium-ion batteries were investigated. Figure 4 reveals the CV of the electrodes at a scan rate of 0.5 mV s^{-1} in the voltage ranging from 0.01 to 3 V. Both of the first discharge process (negative scan) of ZnO nanocrystal and the commercial ZnO electrodes showed broad peaks around 1.2–1.0 V and 0.5–0.7 V and a sharp reduction peak below 0.3 V, corresponding to the irreversible reactions (the reaction of FEC decomposition and formation of primal solid electrolyte interface (SEI) film on the surface of composite electrode) and the insertion of Li ions into ZnO, respectively. The relative peak at 0.5 V originated from the reduction of ZnO into Zn and the formation of amorphous Li₂O, while the strong peak near 0.25 V was caused by the generation of Li-Zn alloy together with the decomposition of electrolyte. These peaks disappeared in further cycles, indicating the irreversible reduction of ZnO with a large irreversible capacity in the first cycle. New reduction peaks at about 0.80 and 0.30 V appeared after the first cycle and shifted to a lower voltage during further cycles. In the subsequent delithium process for ZnO nanocrystals (Figure 4(a)), six weak oxidation peaks centred at 0.27, 0.52, 0.63, 1.48, 1.78, and 2.20 V could be carefully discerned which could be attributed to multistep dealloying of Li-Zn alloy. However, for commercial ZnO electrode (Figure 4(b)), only two oxidation peaks of 0.65 and 1.52 V could be found in the CV curves. Besides, the ZnO nanocrystal electrode displayed a higher peak current in both oxidation-reduction reaction processes, indicating that a better and more active electrode reaction happened.

The cycling performances of ZnO nanocrystal and commercial ZnO nanoparticle electrode at a current density

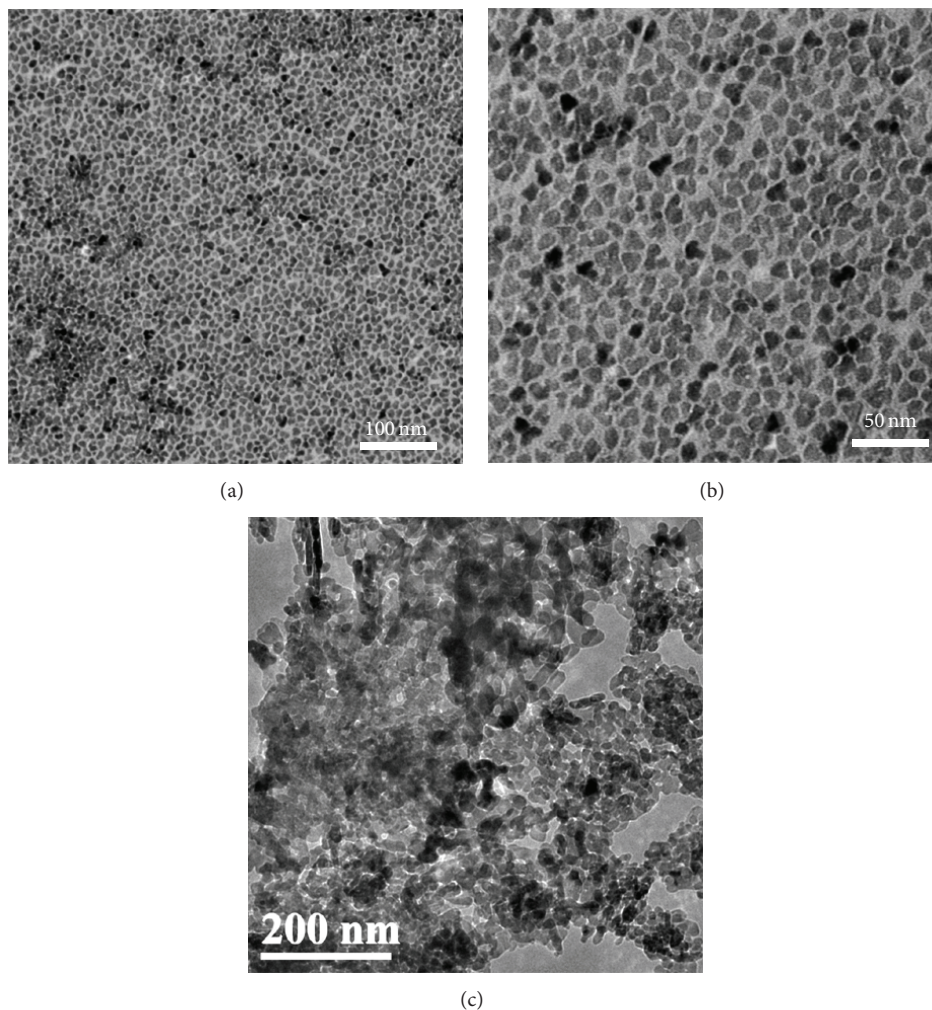


FIGURE 2: TEM images of (a, b) ZnO nanocrystals and (c) commercial ZnO nanoparticles.

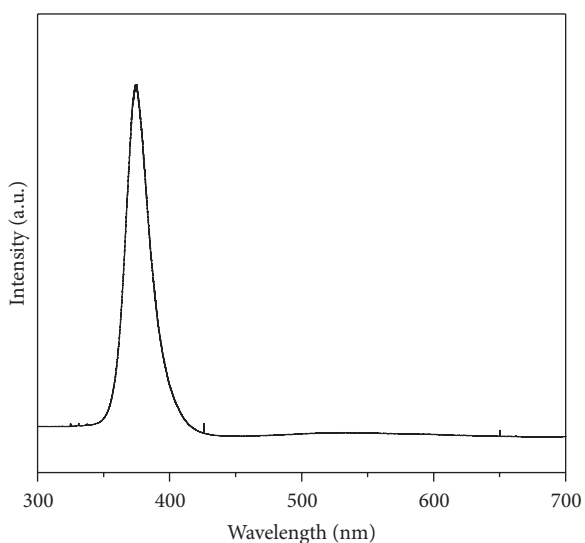


FIGURE 3: PL spectrum of ZnO nanocrystals.

of 200 mA g^{-1} and 400 mA g^{-1} were displayed in Figure 5. At 200 mA g^{-1} , ZnO nanocrystal electrode delivered a high initial charge/discharge capacity of $709/1563 \text{ mAh g}^{-1}$ and exhibited a high average discharge capacity of 500 mAh g^{-1} over 100 cycles, while commercial ZnO nanoparticle electrode delivered a lower initial charge/discharge capacity of $489/1273 \text{ mAh g}^{-1}$ and exhibited a lower average discharge capacity of 112 mAh g^{-1} over 100 cycles. At 400 mA g^{-1} , the electrodes showed similar results. The ZnO nanocrystal electrode displayed a better cycling performance, which delivered an initial charge/discharge capacity of $676/1475 \text{ mAh g}^{-1}$ with a coulombic efficiency of 45.8% and exhibited the discharge capacity of 428 mAh g^{-1} over 100 cycles.

The rate capabilities of ZnO nanocrystal electrode are shown in Figure 6. ZnO nanocrystal electrode was cycled at a current density of 200 mA g^{-1} for the initial 2 cycles. Then, the current density was increased gradually to 4000 mA g^{-1} and finally returned to 200 mA g^{-1} . The ZnO nanocrystal

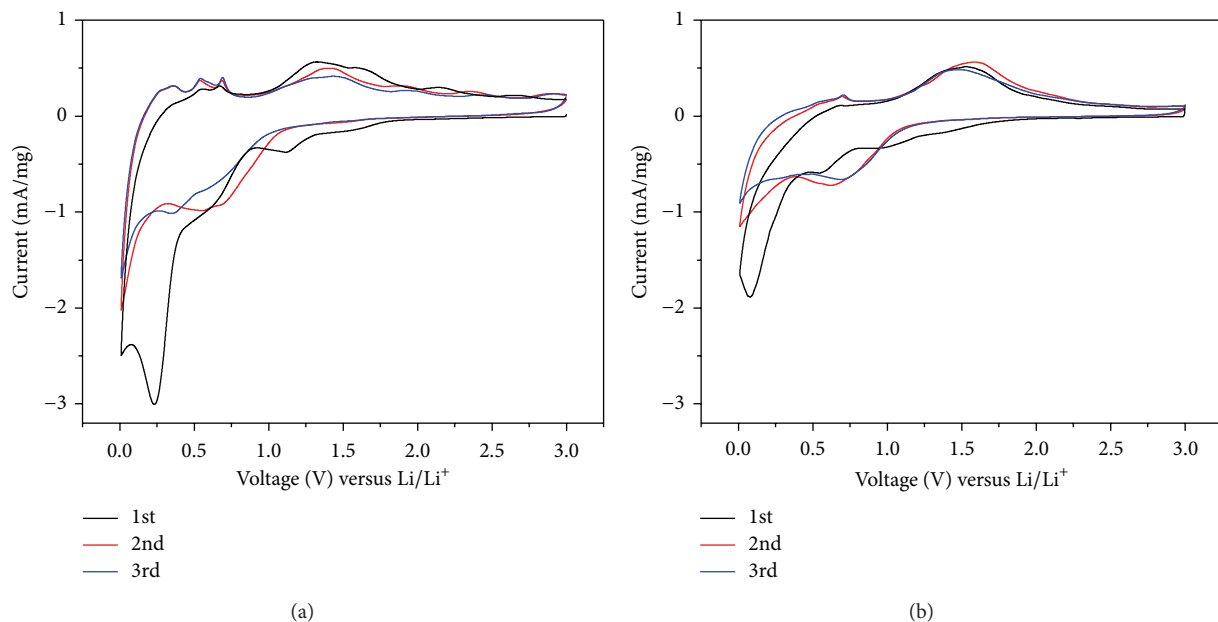


FIGURE 4: Cyclic voltammograms of (a) ZnO nanocrystal and (b) commercial ZnO nanoparticle electrode tested at 0.5 mV s^{-1} in 0.01–3 V.

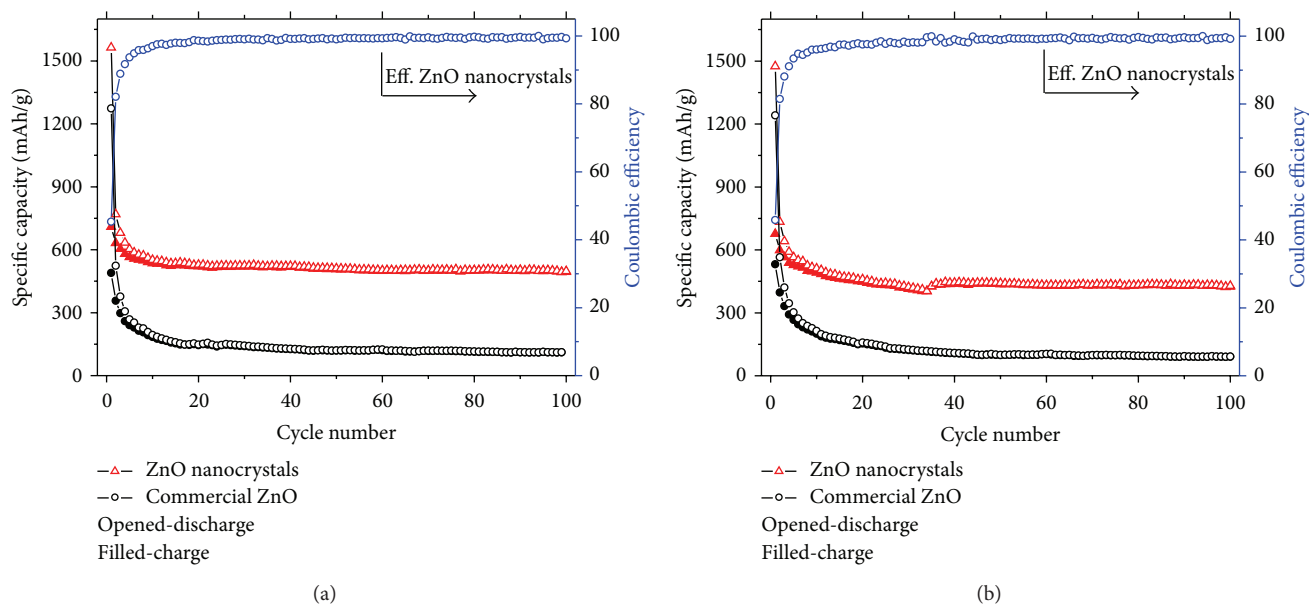


FIGURE 5: Cycle performances of ZnO nanocrystal and commercial ZnO nanoparticle electrode at a current density of (a) 200 mA g^{-1} and (b) 400 mA g^{-1} .

electrode showed a first charge/discharge capacity of $570/1272 \text{ mAh g}^{-1}$ with a coulombic efficiency of 44.8%. At a higher current density of 500, 1000, 2000, 3000, and 4000 mA g^{-1} , the capacity dropped to about 309, 187, 114, 75, and 51 mAh g^{-1} , respectively.

To investigate the difference in electrochemical performance, EIS was employed to characterize the impedance properties of electrodes. The Nyquist complex plane impedance plots of the electrodes after the first two charge/discharge cyclic processes are presented in Figure 7. Both Nyquist plots

which consisted of a depressed semicircle at high frequency range correlated with the electron transfer resistance on the interface of electrode/electrolyte. These Nyquist plots were fitted with the equivalent circuit (inset), as shown in Figure 7. This equivalent circuit consisted of a series of four resistors elements, three constant-phase elements (CPE), and a Warburg diffusion element. In the equivalent circuit, R_1 was composed of the electrolyte resistance (R_s) and the electrode resistance (R_e); R_2 represented the SEI film resistances; R_3 represented the interphase electronic contacts

TABLE 1

Sample ID	R_1 (Ω)	R_2 (Ω)	R_3 (Ω)	R_4 (Ω)	CPE ₁		CPE ₂		CPE ₃		W (DW)
					$Y_{0,1}$ (μF)	n	$Y_{0,2}$ (μF)	n	$Y_{0,3}$ (μF)	n	
Commercial ZnO	0.3	1.7	107.1	43.1	0.55	0.4	4.7	0.8	103.5	0.7	69.2
ZnO nanocrystals	0.3	1.3	53.4	22.2	0.91	0.4	6.2	0.6	280.5	0.6	47.6

Y_0 and n are two parameters of the constant-phase element.

TABLE 2: Electrochemical performance comparison of ZnO-based anodes for lithium-ion batteries.

The structure of the material	Specific discharge capacity (mAh g^{-1})	Cycle number	Current density	References
ZnO radial hollow microparticles	320	100	200 mA g^{-1}	[28]
ZnO nanowires	252	30	120 mA g^{-1}	[29]
ZnO flower-like microaggregates	179	200	1 C	[30]
ZnO dandelion-like nanorod arrays	310	40	250 mA g^{-1}	[27]
ZnO flower-like arrays	238	50	0.5 C	[31]
ZnO microrod arrays	150	50	500 mA g^{-1}	[16]
ZnO nanowire arrays	200	40	120 mA g^{-1}	[32]
ZnO flower-like microparticles	200	50	120 mA g^{-1}	[33]
ZnO nanoplates	368	100	0.1 C	[34]
ZnO mesoporous nanosheets	420	50	100 mA g^{-1}	[17]
Flower-like ZnO nanospheres	381	30	0.5 C	[35]
Ultralong mesoporous ZnO nanowires	432	10	0.1 C	[36]
ZnO nanocrystals	500	100	200 mA g^{-1}	This work
	428		400 mA g^{-1}	

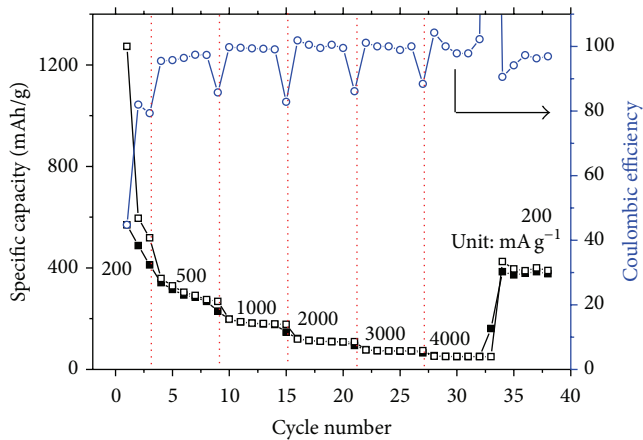


FIGURE 6: Rate performance of ZnO nanocrystal electrode.

resistance; R_4 was the charge-transfer resistance across electrode/electrolyte interface; CPE₁ and CPE₂ were attributed to the Li^+ diffusion in the SEI film and pore channel of the electrode materials, respectively; CPE₃ represented the electric double-layer capacitance of electrode/solution interface; Z_W which represented Warburg impedance was related to the semi-infinite diffusion of lithium ions into the bulk electrode [37, 38].

By fitting the impedance data, the typical parameters were obtained and summarized in Table 1. It was seen that the smaller R_3 was also observed in ZnO nanocrystal electrode,

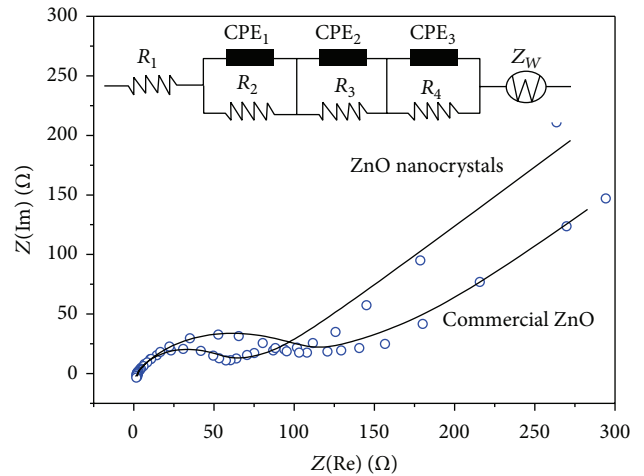


FIGURE 7: Nyquist plots for ZnO nanocrystal and commercial ZnO nanoparticle electrodes. The spots correspond to the experimental data, and the solid lines stand for the calculated data from the equivalent circuits of inset.

which usually favored the fast transport of Li^+ ions and the electrons across the interface. It also indicated that the carbon layer supplied fast charge-transfer channels on the interface of ZnO nanocrystal. $Y_{0,1}$, $Y_{0,2}$, and $Y_{0,3}$ of the ZnO nanocrystal electrode were higher than those of commercial ZnO electrode. The increase of $Y_{0,3}$ representing the electric double-layer capacitance favored the charge transfer for the

electrode reaction. And the increase of $Y_{0,1}$ and $Y_{0,2}$ favored the diffusion of Li^+ in the SEI film and within the pore channels in the electrode, respectively.

ZnO nanocrystal electrode showed a smaller charge-transfer resistance and higher electric double-layer capacitance as compared with the commercial ZnO electrode, indicating an improved kinetic character of electrode reactions (i.e., charge transfer and polarization) which could be ascribed to the better availability of electrons and perhaps also Li^+ . The smaller particle size and better crystal type constituted a fast pathway for mass transport and electron transfer and hence improved Li storage capacity. The excellent capacity of the ZnO nanocrystals is highly attractive when compared with other reported ZnO-based anode materials (Table 2).

4. Conclusion

In summary, ZnO nanocrystals with side-edge length of 10–15 nm were synthesized via the thermal decomposition method. A high reversible discharge capacity of 500 mAh g^{-1} of ZnO nanocrystals was observed after 100 cycles at 200 mA g^{-1} . Compared with commercial ZnO nanoparticles, ZnO nanocrystals showed higher lithium storage capacity. These results are attributed to the structural difference of ZnO nanocrystals resulting in different cell impedance, which affects the Li-ion diffusion.

Competing Interests

The authors declare that there are no competing interests regarding the publication of this paper.

Acknowledgments

This study is supported by the National Natural Science Foundation of China (nos. 51402252 and 51541505) and the Natural Science Foundation of Jiangsu Province (no. BK20140463).

References

- [1] A. K. Mondal, D. Su, S. Chen, A. Ung, H.-S. Kim, and G. Wang, "Mesoporous MnCo_2O_4 with a flake-like structure as advanced electrode materials for lithium-ion batteries and supercapacitors," *Chemistry—A European Journal*, vol. 21, no. 4, pp. 1526–1532, 2015.
- [2] N. N. Wang, X. J. Ma, H. Y. Xu et al., "Porous ZnMn_2O_4 microspheres as a promising anode material for advanced lithium-ion batteries," *Nano Energy*, vol. 6, pp. 193–199, 2014.
- [3] W. Zhang, L. Yue, F. Zhang et al., "One-step in situ synthesis of ultrathin tungsten oxide@carbon nanowire webs as an anode material for high performance," *Journal of Materials Chemistry A*, vol. 3, no. 11, pp. 6102–6109, 2015.
- [4] Y. Zhu, C. Cao, J. Zhang, and X. Xu, "Two-dimensional ultrathin ZnCo_2O_4 nanosheets: general formation and lithium storage application," *Journal of Materials Chemistry A*, vol. 3, no. 18, pp. 9556–9564, 2015.
- [5] C. F. Pan, R. M. Yu, S. M. Niu, G. Zhu, and Z. L. Wang, "Piezotronic effect on the sensitivity and signal level of schottky contacted proactive micro/nanowire nanosensors," *ACS Nano*, vol. 7, no. 2, pp. 1803–1810, 2013.
- [6] Y.-H. Tan, K. Yu, J.-Z. Li, H. Fu, and Z.-Q. Zhu, "MoS₂@ZnO nano-heterojunctions with enhanced photocatalysis and field emission properties," *Journal of Applied Physics*, vol. 116, no. 6, Article ID 064305, 2014.
- [7] Y. D. Zhu, Y. Y. Wang, G. T. Duan et al., "In situ growth of porous ZnO nanosheet-built network film as high-performance gas sensor," *Sensors and Actuators B: Chemical*, vol. 221, Article ID 18692, pp. 350–356, 2015.
- [8] L. X. Song, P. F. Du, J. Xiong, F. Ko, and C. Cui, "Efficiency enhancement of dye-sensitized solar cells by optimization of electrospun ZnO nanowire/nanoparticle hybrid photoanode and combined modification," *Electrochimica Acta*, vol. 163, pp. 330–337, 2015.
- [9] Y. Wang, H. Fang, Y. Zheng, R. Ye, X. Tao, and J. Chen, "Controllable assembly of well-defined monodisperse Au nanoparticles on hierarchical ZnO microspheres for enhanced visible-light-driven photocatalytic and antibacterial activity," *Nanoscale*, vol. 7, no. 45, pp. 19118–19128, 2015.
- [10] Y. F. Yang, Y. Z. Jin, H. P. He et al., "Dopant-induced shape evolution of colloidal nanocrystals: the case of zinc oxide," *Journal of the American Chemical Society*, vol. 132, no. 38, pp. 13381–13394, 2010.
- [11] L. Nasi, D. Calestani, F. Fabbri et al., "Mesoporous single-crystal ZnO nanobelts: supported preparation and patterning," *Nanoscale*, vol. 5, no. 3, pp. 1060–1066, 2013.
- [12] Y.-J. Wu, C.-H. Liao, C.-Y. Hsieh et al., "Local electronic structures and polarity of ZnO nanorods grown on GaN substrates," *Journal of Physical Chemistry C*, vol. 119, no. 9, pp. 5122–5128, 2015.
- [13] A. Umar, M. S. Akhtar, M. S. Al-Assiri et al., "Highly porous ZnO nanosheets self-assembled in rosette-like morphologies for dye-sensitized solar cell application," *New Journal of Chemistry*, vol. 39, no. 10, pp. 7961–7970, 2015.
- [14] Q. Pan, L. Qin, J. Liu, and H. Wang, "Flower-like ZnO-NiO-C films with high reversible capacity and rate capability for lithium-ion batteries," *Electrochimica Acta*, vol. 55, no. 20, pp. 5780–5785, 2010.
- [15] X. H. Huang, X. H. Xia, Y. F. Yuan, and F. Zhou, "Porous ZnO nanosheets grown on copper substrates as anodes for lithium ion batteries," *Electrochimica Acta*, vol. 56, no. 14, pp. 4960–4965, 2011.
- [16] X. H. Huang, J. B. Wu, Y. Lin, and R. Q. Guo, "ZnO microrod arrays grown on copper substrates as anode materials for lithium ion batteries," *International Journal of Electrochemical Science*, vol. 7, no. 8, pp. 6611–6621, 2012.
- [17] X. H. Huang, R. Q. Guo, J. B. Wu, and P. Zhang, "Mesoporous ZnO nanosheets for lithium ion batteries," *Materials Letters*, vol. 122, pp. 82–85, 2014.
- [18] L. F. Zhang, J. Z. Zhang, Y. Liu, P. Zheng, X. Y. Yuan, and S. W. Guo, "Al doped-ZnO nanoparticles implanted in reduced graphene oxide with improved electrochemical properties for lithium ion batteries," *Materials Letters*, vol. 165, pp. 165–168, 2016.
- [19] X. Shen, D. Mu, S. Chen, R. Huang, and F. Wu, "Electrospun composite of ZnO/Cu nanocrystals-implanted carbon fibers as an anode material with high rate capability for lithium ion batteries," *Journal of Materials Chemistry A*, vol. 2, no. 12, pp. 4309–4315, 2014.
- [20] M. S. Song, S. Nahm, W. I. Cho, and C. Lee, "Enhanced electrochemical performance of a ZnO-MnO composite as an anode

- material for lithium ion batteries,” *Physical Chemistry Chemical Physics*, vol. 17, no. 36, pp. 23496–23502, 2015.
- [21] Y. Zhao, X. Li, L. Dong et al., “Electrospun SnO₂-ZnO nanofibers with improved electrochemical performance as anode materials for lithium-ion batteries,” *International Journal of Hydrogen Energy*, vol. 40, no. 41, pp. 14338–14344, 2015.
- [22] C. Y. Zhang, J. Dai, P. G. Zhang et al., “Porous Fe₂O₃/ZnO composite derived from MOFs as an anode material for lithium ion batteries,” *Ceramics International*, vol. 42, no. 1, pp. 1044–1049, 2016.
- [23] Y. Xiao and M. Cao, “Dual hybrid strategy towards achieving high capacity and long-life lithium storage of ZnO,” *Journal of Power Sources*, vol. 305, pp. 1–9, 2016.
- [24] G. Zhang, S. Hou, H. Zhang et al., “High-performance and ultra-stable lithium-ion batteries based on MOF-derived ZnO@ZnO quantum dots/C core-shell nanorod arrays on a carbon cloth anode,” *Advanced Materials*, vol. 27, no. 14, pp. 2400–2405, 2015.
- [25] X. Sun, C. Zhou, M. Xie et al., “Synthesis of ZnO quantum dot/graphene nanocomposites by atomic layer deposition with high lithium storage capacity,” *Journal of Materials Chemistry A*, vol. 2, no. 20, pp. 7319–7326, 2014.
- [26] C.-T. Hsieh, C.-Y. Lin, Y.-F. Chen, and J.-S. Lin, “Synthesis of ZnO@Graphene composites as anode materials for lithium ion batteries,” *Electrochimica Acta*, vol. 111, pp. 359–365, 2013.
- [27] H. Wang, Q. Pan, Y. Cheng, J. Zhao, and G. Yin, “Evaluation of ZnO nanorod arrays with dandelion-like morphology as negative electrodes for lithium-ion batteries,” *Electrochimica Acta*, vol. 54, no. 10, pp. 2851–2855, 2009.
- [28] G. Yuan, G. Wang, H. Wang, and J. Bai, “Synthesis and electrochemical investigation of radial ZnO microparticles as anode materials for lithium-ion batteries,” *Ionics*, vol. 21, no. 2, pp. 365–371, 2015.
- [29] J. Wang, N. Du, H. Zhang, J. Yu, and D. Yang, “Layer-by-layer assembly synthesis of ZnO/SnO₂ composite nanowire arrays as high-performance anode for lithium-ion batteries,” *Materials Research Bulletin*, vol. 46, no. 12, pp. 2378–2384, 2011.
- [30] V. Cauda, D. Pugliese, N. Garino et al., “Multi-functional energy conversion and storage electrodes using flower-like Zinc oxide nanostructures,” *Energy*, vol. 65, pp. 639–646, 2014.
- [31] Z. Wu, L. Qin, and Q. Pan, “Fabrication and electrochemical behavior of flower-like ZnO-CoO-C nanowall arrays as anodes for lithium-ion batteries,” *Journal of Alloys and Compounds*, vol. 509, no. 37, pp. 9207–9213, 2011.
- [32] M. Ahmad, S. Yingying, H. Sun, W. C. Shen, and J. Zhu, “SnO₂/ZnO composite structure for the lithium-ion battery electrode,” *Journal of Solid State Chemistry*, vol. 196, pp. 326–331, 2012.
- [33] M. Ahmad, S. Yingying, A. Nisar et al., “Synthesis of hierarchical flower-like ZnO nanostructures and their functionalization by Au nanoparticles for improved photocatalytic and high performance Li-ion battery anodes,” *Journal of Materials Chemistry*, vol. 21, no. 21, pp. 7723–7729, 2011.
- [34] H. Li, Y. Wei, Y. Zhao et al., “Simple one-pot synthesis of hexagonal ZnO nanoplates as anode material for lithium-ion batteries,” *Journal of Nanomaterials*, vol. 2016, Article ID 4675960, 6 pages, 2016.
- [35] F. Li, L. L. Yang, G. Xu et al., “Hydrothermal self-assembly of hierarchical flower-like ZnO nanospheres with nanosheets and their application in Li-ion batteries,” *Journal of Alloys and Compounds*, vol. 577, pp. 663–668, 2013.
- [36] H.-J. Yang, S.-C. Lim, S.-Y. He, and H.-Y. Tuan, “Ultralong mesoporous ZnO nanowires grown via room temperature self-assembly of ZnO nanoparticles for enhanced reversible storage in lithium ion batteries,” *RSC Advances*, vol. 5, no. 42, pp. 33392–33399, 2015.
- [37] L. Yue, W. Zhang, W. Zhang et al., “One-step solvothermal process of In₂O₃/C nanosheet composite with double phases as high-performance lithium-ion battery anode,” *Electrochimica Acta*, vol. 160, pp. 123–130, 2015.
- [38] W. Zhang, L. Wu, L. Du et al., “Layer-by-layer assembly modification to prepare firmly bonded Si-graphene composites for high-performance anodes,” *RSC Advances*, vol. 6, no. 6, pp. 4835–4842, 2016.

Research Article

Effect of Na Doping on the Nanostructures and Electrical Properties of ZnO Nanorod Arrays

Lu Yue,^{1,2} Zhiqiang Zhang,^{1,2} Yanyan Ma,^{1,2} and Wenhui Zhang^{1,2}

¹Jiangsu Collaborative Innovation Center for Ecological Building Materials and Environmental Protection Equipment, Yancheng Institute of Technology, Yancheng 224051, China

²Key Laboratory for Advanced Technology in Environmental Protection of Jiangsu Province, Yancheng Institute of Technology, Yancheng 224051, China

Correspondence should be addressed to Wenhui Zhang; zwhuizi000@sina.com

Received 9 March 2016; Accepted 5 May 2016

Academic Editor: Gongming Wang

Copyright © 2016 Lu Yue et al. This is an open access article distributed under the Creative Commons Attribution License, which permits unrestricted use, distribution, and reproduction in any medium, provided the original work is properly cited.

The p-type ZnO nanorod arrays were prepared by doping Na with hydrothermal method. The structural, electrical, and optical properties were explored by XRD, Hall-effect, PL, and Raman spectra. The carrier concentrations and the mobility of Na-doped ZnO nanorod arrays are arranged from $1.4 \times 10^{16} \text{ cm}^{-3}$ to $1.7 \times 10^{17} \text{ cm}^{-3}$ and $0.45 \text{ cm}^2 \text{ v}^{-1} \text{ s}^{-1}$ to $106 \text{ cm}^2 \text{ v}^{-1} \text{ s}^{-1}$, respectively.

1. Introduction

Zinc oxide (ZnO) is a promising material candidate for photoelectronic devices due to its direct wide electron energy bandgap of 3.37 eV at room temperature and large exciton binding energy of 60 meV. ZnO is conventionally used as a substrate for GaN and has advantages over GaN such as larger exciton binding energy, lower refraction index, and shallower acceptor levels. Despite its advantages over GaN, the application of ZnO in optoelectronics is hampered by the lack of stable p-type doping due to self-compensation by donor-like native defects, low solubility of p-type dopants, and formation of deep acceptor levels [1]. The n-type ZnO is available even without any intentional doping, but it is very difficult to dope ZnO p-type. Many groups have realized p-type ZnO conversion by doping group V elements (N [2], P [3], As [4], and Sb [5]) and groups I and IB (Li [6], Na [7–9], K [10], Ag [11], and Cu [12]), but the stability was not good. Among the group V elements, N is the most suitable dopant because it has about the same ionic radius as O and thus should readily be substituted on O sites. Indeed, it remains difficult to achieve good quality p-type conduction in N-doped ZnO due to either a low dopant solubility or a high defect ionization energy. Theoretically, group I element substituted on Zn sites is shallow acceptors [13], but instead these dopants tend to occupy the interstitial sites, partly due

to their small atomic radius, and therefore act mainly as donors. On the other hand, reports of Na-doped p-type ZnO films are rather poor [14]. Up to now, various methods have been employed to prepare p-type ZnO including molecular beam epitaxy (MBE) [15], chemical vapor deposition [16], and pulsed laser deposition [17], in which complicated, high temperature deposition and expensive vacuum systems have been employed. In contrast, the hydrothermal method was proven to be an ideal technique for the development of p-type ZnO films owing to its simplicity and easy control of the composition at low cost [18–20]. To date, there is no report of Na doping of p-type ZnO nanorods by a hydrothermal method. Here, we report a simple, reliable, and low-cost method for growing and doping p-type ZnO nanorod arrays in aqueous solution, with Na as the p-type dopant.

2. Experimental Section

A high-resistance Si (100) wafer, the resistivity of which is above $500 \Omega \text{ cm}$, was used as the substrate. Precleaned silicon substrate was coated with a ZnO seed layer by sol-gel spin coating. $\text{Zn}(\text{AC})_2 \cdot 2\text{H}_2\text{O}$ were first dissolved in the mixture of 2-methoxyethanol and monoethanolamine. The molar ratio of monoethanolamine to $\text{Zn}(\text{AC})_2 \cdot 2\text{H}_2\text{O}$ was maintained at 1:1 and the concentration of $\text{Zn}(\text{AC})_2 \cdot 2\text{H}_2\text{O}$ was 75 mM. The sol was aged for 24 h at room temperature. The above

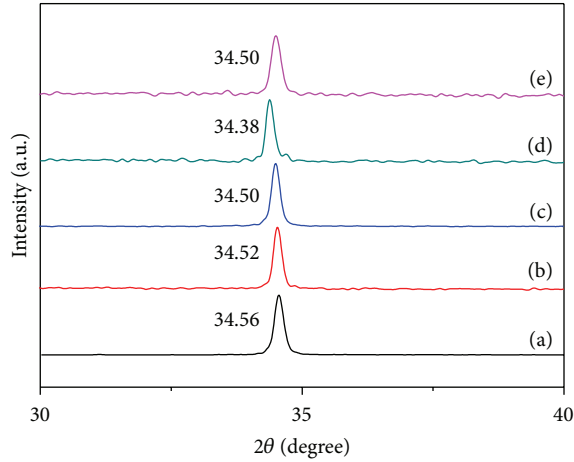


FIGURE 1: XRD patterns of the samples with $n_{\text{Na}}/n_{\text{Zn}}$ of (a) 0, (b) 2.8, (c) 5.6, (d) 8.4, and (e) 11.2.

solution was then spin-coated at 500 rpm for 15 s and then at 5000 rpm for 60 s, followed by drying at 120°C for 15 min. The procedure from coating to drying was repeated five times before the substrates were placed into a 360°C tube furnace in air for 20 min to form ZnO seed layer, evaporate the solvent, and remove any organic residue. Subsequently, ZnO nanorod arrays were grown directly by placing the substrate at the bottom of the beaker in 20 mL of aqueous solution of 12.5 mM $\text{Zn}(\text{AC})_2 \cdot 2\text{H}_2\text{O}$, 12.5 mM hexamethylenetetramine (HMTA, $\text{C}_6\text{H}_{12}\text{N}_4$), and different amounts of NaCl in a 50 mL autoclave. Different Na doping levels were obtained by varying the molar ratio of Na/Zn ($n_{\text{Na}}/n_{\text{Zn}}$) (0, 2.8, 5.6, 8.4, and 11.2) in the precursor solution. Finally the autoclave was sealed and heated at 95°C for 2 h. Subsequently, the samples are washed with deionized water for several times to remove the residual salt and amino complex and dried in a flow of nitrogen gas.

Powder X-ray diffraction (XRD) analyses were performed on a Philips PW-1830 X-ray diffractometer with $\text{Cu K}\alpha$ irradiation ($\lambda = 1.5406 \text{ \AA}$) at a scanning speed of $0.014^\circ/\text{sec}$ over the 2θ range of 30–40°. The electronic morphology of the samples was examined by Hitachi S-4800 scanning electron microscope (SEM). The electrical properties were characterized by a Hall effect measurement system. Photoluminescence and Raman spectra of samples on Si substrate were recorded using Jobin-Yvon Lab-Ram high-resolution spectrometer with He-Cd laser ($\lambda = 325 \text{ nm}$).

3. Results and Discussion

XRD patterns of the hydrothermally grown samples were shown in Figure 1. The strong peak corresponding to ZnO (002) is observed in each film, which indicates high c -axis oriented in all samples. It can be seen that the diffraction peak shows an obvious shift to a smaller angle of about 34.56, 34.52, 34.50, 34.38, and 34.52 for the sample with $n_{\text{Na}}/n_{\text{Zn}}$ of 0, 2.8, 5.6, 8.4, and 11.2, respectively. This demonstrates that Na doping increases the lattice constant as a result of larger

TABLE 1: Electrical properties of ZnO films at room temperature.

$n_{\text{Na}}/n_{\text{Zn}}$	Carrier type	Mobility ($\text{cm}^2 \text{ v}^{-1} \text{ s}^{-1}$)	Carrier concentration (cm^{-3})
0	n	40	1.4×10^{16}
2.8	p	106	3.1×10^{16}
5.6	p	41.9	1.7×10^{17}
8.4	p	99.4	6.5×10^{16}
11.2	n	10.4	4.3×10^{16}

TABLE 2: Electrical properties of Na-doped ZnO films by different processes.

Material	Mobility ($\text{cm}^2 \text{ v}^{-1} \text{ s}^{-1}$)	Carrier concentration (cm^{-3})	References
ZnO:Na	1.41	5.19×10^{16}	[9]
ZnO:Na	0.138–0.676	6.90×10^{16} – 2.16×10^{17}	[21]
ZnO:Na	0.22	5.3×10^{16}	[22]
ZnO:Na	0.43	2.5×10^{17}	[23]
ZnO:Na	0.402	1.81×10^{15}	[24]
ZnO:Na nanowires	2.1	1.3×10^{16}	[7]
ZnO:Na nanorod arrays	41.9–106	3.1×10^{16} – 1.7×10^{17}	Our work

ionic radius of Na^+ (0.089 nm) compared with that of Zn^{2+} (0.070 nm) [8].

Figure 2 shows the surface morphologies of samples grown by simple aqueous solution approach on Si substrates. The nanorods are vertically well-aligned on the substrate surface. The diameter and length of pure ZnO are in the range of around 30 nm and 754 nm, respectively. Figure 3 shows a plot of diameter and length of ZnO nanorod arrays as functions of $n_{\text{Na}}/n_{\text{Zn}}$. With the increase of $n_{\text{Na}}/n_{\text{Zn}}$, the diameter of ZnO nanorod increased to 50 nm, 60 nm, 70 nm, and 70 nm, and the length decreased to 150 nm, 112 nm, 98 nm, and 71 nm, respectively.

Table 1 summarizes the electrical properties of ZnO films. Under Hall effect measurements, the undoped sample showed n-type conductivity, while the doped sample with $n_{\text{Na}}/n_{\text{Zn}}$ of 2.8–8.4 showed p-type conductivity, but when $n_{\text{Na}}/n_{\text{Zn}}$ was increased to 11.2, the film showed n-type conductivity again. In contrast, the electrical properties of samples with $n_{\text{Na}}/n_{\text{Zn}}$ of 2.8–8.4 showed higher mobility and carrier concentration. Mobility was up to $106 \text{ cm}^2 \text{ v}^{-1} \text{ s}^{-1}$ when $n_{\text{Na}}/n_{\text{Zn}}$ was 2.8, and the carrier concentration was $1.7 \times 10^{17} \text{ cm}^{-3}$ when $n_{\text{Na}}/n_{\text{Zn}}$ was 5.6. Mobility and carrier concentration were significantly improved by doping. We think this is due to the right amount of Na ions in the Zn lattice sites acting as acceptors, compensation Zn_i , and V_O intrinsic donor defects in the lattice. Most of the Na^+ occupies the lattice position, and the lattice expansion is small. The above XRD analysis further illustrates the rationality of our analysis. Electrical properties of Na-doped ZnO films by different processes are shown in Table 2. It can be seen that

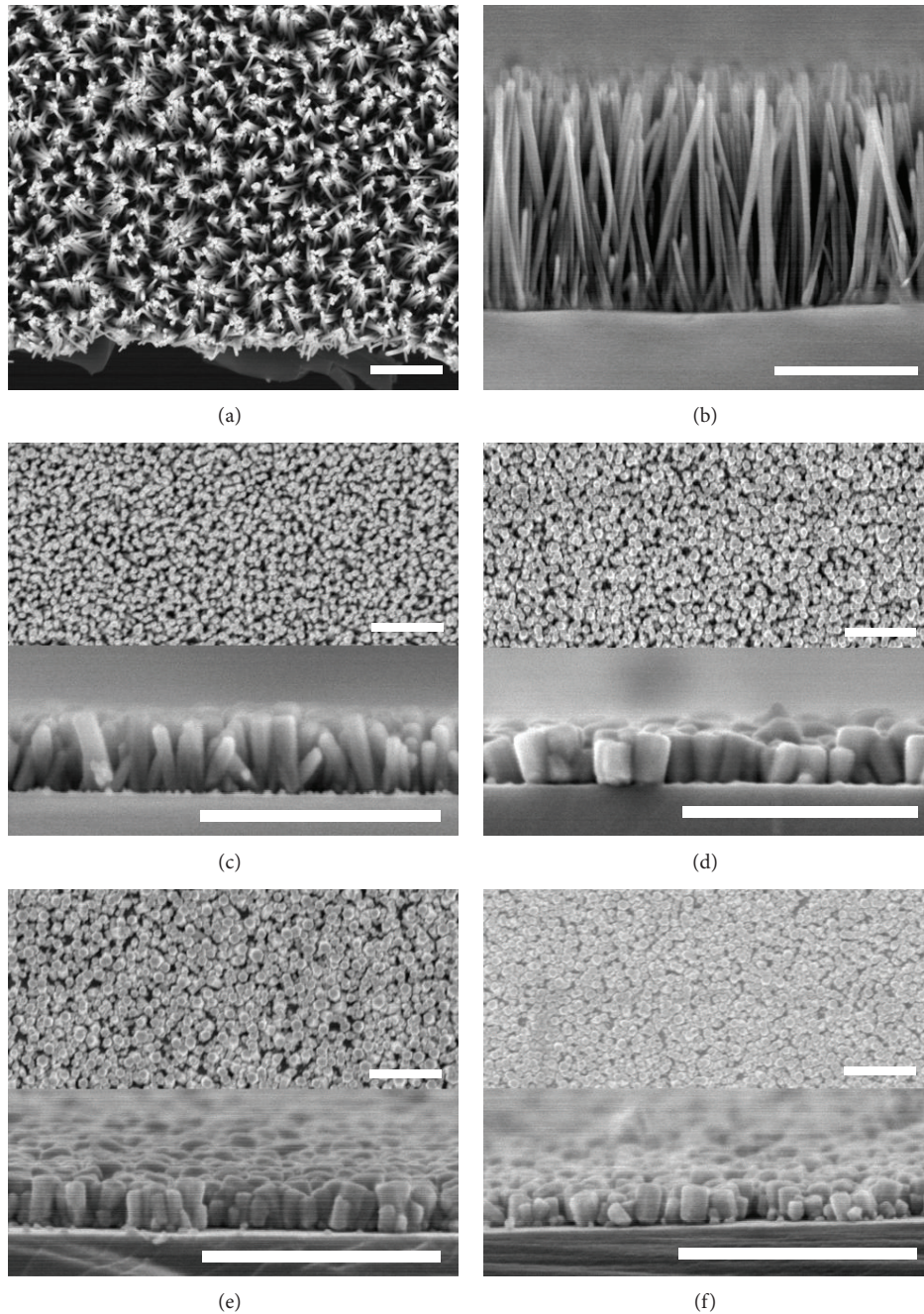


FIGURE 2: SEM images of the samples with $n_{\text{Na}}/n_{\text{Zn}}$ of (a, b) 0, (c) 2.8, (d) 5.6, (e) 8.4, and (f) 11.2. All the scale bars are 500 nm.

Na-doped nanorod arrays in this study showed excellent electrical properties.

Usually, PL spectra of ZnO at room temperature were composed of a near band edge UV emission peak at around 375 nm and a deep level green emission peak at 450–550 nm. Researchers generally believe that the near band edge UV emission peak was caused by the recombination luminescence of the band edge exciton, while the deep level green emission peak was caused by the recombination of the defects such as O vacancy and Zn interstitial. Strong excitonic emission at 375 nm was observed, as shown in Figure 4. The UV emission was so strong, which indicates that all the 1D

ZnO arrays were of high UV emission efficiency and that the green emission could hardly be observed in the PL spectrum, indicating that the crystalline quality of ZnO was high and lattice oxygen vacancy concentration is very low.

Figure 5 shows the doped samples before and after 325 nm excitation of Raman spectra. Raman spectra can be sensitive to detect the crystallization of the material and the defect state. Undoped Al (LO) mode peak at 578.1 cm^{-1} corresponds to the E1 longitudinal optical phonon (LO) mode. When the molar ratio of Na and Zn was 2.8, 5.6, 7.8, and 11.2, the peak position was at 577.3 cm^{-1} , 574.9 cm^{-1} , 574.2 cm^{-1} , and 575.8 cm^{-1} , which moved 0.8 cm^{-1} , 3.2 cm^{-1} , 3.9 cm^{-1} ,

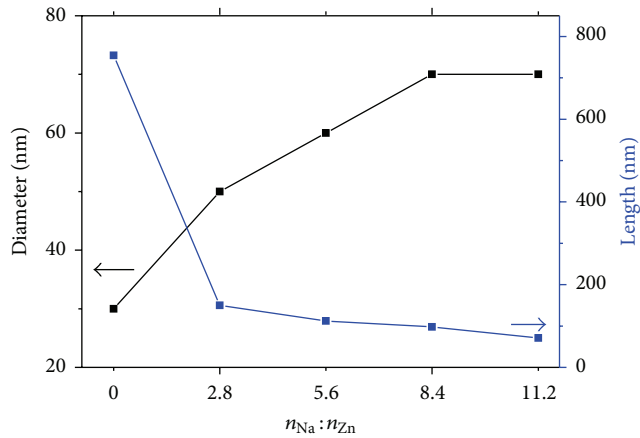


FIGURE 3: Diameter and length of ZnO nanorod arrays as functions of $n_{\text{Na}}/n_{\text{Zn}}$.

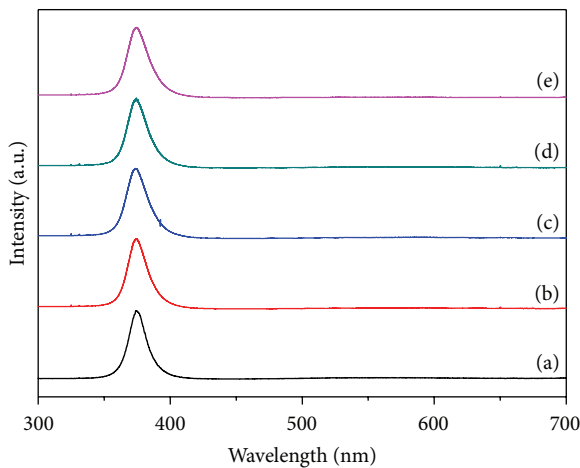


FIGURE 4: PL spectrum of the samples with $n_{\text{Na}}/n_{\text{Zn}}$ of (a) 0, (b) 2.8, (c) 5.6, (d) 8.4, and (e) 11.2.

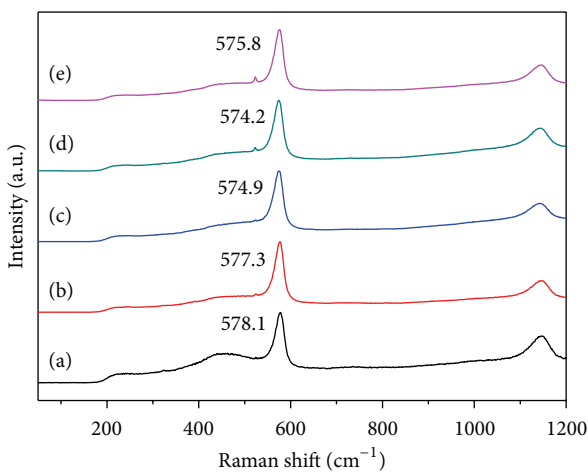


FIGURE 5: Raman spectra of the samples with $n_{\text{Na}}/n_{\text{Zn}}$ of (a) 0, (b) 2.8, (c) 5.6, (d) 8.4, and (e) 11.2.

and 2.3 cm^{-1} , respectively. We observed that the peaks move to lower frequency, because this peak and the oxygen atom

vacancies and zinc atoms interstitial related to its move reflect the changes in the concentration of free carriers in the ZnO crystal. So the concentration of free carriers in the ZnO crystals doped Na changed, and when the doping concentration of Al (LO) peak of the amount of movement is also different, this also shows the degree of change of free carrier concentration to be different.

4. Conclusion

In summary, Na-doped ZnO nanorod arrays with high crystalline quality were successfully fabricated on Si substrate by a simple hydrothermal method for the first time. With the increase of $n_{\text{Na}}/n_{\text{Zn}}$, the diameter of ZnO nanorod gradually increased from 30 nm to 70 nm, and the length decreased from 754 nm to 71 nm. Structural, electrical, and optical properties were investigated. The p-type carrier concentrations and mobility of Na-doped ZnO nanorod arrays arranged from $3.1 \times 10^{16} \text{ cm}^{-3}$ to $1.7 \times 10^{17} \text{ cm}^{-3}$ and $41.9 \text{ cm}^2 \text{ v}^{-1} \text{ s}^{-1}$ to $106 \text{ cm}^2 \text{ v}^{-1} \text{ s}^{-1}$, respectively.

Competing Interests

The authors declare that there are no competing interests regarding the publication of this paper.

Acknowledgments

This study is supported by the National Natural Science Foundation of China (no. 51402252) and the Natural Science Foundation of Jiangsu Province (no. BK20140463).

References

- [1] Y. X. Liu, H. L. Zhang, Z. X. Zhang, Y. Z. Xie, and E. Q. Xie, "Conversion of p-type to n-type conductivity in undoped ZnO films by increasing operating temperature," *Applied Surface Science*, vol. 257, no. 4, pp. 1236–1238, 2010.
- [2] M. Ding, D. X. Zhao, B. Yao, B. H. Li, Z. Zhang, and D. Shen, "The p-type ZnO film realized by a hydrothermal treatment method," *Applied Physics Letters*, vol. 98, no. 6, Article ID 062102, 2011.
- [3] Y. T. Shih, J. F. Chien, M. J. Chen, J. R. Yang, and M. Shiojiri, "P-type ZnO:P films fabricated by atomic layer deposition and thermal processing," *Journal of the Electrochemical Society*, vol. 158, no. 5, pp. H516–H520, 2011.
- [4] V. Vaithianathan, B.-T. Lee, and S. S. Kim, "Preparation of As-doped p-type ZnO films using a Zn_3As_2 ZnO target with pulsed laser deposition," *Applied Physics Letters*, vol. 86, no. 6, Article ID 062101, 2005.
- [5] F. Friedrich, I. Sieber, C. Klimm, M. Klaus, C. Genzel, and N. H. Nickel, "Sb-doping of ZnO: phase segregation and its impact on p-type doping," *Applied Physics Letters*, vol. 98, no. 13, Article ID 131902, 2011.
- [6] Y. J. Zeng, Z. Z. Ye, W. Z. Xu et al., "Dopant source choice for formation of p-type ZnO: Li acceptor," *Applied Physics Letters*, vol. 88, no. 6, Article ID 062107, 2006.
- [7] W. Liu, F. X. Xiu, K. H. Sun et al., "Na-doped p-type ZnO microwires," *Journal of the American Chemical Society*, vol. 132, no. 8, pp. 2498–2499, 2010.

- [8] L. Q. Zhang, Y. Z. Zhang, Z. Z. Ye et al., "The fabrication of Na doped p-type $Zn_{1-x}Mg_xO$ films by pulsed laser deposition," *Applied Physics A: Materials Science and Processing*, vol. 106, no. 1, pp. 191–196, 2012.
- [9] Y. Li, Y. Z. Zhang, H. P. He, Z. Z. Ye, J. Jiang, and L. Cao, "Growth of Na doped p-type non-polar a-plane ZnO films by pulsed laser deposition," *Materials Letters*, vol. 76, pp. 81–83, 2012.
- [10] M. K. Gupta, N. Sinha, and B. Kumar, "p-type K-doped ZnO nanorods for optoelectronic applications," *Journal of Applied Physics*, vol. 109, no. 8, Article ID 083532, 2011.
- [11] M. A. Myers, J. H. Lee, Z. X. Bi, and H. Y. Wang, "High quality p-type Ag-doped ZnO thin films achieved under elevated growth temperatures," *Journal of Physics-Condensed Matter*, vol. 24, no. 22, Article ID 229501, 2012.
- [12] B. Mari, M. Sahal, M. A. Mollar, F. M. Cerqueira, and A. P. Samantilleke, "p-Type behaviour of electrodeposited ZnO:Cu films," *Journal of Solid State Electrochemistry*, vol. 16, no. 6, pp. 2261–2265, 2012.
- [13] C. H. Park, S. B. Zhang, and S.-H. Wei, "Origin of p-type doping difficulty in ZnO: the impurity perspective," *Physical Review B—Condensed Matter and Materials Physics*, vol. 66, no. 7, Article ID 073202, 2002.
- [14] B. Y. Zhang, B. Yao, Y. F. Li et al., "Investigation on the formation mechanism of p-type Li-N dual-doped ZnO," *Applied Physics Letters*, vol. 97, no. 22, Article ID 222101, 2010.
- [15] M. Suja, S. B. Bashar, M. M. Morshed, and J. L. Liu, "Realization of Cu-doped p-type ZnO thin films by molecular beam epitaxy," *ACS Applied Materials & Interfaces*, vol. 7, no. 16, pp. 8894–8899, 2015.
- [16] S. B. Bashar, M. Suja, M. Morshed, F. Gao, and J. Liu, "An Sb-doped p-type ZnO nanowire based random laser diode," *Nanotechnology*, vol. 27, no. 6, Article ID 065204, 2016.
- [17] L. Cao, L. P. Zhu, J. Jiang, Y. Li, Y. Z. Zhang, and Z. Z. Ye, "Preparation and properties of p-type Ag-doped ZnMgO thin films by pulsed laser deposition," *Journal of Alloys and Compounds*, vol. 516, pp. 157–160, 2012.
- [18] X. Fang, J. H. Li, D. Zhao, D. Shen, B. Li, and X. Wang, "Phosphorus-doped p-Type ZnO nanorods and ZnO nanorod p-n homojunction LED fabricated by hydrothermal method," *Journal of Physical Chemistry C*, vol. 113, no. 50, pp. 21208–21212, 2009.
- [19] S. N. Das, J.-H. Choi, J. P. Kar, T. I. Lee, and J.-M. Myoung, "Fabrication of p-type ZnO nanowires based heterojunction diode," *Materials Chemistry and Physics*, vol. 121, no. 3, pp. 472–476, 2010.
- [20] Q. X. Xia, K. S. Hui, K. N. Hui et al., "High quality p-type N-doped AZO nanorod arrays by an ammonia-assisted hydrothermal method," *Materials Letters*, vol. 78, pp. 180–183, 2012.
- [21] Z. Zheng, Y. F. Lu, Z. Z. Ye, H. P. He, and B. H. Zhao, "Carrier type- and concentration-dependent absorption and photoluminescence of ZnO films doped with different Na contents," *Materials Science in Semiconductor Processing*, vol. 16, no. 3, pp. 647–651, 2013.
- [22] X. H. Pan, Y. S. Zhou, S. S. Chen et al., "Effect of Na contents on fabrication of p-type non-polar m-plane ZnO films," *Journal of Crystal Growth*, vol. 404, pp. 54–58, 2014.
- [23] W. Chen, X. H. Pan, S. S. Chen et al., "Investigation on non-polar m-plane ZnO and Na-doped p-type ZnO films grown by plasma-assisted molecular beam epitaxy," *Applied Physics A: Materials Science and Processing*, vol. 121, no. 1, pp. 77–82, 2015.
- [24] P. Ding, X. H. Pan, Z. Z. Ye et al., "Realization of p-type non-polar a-plane ZnO films via doping of Na acceptor," *Solid State Communications*, vol. 156, pp. 8–11, 2013.

Research Article

Multishelled NiO Hollow Spheres Decorated by Graphene Nanosheets as Anodes for Lithium-Ion Batteries with Improved Reversible Capacity and Cycling Stability

Lihua Chu,¹ Meicheng Li,^{1,2} Yu Wang,¹ Xiaodan Li,¹ Zipei Wan,¹ Shangyi Dou,¹ and Yue Chu¹

¹State Key Laboratory of Alternate Electrical Power System with Renewable Energy Sources, North China Electric Power University, Beijing 102206, China

²Chongqing Materials Research Institute, Chongqing 400707, China

Correspondence should be addressed to Meicheng Li; mcli@ncepu.edu.cn

Received 15 December 2015; Revised 16 January 2016; Accepted 21 April 2016

Academic Editor: Raul Arenal

Copyright © 2016 Lihua Chu et al. This is an open access article distributed under the Creative Commons Attribution License, which permits unrestricted use, distribution, and reproduction in any medium, provided the original work is properly cited.

Graphene-based nanocomposites attract many attentions because of holding promise for many applications. In this work, multishelled NiO hollow spheres decorated by graphene nanosheets nanocomposite are successfully fabricated. The multishelled NiO microspheres are uniformly distributed on the surface of graphene, which is helpful for preventing aggregation of as-reduced graphene sheets. Furthermore, the NiO/graphene nanocomposite shows much higher electrochemical performance with a reversible capacity of 261.5 mAh g⁻¹ at a current density of 200 mA g⁻¹ after 100 cycles tripled compared with that of pristine multishelled NiO hollow spheres, implying the potential application in modern science and technology.

1. Introduction

With the rapid development of the global economy, fast depletion of nonrenewable energy, and the increasing environmental problems, it is urgent to develop new clean and sustainable sources and technologies for energy storage and conversion with high efficiency [1–3]. Rechargeable lithium-ion batteries (LIBs) are a promising one for the upcoming demand such as electric vehicles and grid storage systems because of their high energy density, long lifespan, and environmental benignancy.

As one of the special structures of carbon, graphene has initiated enormous scientific activities, with the honeycomb lattice structure, unique structural features of chemical stability, high surface area, flexibility, and superior electric and thermal conductivity. It has been used as ideal building blocks for energy storage systems with improved electrochemical properties compared with these host materials, such as metal, metal oxide, and sulfide [4, 5]. To further explore the potential application of graphene-based nanomaterials, deriving from

the decoration of graphene nanosheets (GNS) with nanomaterials attracts more and more interest. So far, several graphene-based nanocomposites have been successfully fabricated and show desirable combinations of properties that are not found in individual components [6, 7].

Nickel oxide (NiO) is one of prospective anode materials in li-ion battery (LIB), which possesses the advantages of high theoretical capacity (717 mAh g⁻¹), high natural abundance, nontoxicity, low cost, and environmental benignity [8–11]. However, the practical utilization of NiO is still limited owing to its poor cycling and rate performances of the NiO-based LIBs. Several strategies have been undertaken to enhance the performance of NiO electrode materials. One well-established method is constructing hybrid with GNS. Various structures of NiO/GNS, such as porous NiO-wrapped GNS [12], 3D-hierarchical NiO/GNS [13], and graphene anchored with nickel nanoparticles [14], have been prepared, revealing that the NiO/GNS nanocomposite reinforces the properties of pristine NiO which favors their wide application in LIBs.

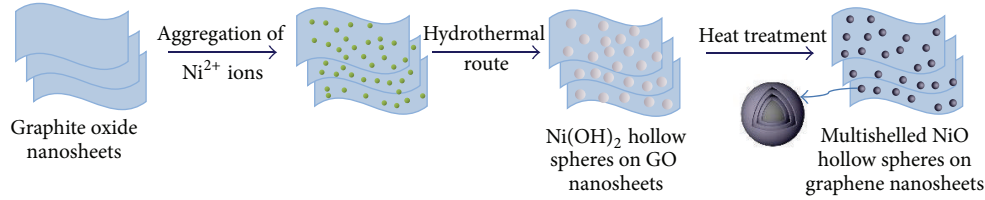


FIGURE 1: Illustration of the procedures for preparation of NiO/graphene hierarchical structure.

In this work, we report the solvothermal method for the synthesis of multishelled NiO hollow spheres/GNS nanocomposite, in which the multishelled NiO hollow spheres are wrapped by GNS. This hybrid architecture is found to display much improved electrochemical properties by comparison to that of pristine multishelled NiO hollow microspheres.

2. Experimental

The composite was prepared by the solvothermal method. 3 mL graphite oxide (6 mol L^{-1}) was ultrasonically dispersed in 30 mL of deionized water and then 1 g of $\text{Ni}(\text{NO})_3 \cdot 6\text{H}_2\text{O}$ and 1 g of D-glucose were added, adjusting the pH to 10.90 with $\text{NH}_3 \cdot \text{H}_2\text{O}$, using a pH meter and magnetic stirrer to form a homogeneous solution at room temperature. The solution was then transferred into a Teflon-lined stainless steel autoclave (50 mL), sealed, and heated at 150°C for 15 h. The product was collected by centrifugation, washed with deionized water several times to remove impurity, and then dried at 60°C in vacuum. Finally, the NiO/graphene was obtained by calcining the precursor in N_2 at 300°C for 2 h and then in air at 500°C for 2 h. For comparison, the multishelled NiO spheres were prepared by a similar solution-based method and subsequent calcination with the absence of graphene oxide (GO).

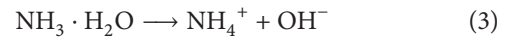
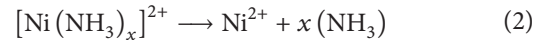
The crystallographic structures, morphology, and microstructure of the as-prepared products were characterized by Bruker D8 Focus X-ray powder diffractometer with using $\text{Cu K}\alpha$ ($\lambda = 1.5406 \text{ \AA}$) radiation over a range of 2θ from 20° to 90° , FEI Quanta 200F microscope field emission scanning electron microscope (FESEM), and Tecnai G2 F20 Field emission transmission electron microscopy (TEM) with accelerating voltage of 200 kV. Raman measurements were recorded on Laser Confocal Micro-Raman Spectroscopy (LabRAM Aramis).

Electrochemical measurements were conducted using a CR-2032-coin type cell configuration. The electrode materials are a slurry consisting of 80 wt% of electrode materials, 10 wt% of acetylene black (Super-P), and 10 wt% of polyvinylidene fluoride (PVDF) dissolved in N-methyl-2-pyrrolidinone. They were coated onto a copper foil and dried at 100°C in vacuum for 12 h before pressing. Lithium foil was used as the counter and reference electrodes and the polypropylene foil (Celgard 2400) was used as the separator. The electrolyte was 1 M LiPF_6 dissolved in a mixture of ethylene carbonate (EC) and dimethyl carbonate (DMC) (v/v = 1:1). Galvanostatic discharge-charge (GDC) experiments were carried out at different current densities in the voltage

range of 0.01–3.00 V with a multichannel battery tester (Maccor, Inc., USA). Cycling and rate performances were measured by the electrochemical workstation (LAND battery test system).

3. Results and Discussion

A schematic illustration of the fabrication process of NiO/graphene composite is shown in Figure 1. Graphite oxide (GO) was sonicated in di-water to form a homogeneous suspension. Then, the GO nanosheets absorb Ni^{2+} ions, which react with OH^- to grow $\text{Ni}(\text{OH})_2$ architectures on GO nanosheets. Here, OH^- were released by $\text{NH}_3 \cdot \text{H}_2\text{O}$, which can also control the morphology of the $\text{Ni}(\text{OH})_2$ architectures. The formation of $\text{Ni}(\text{OH})_2$ from Ni^{2+} ions and $\text{NH}_3 \cdot \text{H}_2\text{O}$ can be expressed by the following reactions:



During the calcination, $\text{Ni}(\text{OH})_2$ decomposed to yield multishelled NiO hollow spheres following $\text{Ni}(\text{OH})_2 \rightarrow \text{NiO} + \text{H}_2\text{O}$, and GO nanosheets reduced to graphene by losing oxygen-containing surface groups [15, 16]. So the $\text{Ni}(\text{OH})_2/\text{GO}$ precursor converted to NiO/GNS composites after annealing. The pristine multishelled NiO hollow spheres would be obtained without GO during the similar reaction process, which were discussed in our previous paper [17].

The XRD patterns of NiO and NiO/GNS composite are shown in Figure 2(a). All of the diffraction peaks of pure NiO sample can be ascribed to face centered cubic NiO (JCPDS number 071-1179), which correspond to (111), (200), (220), (311), and (222) planes, respectively. All the characteristic peaks of pure NiO are also observed for NiO/GNS composite. (002) diffraction peak of GNS is typically located at about 24° in the XRD pattern, but it is not obvious in Figure 2(a). Because the content of graphene is low and the diffraction of disorderedly stacked GNS is quite weaker as compared to the well-crystalline NiO, the presence of graphene can be confirmed in the Raman spectra of NiO/GNS, as shown in Figure 2(b), where the G characteristic peaks of graphene are obvious, though the D peak located at $\sim 1350 \text{ cm}^{-1}$ is invisible.

The morphology of pristine NiO and NiO/GNS composite is compared by SEM and TEM. Pure NiO is composed of

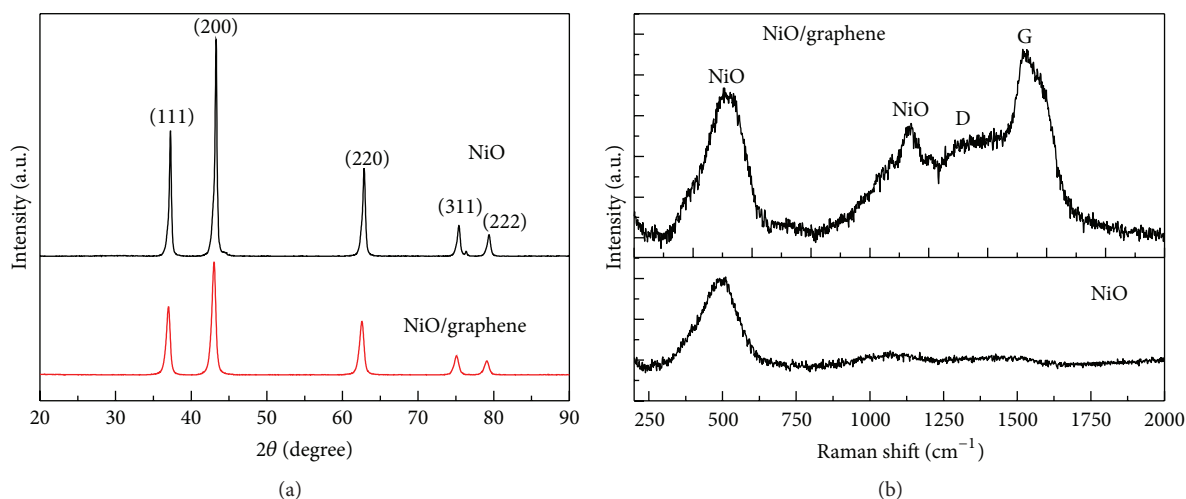


FIGURE 2: (a) X-ray diffraction patterns and (b) Raman spectra for pristine NiO and NiO/graphene composite.

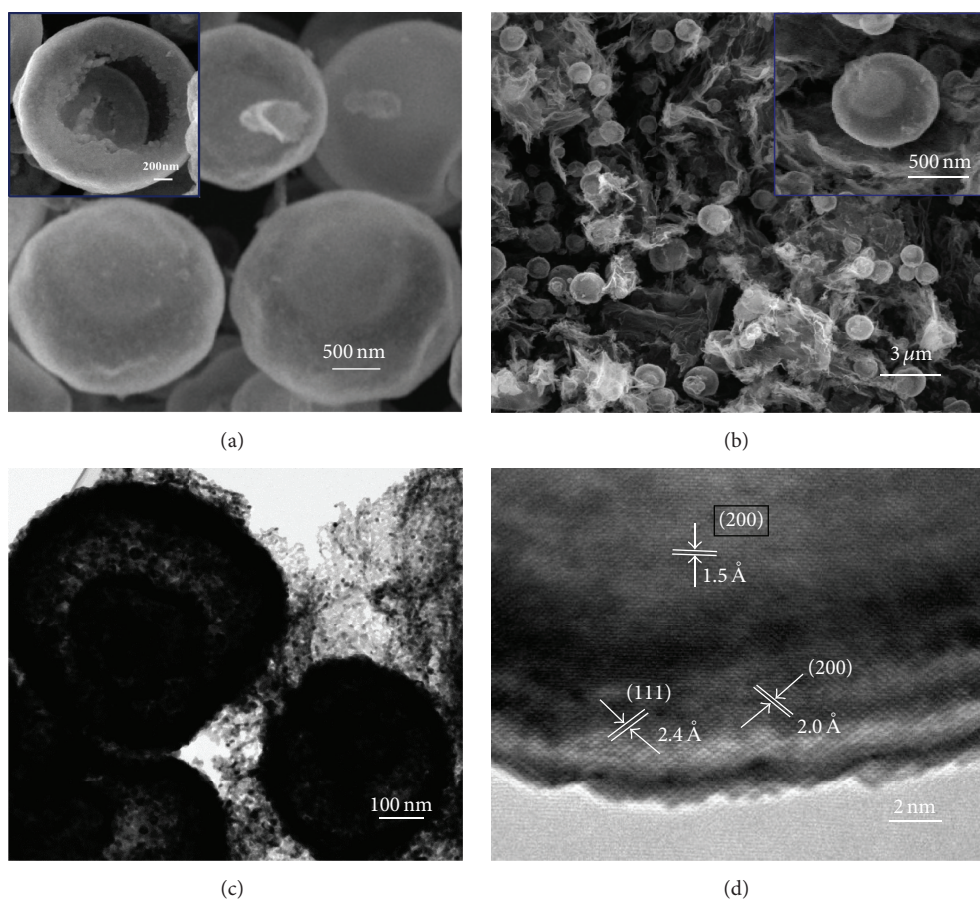


FIGURE 3: SEM images of pristine multishelled NiO spheres (a), NiO/graphene (b), TEM images of NiO/graphene (c), and HRTEM pattern of multishelled NiO spheres (d).

multishelled spheres as shown in Figure 3(a). The NiO/GNS are composed of typical rippled and crumpled GNS and multishelled NiO spheres (Figure 3(b)). It can be clearly seen that the multishelled NiO microspheres with diameter varying from 2.0 μm to 3.5 μm are uniformly distributed on

the surface of GNS. The hybrid architecture can effectively prevent the agglomeration of as-reduced GNS. The inset of Figure 3(b) is the multishelled NiO sphere on the GNS which demonstrates that the multishelled NiO spheres do not change after the addition of graphene. Figure 3(c) shows

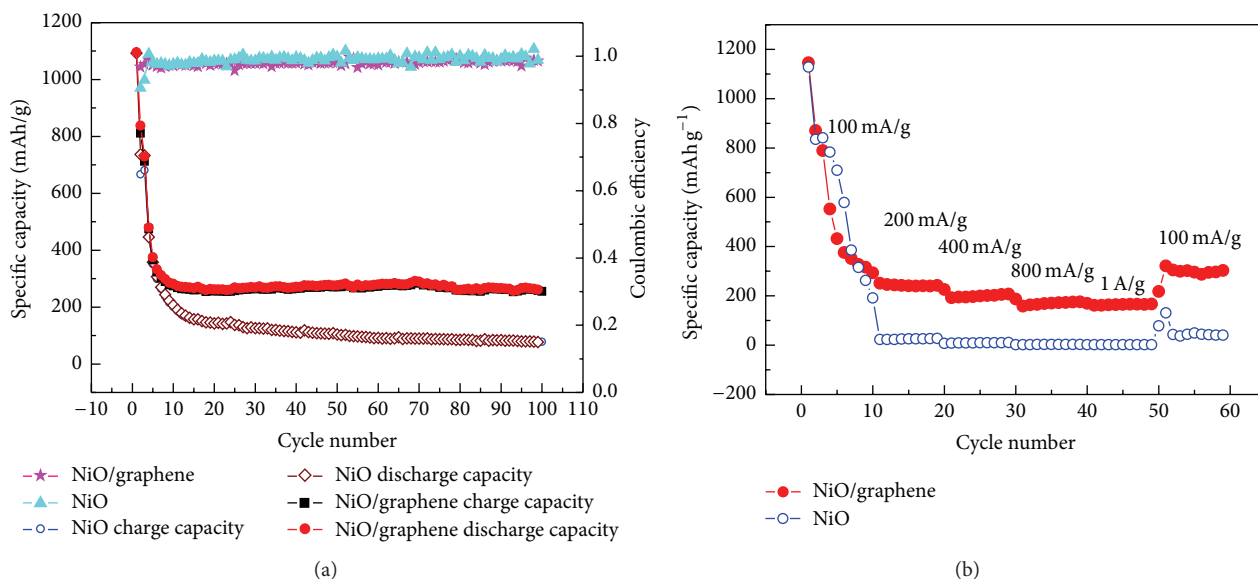


FIGURE 4: (a) Capacity retention and Coulombic efficiency at a current density of 200 mA g^{-1} . (b) Rate performance at various current densities between 100 mA g^{-1} and 1 A g^{-1} .

the TEM image of NiO/GNS which further confirms the multishelled sphere feature of NiO. The HRTEM pattern of multishelled NiO sphere is presented in Figure 3(d). The lattice spacing of 0.15, 0.2, and 0.24 nm is observed, corresponding to the interspaces of (220), (200) and (111), and (200) planes of cubic NiO.

The electrochemical properties of NiO/GNS composite were evaluated as anode for lithium-ion batteries (LIBs). Figure 4 displays the cycling and rate performances of NiO/GNS composite and pristine NiO. The initial discharge capacities are $\sim 1100 \text{ mAh g}^{-1}$ as shown in Figure 4(a). It is much higher than the theoretical value (718 mAh g^{-1}), mainly attributed to the solid electrolyte interphase (SEI) film formation, and the additional Li^+ storage in the space between NiO spheres and GNS. The reversible capacity of NiO spheres decreases to 77.1 mAh g^{-1} after 100 cycles. While the reversible capacity of NiO/GNS composite still can retain 261.5 mAh g^{-1} after 100 cycles, which is more than three times of pristine NiO sphere. The coulombic efficiencies increase to and almost keep stable in the scale of 98-99% at successive cycles, indicating that the formed SEI film is favorable and stable [18]. The enhanced cycling performance of NiO/GNS composite should be ascribed to the addition of graphene and the hybrid architecture. Firstly, the GNS have much better conductivity due to the wider layer spacing compared with NiO. The d -spacing of GNS was found to be 0.365 nm, and the maximum d -spacing of NiO is 0.24 nm ((111) lattice plane) [19]. Therefore, the GNS can offer additional sites for accommodation of Li^+ leading to the enhanced reversible capacity. Secondly, the flexible GNS can accommodate the volume change and prevent the aggregation of active materials upon cycling. Thirdly, the hybrid architecture can also be helpful for preventing aggregating or restacking of as-reduced GNS.

Moreover, the NiO/GNS composites also exhibit enhanced rate capacity compared with pristine NiO spheres, as presented in Figure 4(b). The discharge capacities of NiO/GNS at 100 mA g^{-1} , 200 mA g^{-1} , 400 mA g^{-1} , 800 mA g^{-1} , and 1 A g^{-1} are 292.3 mAh g^{-1} (10th cycle), 225.9 mAh g^{-1} (20th cycle), 187.3 mAh g^{-1} (30th cycle), 169.3 mAh g^{-1} (40th cycle), and 166.5 mAh g^{-1} (50th cycle), respectively. In the initial 10 cycles with a small current density (100 mA g^{-1}), the capacities of pristine NiO and NiO/GNS composite are comparable, and the pristine NiO is even a little better than NiO/GNS composite, which may be caused by the lower capacity of graphene as compared to NiO [18]. However, the situation reverses when the current density increases. The enhanced rate capacity could be reasonably attributed to advantageous combination of the highly conductive GNS and the favorable multishelled NiO hollow spheres architecture with large specific surface area and open inner cavity, which can facilitate the rapid diffusion of lithium ions from electrolyte to active material.

As shown in Figure 4(b), the capacity dropped dramatically from $\sim 1100 \text{ mAh g}^{-1}$ to a little more than 300 mAh g^{-1} during the first five cycles with a small current density (100 mA g^{-1}). Generally, the capacity lost in the first several cycles can be attributed to the irreversible reactions involved in the formation of the SEI layer. In addition, the formation and stabilization of the SEI layer are a gradual process, so that stable capacity also requires a process, which has been described in many works [20, 21]. It is also probably caused by large theoretical capacity difference between NiO (717 mAh g^{-1}) and graphene (372 mAh g^{-1}). During the first several cycles, the synergy effect between NiO and graphene does not play well during the lithiation and delithiation process; therefore, the NiO and graphene do not serve well in

terms of improving and stabilizing capacity. So the dropped capacity is due to the formation of SEI layer and the capacity difference in the first several cycles.

The NiO/GNS composite demonstrates improved electrochemical performance, which could be due to several reasons. Firstly, the wider GNS can offer additional sites for the accommodation of Li^+ compared with NiO. Moreover, the well-contact GNS and multishelled NiO hollow spheres can facilitate the continuous and rapid conducting pass way of Li^+ , which are beneficial for enhancing specific capacity and rate performance of the active materials. Secondly, GNS are anticipated to prevent the collapse and aggregation of the active materials upon cycling, which brings about excellent cycling stability. Vice versa, the hybrid architecture can also be helpful for preventing aggregating of GNS [12]. Thirdly, the large specific surface area and open inner cavity of GNS and the favorable multishelled NiO hollow spheres architecture can provide sufficient electrode/electrolyte contact areas and facilitate the continuous and rapid electron transport through the electrodes, resulting in the improved rate performance.

4. Conclusions

In summary, we have successfully fabricated NiO/GNS composite, in which the multishelled NiO microspheres are uniformly distributed on the surface of GNS. The composite shows much enhanced cycling stability and capacity compared with the pristine multishelled NiO hollow spheres, when evaluated as the anode materials in LIBs. The superior performance in LIBs originates from the addition of GNS and the sandwich-like architecture, which can facilitate the continuous and rapid electron transport and prevent the collapse of nanostructures and aggregation of the active materials. The strategies described here could offer an effective method to improve the electrochemical performance of other electrode materials with large volume changes and low electrical conductivities.

Competing Interests

The authors declare that they have no competing interests.

Acknowledgments

This work is supported partially by National High-tech R&D Program of China (863 Program, no. 2015AA034601), National Natural Science Foundation of China (Grant nos. 91333122, 51402106, 51372082, 51172069, 61204064, and 51202067), Ph.D. Programs Foundation of Ministry of Education of China (Grant nos. 20120036120006 and 20130036110012), Par-Eu Scholars Program, and the Fundamental Research Funds for the Central Universities.

References

- [1] H. Xia, C. Hong, X. Shi et al., "Hierarchical heterostructures of Ag nanoparticles decorated MnO_2 nanowires as promising electrodes for supercapacitors," *Journal of Materials Chemistry A*, vol. 3, no. 3, pp. 1216–1221, 2015.
- [2] H. Xia, C. Hong, B. Li et al., "Facile synthesis of hematite quantum dot/functionalized graphene-sheet composites as advanced anode materials for asymmetric supercapacitors," *Advanced Functional Materials*, vol. 25, no. 4, pp. 627–635, 2015.
- [3] H. Xia, D. Zhu, Z. Luo et al., "Hierarchically structured Co_3O_4 @Pt@ MnO_2 nanowire arrays for high-performance supercapacitors," *Scientific Reports*, vol. 3, article 2978, 2013.
- [4] J. Zhu, D. Yang, Z. Yin, Q. Yan, and H. Zhang, "Graphene and graphene-based materials for energy storage applications," *Small*, vol. 10, no. 17, pp. 3480–3498, 2014.
- [5] M. Pumera, "Graphene-based nanomaterials for energy storage," *Energy and Environmental Science*, vol. 4, no. 3, pp. 668–674, 2011.
- [6] C. Zhang, X. Peng, Z. Guo et al., "Carbon-coated SnO_2 /graphene nanosheets as highly reversible anode materials for lithium ion batteries," *Carbon*, vol. 50, no. 5, pp. 1897–1903, 2012.
- [7] D.-H. Lee, J.-C. Kim, H.-W. Shim, and D.-W. Kim, "Highly reversible Li storage in hybrid NiO/Ni/graphene nanocomposites prepared by an electrical wire explosion process," *ACS Applied Materials & Interfaces*, vol. 6, no. 1, pp. 137–142, 2014.
- [8] N. S. Spinner, A. Palmieri, N. Beauregard, L. Zhang, J. Campanella, and W. E. Mustain, "Influence of conductivity on the capacity retention of NiO anodes in Li-ion batteries," *Journal of Power Sources*, vol. 276, pp. 46–53, 2015.
- [9] X. Yan, X. Tong, J. Wang, C. Gong, M. Zhang, and L. Liang, "Synthesis of hollow nickel oxide nanotubes by electrospinning with structurally enhanced lithium storage properties," *Materials Letters*, vol. 136, pp. 74–77, 2014.
- [10] W. Sun, X. Rui, J. Zhu et al., "Ultrathin nickel oxide nanosheets for enhanced sodium and lithium storage," *Journal of Power Sources*, vol. 274, pp. 755–761, 2015.
- [11] D. Mao, J. Yao, X. Lai, M. Yang, J. Du, and D. Wang, "Hierarchically mesoporous hematite microspheres and their enhanced formaldehyde-sensing properties," *Small*, vol. 7, no. 5, pp. 578–582, 2011.
- [12] D. Xie, Q. Su, W. Yuan, Z. Dong, J. Zhang, and G. Du, "Synthesis of porous NiO-wrapped graphene nanosheets and their improved lithium storage properties," *Journal of Physical Chemistry C*, vol. 117, no. 46, pp. 24121–24128, 2013.
- [13] L. Tao, J. Zai, K. Wang et al., "3D-hierarchical NiO-graphene nanosheet composites as anodes for lithium ion batteries with improved reversible capacity and cycle stability," *RSC Advances*, vol. 2, no. 8, pp. 3410–3415, 2012.
- [14] Y. J. Mai, J. P. Tu, C. D. Gu, and X. L. Wang, "Graphene anchored with nickel nanoparticles as a high-performance anode material for lithium ion batteries," *Journal of Power Sources*, vol. 209, pp. 1–6, 2012.
- [15] H. Li, L. Pan, C. Nie, Y. Liu, and Z. Sun, "Reduced graphene oxide and activated carbon composites for capacitive deionization," *Journal of Materials Chemistry*, vol. 22, no. 31, pp. 15556–15561, 2012.
- [16] I. R. M. Kottegoda, N. H. Idris, L. Lu, J.-Z. Wang, and H.-K. Liu, "Synthesis and characterization of graphene-nickel oxide nanostructures for fast charge-discharge application," *Electrochimica Acta*, vol. 56, no. 16, pp. 5815–5822, 2011.
- [17] L. Chu, M. Li, Z. Wan et al., "Morphology control and fabrication of multi-shelled NiO spheres by tuning the pH value via a hydrothermal process," *CrystEngComm*, vol. 16, no. 48, pp. 11096–11101, 2014.
- [18] Y. Huang, X.-L. Huang, J.-S. Lian, D. Xu, L.-M. Wang, and X.-B. Zhang, "Self-assembly of ultrathin porous NiO

- nanosheets/graphene hierarchical structure for high-capacity and high-rate lithium storage,” *Journal of Materials Chemistry*, vol. 22, no. 7, pp. 2844–2847, 2012.
- [19] E. J. Yoo, J. Kim, E. Hosono, H.-S. Zhou, T. Kudo, and I. Honma, “Large reversible Li storage of graphene nanosheet families for use in rechargeable lithium ion batteries,” *Nano Letters*, vol. 8, no. 8, pp. 2277–2282, 2008.
- [20] X. Huang, H. Yu, J. Chen, Z. Lu, R. Yazami, and H. H. Hng, “Ultrahigh rate capabilities of lithium-ion batteries from 3D ordered hierarchically porous electrodes with entrapped active nanoparticles configuration,” *Advanced Materials*, vol. 26, no. 8, pp. 1296–1303, 2014.
- [21] K. Cao, L. Jiao, H. Liu et al., “3D hierarchical porous α - Fe_2O_3 nanosheets for high-performance lithium-ion batteries,” *Advanced Energy Materials*, vol. 5, no. 4, Article ID 1401421, 2015.

Research Article

Lanthanide Coordination Polymer Nanosheet Aggregates: Solvothermal Synthesis and Downconversion Luminescence

Rui-Rui Su,¹ Peng Tao,¹ Yi Han,² Cheng-Hui Zeng,¹ and Sheng-Liang Zhong¹

¹Key Laboratory of Functional Small Organic Molecule, Ministry of Education and Jiangxi's Key Laboratory of Green Chemistry, College of Chemistry and Chemical Engineering, Jiangxi Normal University, Nanchang 330022, China

²School of Chemistry and Chemical Engineering, Sun Yat-Sen University, Guangzhou 510275, China

Correspondence should be addressed to Cheng-Hui Zeng; chenghuizeng@qq.com and Sheng-Liang Zhong; slzhong@jxnu.edu.cn

Received 23 February 2016; Accepted 10 April 2016

Academic Editor: Margarida Amaral

Copyright © 2016 Rui-Rui Su et al. This is an open access article distributed under the Creative Commons Attribution License, which permits unrestricted use, distribution, and reproduction in any medium, provided the original work is properly cited.

A lanthanide coordination polymers (CPs) nanostructure (**1**) has been synthesized via a facile template-free solvothermal strategy using DMF as solvent and 2-methyl benzoic acid (2-MeBAH) as ligands. The products are characterized by powder X-ray diffraction (PXRD), scanning electron microscopy (SEM), elemental analyses (EA), and downward luminescence. Product **1** built from Tb³⁺ and 2-MeBAH has one-dimensional structure which is connected by trinuclear second building units (SBUs). Downward luminescence shows that sample **1** exhibits characteristic transitions of the Tb³⁺ ion at 489, 544, 583, and 621 nm, and the strongest peak is at 544 nm ascribed to the transition of ⁵D₄ → ⁷F₅ of Tb³⁺.

1. Introduction

Lanthanide coordination polymer (CP) is an important class of organic-inorganic hybrid materials formed by the coordination of lanthanide ions with organic linkers. They have shown a number of promising applications; these applications are ascribed to the best properties of organic and inorganic components and decrease their drawbacks by a synergic effect [1]. In order to get functional lanthanide materials, appropriate synthetic strategies are critical [2, 3]. Compared with first-row transition metal ions, lanthanide ions usually display high coordination number and variable coordination geometries, and they will make lanthanide ions become excellent spacers in assembling fascinating coordination polymers [4]. As a subset of such materials, lanthanide CPs continue to attract an escalating attention, owing to their unique optical, electronic, and magnetic properties [5–7]. In addition, nanosheet materials have been of continuous research interests in material science, because of their unique properties in the areas of catalysis, drug delivery, and biosensors. Herein, our group has successfully prepared terbium-based CP nanosheet aggregates, with downward green-light emission while excited by violet light.

In modern chemistry and materials science, synthesis of uniform nanosheet materials with controllable size and well-defined morphologies remains a research focus due to their superior properties of large specific area, low effective density, and good permeation [8]. Thereby, hollow spherical materials constructed by the nanosheet possess widespread potential applications in various fields, including catalysts, adsorbents, photonic devices, sensors, drug-delivery carriers, disease diagnosis agents, waste removal, and chemical reactors [9]. In recent years, a variety of synthetic routes have been developed for the preparation of hollow spheres [10, 11] such as solvothermal method, hydrothermal method, precipitation method, spray pyrolysis method, and template-assisted method. Generally, the solvothermal method is used widely, because the solvent controlling effect is versatile.

As well known, lanthanide coordination polymers have been widely applied in luminescent devices [12, 13]. However, compared with other morphologies of sphere, nanorod, and nanotube, the nanosheet of rare earth coordination polymers which are constructed into aggregates of hollow spheres morphologies has received much attention. Apart from possessing a collection of advantages, such as low weight and saving materials and costs, hollow sphere optical materials

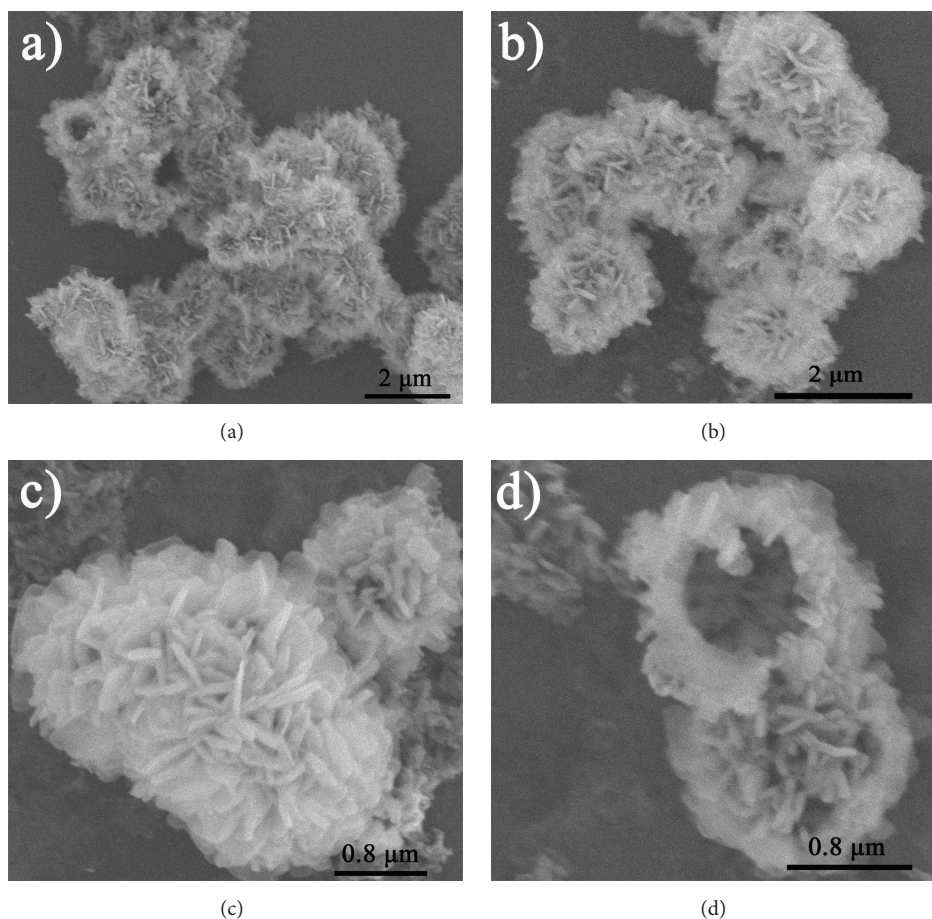


FIGURE 1: SEM images of sample 1.

also display better luminescent properties than other solid materials.

So far, there have been many researches of organic hollow sphere structures fabrication reported. However, there have been few inorganic nanostructures constructed by the nanosheet [8]. In this paper, we report a general one-pot low-cost solvothermal method for preparation of Tb^{3+} -based CP nanosheet and construction into aggregates of hollow microspheres (**1**), using Tb^{3+} as metal center and 2-methyl benzoic acid (2-MeBAH) as ligand. The formation of nanosheet and spherical hollow structures is unusual since no templates or surfactant is intentionally used during the synthetic process. The downward luminescence of **1** was investigated in detail.

2. Experimental Section

Tb_4O_7 was bought from Ganzhou Kemingrui Rare Earth Company (Ganzhou, China). 2-MeBAH was purchased from Aladdin Company (Shanghai, China) and used as received. $TbCl_3 \cdot 6H_2O$ was prepared by dissolving Tb_4O_7 (99.9%) with concentrated HCl_3 and then evaporated at $100^\circ C$ until the crystal film formed. Other reagents were from Guangzhou Chemical Reagent Factory (AR, Guangzhou, China) and used without further purification.

In a typical process, Tb^{3+} -based CP nanosheet and its aggregates of hollow microspheres were prepared as follows: an aqueous solution of 2-MeBAH (0.1 g in 25 mL) was added with a 0.1 M NaOH solution to adjust the ligand solution at $pH = 6$, in a stoichiometric amount to yield the sodium salt in situ. The resulting solution was added dropwise to a 10 mL 0.1 g $TbCl_3$ DMF solution ($100^\circ C$). All the ligand solution was added to the salt solution in an hour and resulted in a white precipitate. The solid was separated by centrifugation, then washed with water and ethanol, and dried in vacuum desiccator for several days.

Powder X-ray diffraction (PXRD) was carried out using a Rigaku X-ray diffractometer with $Cu-K\alpha$ radiation ($\lambda = 1.54178 \text{ \AA}$). Scanning electron microscopy (SEM) was performed on a Hitachi S-3400. Elemental analysis (EA, C and H) was performed on an EA3000 elemental analyzer. Downconversion luminescence spectrum was recorded on an FLS 980 (Edinburgh Instruments, UK) at room temperature.

3. Results and Discussion

SEM was utilized to characterize the morphology and structure of as-prepared samples. As presented in Figure 1(a), it can be seen that sample **1** consists of well aggregated

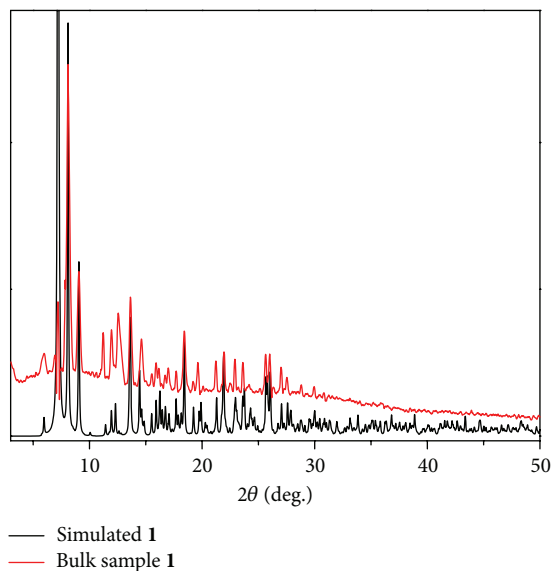


FIGURE 2: PXRD of simulated and bulk sample **1**.

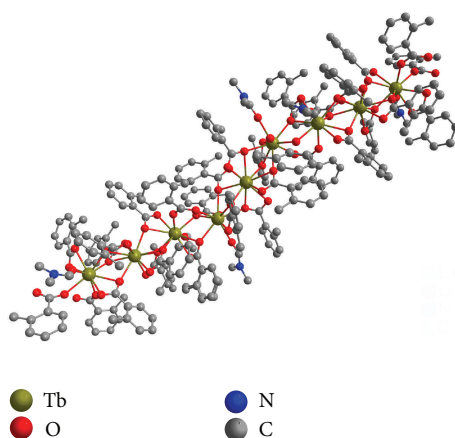


FIGURE 3: The 1D structure of **1** constructed by trinuclear SBUs.

nanosheet, and the aggregated nanosheet forms uniform ball-like structure (Figure 1(b)). Enlargement of the ball-like structure shows that the aggregate units of nanosheets are uniform, with a smooth surface and a narrow size distribution in 50–70 nm (Figure 1(c)).

PXRD of bulk sample **1** in Figure 2 shows evident diffraction peaks, which means that **1** is a crystalline material. Further investigation found that the diffraction peaks compete well with the data (CCDC: 634372) reported by Buskamp et al. [14]. The reported result is a lanthanum complex, and in our result, **1** may be a terbium complex; this indicates that **1** is isostructural to the reported data [14]. Thus, it can be deduced that nanomaterial **1** has the chemical formula of $\text{Tb}_3(2\text{-MeBAH})_9(\text{DMF})_3$. It has one-dimensional polymer structure (Figure 3), and the one-dimensional structure is connected by the trinuclear second building unit (SBU, Figure 4); the 1D structure is connected by hydrogen bond and van der Waals (VDW) forth to form 3D structure.

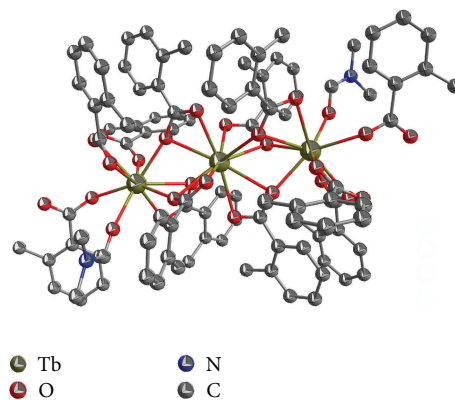


FIGURE 4: The SBU structure of material **1**.

The elemental analysis of **1** reveals that C is 51.17% and H is 4.151%, which is consistent with the calculated results

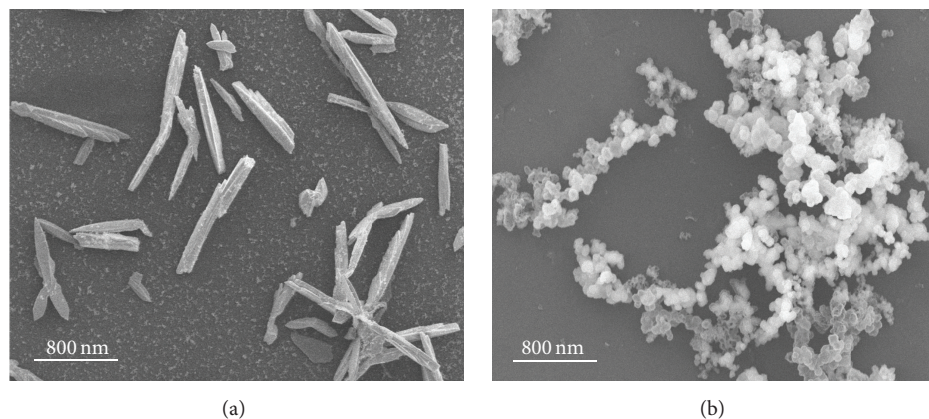


FIGURE 5: The SEM of different weight ratio of Tb^{3+} to ligand: (a) $Tb^{3+}/\text{ligand} = 1:3$; (b) $Tb^{3+}/\text{ligand} = 3:1$.

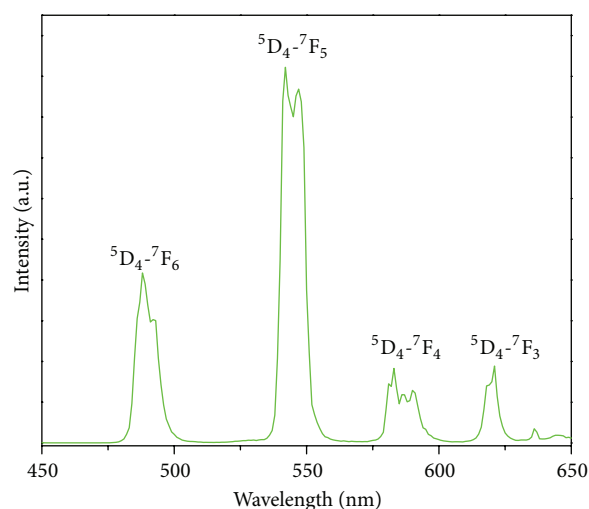


FIGURE 6: Downconversion luminescence spectrum of **1**.

well (C, 50.94; H, 4.220). This further confirms that bulk nanomaterial really has structure as depicted in Figures 3 and 4 and has the molecular formula of $Tb_3(2\text{-MeBAH})_9(\text{DMF})_3$.

In order to reveal the factors influencing the formation and morphology of the hollow spheres of **1**, controlled experiments were carefully performed [15]. As shown by the SEM images in Figure 5, when the weight ratio of Tb^{3+} to ligand is 1:3, it is found that almost all the products are microrods, and when the weight ratio is 3:1, the product is ruleless ball-like structure.

Due to the unique properties of rare earth elements, the downward luminescent property of sample **1** was determined at the excitation wavelength of 320 nm under ambient temperature. Sample **1** exhibits characteristic transitions of the Tb^{3+} ion at 489, 544, 583, and 621 nm, corresponding to the transitions of $^5D_4 \rightarrow ^7F_6$, $^5D_4 \rightarrow ^7F_5$, $^5D_4 \rightarrow ^7F_4$, and $^5D_4 \rightarrow ^7F_3$, respectively (Figure 6) [16–19]. The strongest peak is ascribed to the transition of $^5D_4 \rightarrow ^7F_5$ [4, 20–22]. The ligand is at the excited $^1\pi\pi^*$ state after the simultaneous absorption of one photon and then transfers to the excited $^3\pi\pi^*$ state through intersystem crossing (ISC), after that, the

energy transfer (ET) to 5D_4 state of Tb^{3+} , and luminescence is generated by the $^5D_4 \rightarrow ^7F_j$ ($j = 6, 5, 4$ and 3) transitions.

4. Conclusions

Lanthanide CPs nanosheet aggregates have been synthesized via a facile template-free solvothermal strategy using DMF as a solvent and 2-MeBAH as ligand. The products were characterized by PXRD, SEM, EA, and downward luminescence. The downward luminescence of product **1** built from Tb^{3+} and 2-MeBAH has one-dimensional structure connected by trinuclear SBU. Downward luminescence shows that sample **1** exhibits characteristic transitions of $^5D_4 \rightarrow ^7F_j$ ($j = 6, 5, 4$ and 3) for Tb^{3+} at 489, 544, 583, and 621 nm, respectively, and the strongest peak is at 544 nm ascribed to the transition of $^5D_4 \rightarrow ^7F_5$.

Competing Interests

The authors declare that they have no competing interests.

Acknowledgments

The authors acknowledge the financial support of the Open Project Program of Key Laboratory of Functional Small Organic Molecule, Ministry of Education (no. KLFS-KF-201422) and Jiangxi Normal University (no. 5616).

References

- [1] D. Yang, Y. Wang, Y. Wang, Z. Li, and H. Li, "Luminescence enhancement after adding organic salts to nanohybrid under aqueous condition," *ACS Applied Materials and Interfaces*, vol. 7, no. 3, pp. 2097–2103, 2015.
- [2] N. Ekthammathat, T. Thongtem, A. Phuruangrat, and S. Thongtem, "Synthesis and characterization of CeVO₄ by microwave radiation method and its photocatalytic activity," *Journal of Nanomaterials*, vol. 2013, Article ID 434197, 7 pages, 2013.
- [3] D. Falcomer, A. Speghini, G. Ibba et al., "Morphology and luminescence of nanocrystalline Nb₂O₅ doped with Eu³⁺," *Journal of Nanomaterials*, vol. 2007, Article ID 94975, 5 pages, 2007.
- [4] C.-H. Zeng, J.-L. Wang, Y.-Y. Yang et al., "Lanthanide CPs: the guest-tunable drastic changes of luminescent quantum yields, and two photon luminescence," *Journal of Materials Chemistry C*, vol. 2, no. 12, pp. 2235–2242, 2014.
- [5] H. Liu, T. Chu, Z. Rao, S. Wang, Y. Yang, and W.-T. Wong, "The tunable white-light and multicolor emission in an electrodeposited thin film of mixed lanthanide coordination polymers," *Advanced Optical Materials*, vol. 3, no. 11, pp. 1545–1550, 2015.
- [6] M. Xie, Y. Zhu, Y. Yang, and F. Zhao, "Ultrafast dynamics of two-photon absorption related filaments in methanol solution of a Tb(III) complex," *Optical Materials*, vol. 36, no. 4, pp. 727–731, 2014.
- [7] C. B. Han, Y. L. Wang, Y. L. Li, C. M. Liu, and Q. Y. Liu, "Slow magnetization relaxation in a one-dimensional chiral dysprosium-carboxylate compound constructed from the cubic Dy₄(μ₃-OH)₄ clusters," *Inorganic Chemistry Communications*, vol. 58, pp. 91–94, 2015.
- [8] S.-L. Zhong, R. Xu, L.-F. Zhang et al., "Terbium-based infinite coordination polymer hollow microspheres: preparation and white-light emission," *Journal of Materials Chemistry*, vol. 21, no. 41, pp. 16574–16580, 2011.
- [9] X. Kang, D. Yang, P. Ma et al., "Fabrication of hollow and porous structured GdVO₄:Dy³⁺ nanospheres as anticancer drug carrier and MRI contrast agent," *Langmuir*, vol. 29, no. 4, pp. 1286–1294, 2013.
- [10] R. C. Lv, S. L. Gai, Y. L. Dai, F. He, N. Niu, and P. P. Yang, "Surfactant-free synthesis, luminescent properties, and drug-release properties of LaF₃ and LaCO₃F hollow microspheres," *Inorganic Chemistry*, vol. 53, no. 2, pp. 998–1008, 2014.
- [11] E. Martinez-Castro, J. Garcia-Sevillano, F. Cusso, and M. Ocana, "Template-free synthesis and luminescent properties of hollow Ln:YOF (Ln = Eu or Er plus Yb) microspheres," *Journal of Alloys and Compounds*, vol. 619, pp. 44–51, 2015.
- [12] Z. Wang, H. Liu, S. Wang, Z. Rao, and Y. Yang, "A luminescent Terbium-Succinate MOF thin film fabricated by electrodeposition for sensing of Cu²⁺ in aqueous environment," *Sensors and Actuators B: Chemical*, vol. 220, pp. 779–787, 2015.
- [13] T. Chu, H. Liu, Y. Yang et al., "A new dinuclear terbium complex as a novel luminescence probe for detecting amines," *Journal of Photochemistry and Photobiology A: Chemistry*, vol. 294, pp. 38–43, 2014.
- [14] H. Busskamp, G. B. Deacon, M. Hilder et al., "Structural variations in rare earth benzoate complexes: part I. Lanthanum," *CrystEngComm*, vol. 9, no. 5, pp. 394–411, 2007.
- [15] J. Huo, L. Wang, E. Irran et al., "Hollow ferrocenyl coordination polymer microspheres with micropores in shells prepared by Ostwald ripening," *Angewandte Chemie—International Edition*, vol. 49, no. 48, pp. 9237–9241, 2010.
- [16] K. Zheng, K.-L. Lou, C.-H. Zeng, S.-S. Li, Z.-W. Nie, and S. Zhong, "Hybrid membrane of agarose and lanthanide coordination polymer: a selective and sensitive Fe³⁺ sensor," *Photochemistry and Photobiology*, vol. 91, no. 4, pp. 814–818, 2015.
- [17] C.-H. Zeng, X.-T. Meng, S.-S. Xu, L.-J. Han, S. Zhong, and M.-Y. Jia, "A polymorphic lanthanide complex as selective Co²⁺ sensor and luminescent timer," *Sensors and Actuators B: Chemical*, vol. 221, pp. 127–135, 2015.
- [18] Z.-Q. Yan, X.-T. Meng, R.-R. Su et al., "Basophilic method for lanthanide MOFs with a drug ligand: crystal structure and luminescence," *Inorganica Chimica Acta*, vol. 432, pp. 41–45, 2015.
- [19] S.-S. Li, Z.-N. Ye, S.-S. Xu et al., "Highly luminescent lanthanide CPs based on dinuclear cluster: crystal structure and sensitive Trp sensor," *RSC Advances*, vol. 5, no. 88, pp. 71961–71967, 2015.
- [20] T. T. Shen, Y. Zhang, W. S. Liu, and Y. Tang, "Novel multi-color photoluminescence emission phosphors developed by layered gadolinium hydroxide via in situ intercalation with positively charged rare-earth complexes," *Journal of Materials Chemistry C*, vol. 3, no. 8, pp. 1807–1816, 2015.
- [21] C.-H. Zeng, F.-L. Zhao, Y.-Y. Yang et al., "Unusual method for phenolic hydroxyl bridged lanthanide CPs: syntheses, characterization, one and two photon luminescence," *Dalton Transactions*, vol. 42, no. 6, pp. 2052–2061, 2013.
- [22] C.-H. Zeng, Y.-Y. Yang, Y.-M. Zhu, H.-M. Wang, T.-S. Chu, and S. W. Ng, "A new luminescent terbium 4-methylsalicylate complex as a novel sensor for detecting the purity of methanol," *Photochemistry and Photobiology*, vol. 88, no. 4, pp. 860–866, 2012.